

THE GEOMETRY AND BIOMECHANICS OF NORMAL
AND PATHOMORPHOLOGIC HUMAN HIPS

by

Michael Dennison Harris

A dissertation submitted to the faculty of
The University of Utah
in partial fulfillment of the requirements for the degree of

Doctor of Philosophy

Department of Bioengineering

The University of Utah

August 2013

Copyright © Michael Dennison Harris 2013

All Rights Reserved

The University of Utah Graduate School

STATEMENT OF DISSERTATION APPROVAL

The dissertation of Michael Dennison Harris

has been approved by the following supervisory committee members:

<u>Andrew E. Anderson</u>	, Chair	<u>3/29/2013</u> Date Approved
---------------------------	---------	-----------------------------------

<u>Robert W. Hitchcock</u>	, Member	<u>3/29/2013</u> Date Approved
----------------------------	----------	-----------------------------------

<u>Bruce A. MacWilliams</u>	, Member	<u>3/29/2013</u> Date Approved
-----------------------------	----------	-----------------------------------

<u>Christopher L. Peters</u>	, Member	<u>3/27/2013</u> Date Approved
------------------------------	----------	-----------------------------------

<u>Richard D. Rabbitt</u>	, Member	<u>3/27/2013</u> Date Approved
---------------------------	----------	-----------------------------------

<u>Jeffrey A. Weiss</u>	, Member	<u>3/27/2013</u> Date Approved
-------------------------	----------	-----------------------------------

and by Patrick Tresco, Chair of
the Department of Bioengineering

and by Donna M. White, Interim Dean of The Graduate School.

ABSTRACT

Geometric abnormalities of the human hip joint, as found in femoroacetabular impingement (FAI) and acetabular dysplasia, alter hip biomechanics and may be the primary causes of osteoarthritis in young adults. However, empirical evidence of direct correlations between abnormal geometry, altered biomechanics, and osteoarthritis is scarce. Also, clinical measures used to diagnose FAI and dysplasia still have substantial limitations, including questions about their reliability, assumptions about hip joint geometry and their ability to definitively distinguish pathologic from normal hips. The goals of this dissertation are twofold. First, a set of tools are presented and applied to quantify three-dimensional (3D) anatomical differences between hips with FAI and control subjects. The 3D tools were developed, validated and applied to patients with a subtype of FAI, called cam FAI, to improve basic understanding of the spectrum of FAI deformities, and to provide meaningful new metrics of morphology that are relatable to current diagnostic methods and translate easily for clinical use. The second goal of this dissertation is to improve our understanding of intra-articular hip contact mechanics as well as hip joint kinematics and muscle forces. To do so, a finite element study of intra-articular cartilage contact mechanics was completed with a cohort of live human subjects, using a validated modeling protocol. Finally, musculoskeletal modeling was used with gait data from healthy subjects and acetabular dysplasia patients to provide preliminary estimates of hip joint kinematics, kinetics, and muscle forces and compare differences

between the groups. The translational methods of this dissertation utilized techniques from orthopaedics, computer science, physical therapy, mechanics, and medical imaging. Results from this dissertation offer new insight into the complex pathomechanics and pathomorphology of FAI and acetabular dysplasia. Application and extension of the work of this dissertation has the potential to help establish links between FAI and dysplasia with osteoarthritis and to improve patient care.

To my wife, Hannah.
You are exceptional in every way.

TABLE OF CONTENTS

ABSTRACT.....	iii
LIST OF TABLES.....	x
LIST OF FIGURES.....	xi
ACKNOWLEDGEMENTS.....	xiv
Chapters	
1. INTRODUCTION.....	1
1.1 Motivation.....	1
1.2 Research Goals.....	4
1.3 Summary of Chapters.....	5
1.4 References.....	8
2. BACKGROUND.....	13
2.1 The Human Hip Joint: Anatomy and Function.....	13
2.1.1 Pelvis and Femur Bones.....	13
2.1.2 Articular Cartilage.....	15
2.1.3 Acetabular Labrum and Hip Joint Capsule.....	17
2.1.4 Surrounding Musculature.....	17
2.2 Pathologies of the Hip.....	18
2.2.1 Osteoarthritis.....	19
2.2.2 Acetabular Dysplasia.....	20
2.2.3 Femoroacetabular Impingement.....	22
2.3 Measurement of Hip Morphology.....	25
2.3.1 Radiographic Measures.....	25
2.3.3 Three-dimensional Characterization of Hip Morphology.....	26
2.4 Measurement of Hip Mechanics.....	28
2.4.1 Intra-articular Cartilage Contact Mechanics.....	29
2.4.2 Whole-joint Mechanics (Kinematics and Kinetics).....	31
2.4.3 Muscle Force Modeling.....	32
2.5 References.....	34

3. THREE-DIMENSIONAL QUANTIFICATION OF FEMORAL HEAD SHAPE IN CONTROLS AND PATIENTS WITH CAM-TYPE FEMOROACETABULAR IMPINGEMENT.....	51
3.1 Abstract.....	51
3.2 Introduction.....	52
3.3 Patients and Methods.....	54
3.3.1 Subject Selection.....	54
3.3.2 3D Reconstruction.....	55
3.3.3 Comparison to Ideal Geometries.....	56
3.3.4 Regionalization of the Femoral Head and Characterization of the Protrusion.....	57
3.3.5 Statistical Analysis.....	58
3.4 Results.....	58
3.5 Discussion.....	60
3.6 Acknowledgements.....	65
3.7 References.....	65
4. CORRELATIONS BETWEEN THE ALPHA ANGLE AND FEMORAL HEAD ASPHERICITY: IMPLICATIONS AND RECOMMENDATIONS FOR DIAGNOSING CAM FEMOROACETABULAR IMPINGEMENT.....	77
4.1 Abstract.....	77
4.2 Introduction.....	78
4.3 Patients and Methods.....	79
4.3.1 Subject Selection.....	79
4.3.2 3D Reconstruction and Sphere Fitting.....	80
4.3.3 Generation and Alignment of Digitally Reconstructed Radiographs.....	81
4.3.4 Generation and Alignment of Radial CT and Oblique Axial Views.....	82
4.3.5 Measurement of the Alpha Angle.....	83
4.3.6 Statistical Analysis.....	83
4.4 Results.....	84
4.5 Discussion.....	85
4.6 Appendix.....	89
4.6.1 DRR Validation: Methods.....	89
4.6.2 DRR Validation: Results.....	90
4.7 Acknowledgements.....	91
4.8 References.....	91
5. STATISTICAL SHAPE MODELING OF CAM FEMOROACETBAULAR IMPINGEMENT.....	104
5.1 Abstract.....	104

5.2 Introduction.....	105
5.3 Methods.....	107
5.3.1 Subject Selection.....	107
5.3.2 Three-dimensional Reconstruction and SSM Preprocessing.....	108
5.3.3 Statistical Shape Modeling.....	109
5.3.4 Analysis.....	111
5.4 Results.....	112
5.5 Discussion.....	114
5.6 Acknowledgements.....	118
5.7 References.....	118
 6. FINITE ELEMENT PREDICTION OF CARTILAGE CONTACT STRESSES IN NORMAL HUMAN HIPS.....	 127
6.1 Abstract.....	127
6.2 Introduction.....	128
6.3 Methods.....	129
6.3.1 Subject Selection and CT Imaging.....	129
6.3.2 Surface Reconstruction, Mesh Generation and Constitutive Models.....	131
6.3.3 Model Positioning, Boundary Conditions and Loading.....	132
6.3.4 Contact Areas and Stresses.....	133
6.3.5 Statistical Analysis.....	133
6.4 Results.....	133
6.4.1 Contact Stress Distributions and Contact Area.....	133
6.4.2 Peak and Average Contact Stresses.....	134
6.4.3 Regional Differences in Average Contact Stresses.....	135
6.5 Discussion.....	136
6.6 Acknowledgments.....	140
6.7 References.....	141
 7. JOINT ANGLES, MOMENTS, MUSCLE FORCES, AND REACTION FORCES IN NORMAL AND DYSPLASTIC HIPS.....	 150
7.1 Abstract.....	150
7.2 Introduction.....	151
7.3 Methods.....	153
7.3.1 Data Collection and Processing (Feasibility Study).....	153
7.3.2 Musculoskeletal Modeling (Feasibility Study).....	155
7.3.3 Modeling Control Subjects and Dysplastic Patients.....	156
7.3.4 Analysis.....	157
7.4 Results.....	158
7.4.1 Feasibility and Validation.....	158
7.4.2 Demographics, Joint Angles, and Moments.....	159
7.4.3 Joint Reaction and Muscle Forces.....	160

7.5 Discussion.....	161
7.6 Acknowledgements.....	169
7.7 References.....	169
8. CONCLUSION.....	184
8.1 Summary and Impact.....	184
8.1.1 Objective 1.....	184
8.1.2 Objective 2.....	187
8.2 Limitations and Future Work.....	188
8.3 References.....	192

LIST OF TABLES

3.1	Mean \pm standard error maximum deviation values, 95% confidence intervals of maximum deviations, and mean \pm standard error fitting errors of control and patient femurs from best-fit spheres and conchoids.....	74
4.1	Alpha angles and ICCs with 95% confidence intervals for each view.....	100
7.1	Average \pm standard deviation forces generated by muscles spanning the hip during peaks JRF times.....	182

LIST OF FIGURES

2.1	Bony anatomy of the hip.....	47
2.2	Bony reconstructions of dysplastic and healthy hips.....	48
2.3	Femoral morphology in a cam FAI patient compared to a healthy control.....	49
2.4	Two common radiographic measures of acetabular dysplasia and FAI.....	50
3.1	Alpha angle and head-neck offset measured on DRRs of the standing frog-leg lateral view.....	70
3.2	Three-dimensional reconstructions of the femur showing the process of identifying the head neck junction and regionalization of the femoral head....	71
3.3	Geometric description of rotational conchoid according to equation $r=a+b*cos(\theta)$	72
3.4	Deviations from ideal sphere and rotational conchoid shapes in representative control and patient femurs.....	73
3.5	Maximum protrusion and mean deviation by region.....	75
3.6	Protrusion areas determined in the region of maximum deviation from spheres (top) and conchoids (bottom).....	76
4.1	Process of femoral head isolation and sphere fitting.....	95
4.2	DRR generation.....	96
4.3	DRR alignment routine applied to standing frog-leg lateral.....	97
4.4	Planes and resulting radial CT views for 1 subject.....	98
4.5	Representative DRRs and 90° Radial CT / oblique axial view with alpha angle (α) outlines for a single cam FAI patient.....	99

4.6	Linear regressions (solid line), including 95% confidence intervals (dashed lines), of alpha angles (α) compared to maximum deviations from spheres.....	101
4.7	DRR validation.....	102
4.8	Bland-Altman plot of agreement between traditional radiograph and DRR measurements (top: interbead distances, bottom: alpha angles).....	103
5.1	Correspondence particle distribution on a control (top) and cam FAI (bottom) femur.....	122
5.2	Mean control (left) and cam (right) shapes.....	123
5.3	Cumulative shape variation captured in the 70 PCA modes when PCA was run for all femurs.....	124
5.4	Shape variation captured in the first 3 modes.....	125
5.5	Color plot of a single cam FAI femur (shown) and the amount it deviates from the average control femur.....	126
6.1	FE model creation and simulated loading scenarios.....	145
6.2	Contact stresses on the acetabular cartilage for each subject during walking, ascending stairs and descending stairs.....	146
6.3	CT image and model predictions of cartilage contact stress for 1 subject, illustrating the effects of bony geometry.....	147
6.4	Contact area on the articulating surface of the acetabular cartilage as a function of activity.....	148
6.5	Average contact stress as a function of region and activity.....	149
7.1	Frontal and sagittal view of unscaled OpenSim musculoskeletal model.....	175
7.2	Residual forces and moments, after RRA, averaged across 7 trials for 1 subject.....	176
7.3	Rectified and normalized EMG signals (green) compared to OpenSim predictions of muscle activations (black).....	177
7.4	Average pelvis angles for control and dysplastic subjects.....	178

7.5	Average hip angles and moments for controls and dysplastic patients.....	179
7.6	Knee flexion angles and moments for control and dysplastic subjects.....	180
7.7	Average joint reaction forces at the hip for control and dysplastic subjects....	181
7.8	Muscle forces from a representative control subject (top) and a dysplastic patient (bottom).....	183

ACKNOWLEDGEMENTS

My thanks to Andy Anderson, PhD for always doing his best as an advisor and mentor. No one can question that he wants his students to succeed, and he has done everything in his power to make that happen. As one of his first students, this has been a challenging, painful, rewarding, and enjoyable experience for both of us. I would also like to thank Jeff Weiss, PhD for employing me as an undergraduate and always being available to offer advice. His guidance has been invaluable. Thanks also to the members of my supervisory committee (Bruce MacWilliams, PhD; Chris Peters, MD; Rick Rabbitt, PhD; and Bob Hitchcock, PhD). I have received ample support and quick responses from each member of my committee and I appreciate the sacrifice they have made of their time. I have learned from each of them. One of the most rewarding things about the research in this dissertation is that I have been able to interact with many skilled individuals from an array of disciplines. Thus, I would like to also thank Bo Foreman, PhD, Ross Whitaker, PhD, Heath Henninger, PhD, Kent Bachus, PhD, Jill Erickson PA-C, Steve Aoki, MD, Hugh West MD, Manasi Datar, BS, Corinne Henak, BS, Ashley Kapron, BS, Christine Abraham, BA and the staff and students of the Orthopaedic Research Lab, the Musculoskeletal Research Lab, Shriners Intermountain Movement Analysis Lab, and the MOCAP Lab.

Although my name is on this dissertation, none of the studies described could have been completed without the contributions of my coauthors. Thank you.

I also need to recognize the financial support I have received through donor-funded scholarships and fellowships. Thanks to the donors, orchestrators and distributors of the Obyn Memorial Scholarship in Orthopaedics, the LS Peery Discovery Program in Musculoskeletal Restoration, the David R. and Isabelle E. Atherton Scholarship in the School of Medicine, and the Campbell Endowed Graduate Fellowship. Among those individuals, a special thanks to LeAnn Chandler and Art Swindle.

An understated but earnest thanks to my parents for teaching the need for an education and a productive life; thank you for always being concerned for my success and welfare. Finally, thanks to my wife, to whom this work is dedicated, and my children. A happy home has made all the difference during this experience.

CHAPTER 1

INTRODUCTION

1.1 Motivation

A healthy hip allows efficient movement during activities of daily living and can endure for a lifetime. However, mechanical disruption at any stage of life can impede normal hip function and cause premature degeneration of the intra-articular tissues required for pain free motion and proper load distribution. Specifically, alteration of the hip's mechanical environment due to traumatic injury, increase in body mass, genetic disposition (e.g., weakness of bone or cartilage), or geometric abnormalities (i.e., a morphologically abnormal hip), or a combination of these factors, can initiate and propagate the disease, osteoarthritis (OA).^{1,2}

OA is the most common degenerative disease of the hip, and the most prevalent of all forms of arthritis. Besides pain and disability, OA presents a large financial burden to patients and healthcare organizations, accounting for 85% of all arthritis related costs in the US at a cost of more than \$64 billion per year.^{3,4}

While commonly thought of as a disease of the elderly, OA can develop in younger adults. It is generally believed that abnormal bony geometry alters the hip's mechanical environment and predisposes younger individuals to early OA. Acetabular dysplasia (also known as developmental dysplasia of the hip or dysplasia) and

femoroacetabular impingement (FAI) are two diseases primarily characterized by altered hip geometry and may be the primary causes of early hip OA.⁵⁻¹⁰ Subtle cases of these diseases that remain undiagnosed may also be major contributors to hip degeneration later in life.⁶ Although usually distinct, acetabular dysplasia and FAI are each characterized by a misshapen femoral head or acetabulum, which may detrimentally alter loading within the hip. Abnormal loads are thought to cause tears and excessive wear of the acetabular labrum and articular cartilage.^{5,11-13}

Total joint replacement is the mainstay treatment for OA, but is undesirable in younger adults and adolescents because of consequential restrictions to activity and the need for implant revision earlier in life. Accordingly, hip joint preserving surgeries have been proposed for young adults with FAI and dysplasia to delay initiation or curb propagation of OA and prolong the lifetime of the natural hip.^{11,14-16} The goal of such surgeries is to reshape, reorient, and/or repair joint anatomy to relieve pain, improve range of motion, and curtail soft tissue damage.

It is thought that early diagnosis and intervention in cases of dysplasia and FAI offers the best chance for preservation surgery success. However, many patients do not receive immediate treatment.¹⁷ Delayed treatment may be due to initial misdiagnosis or concomitant complications that mask symptoms.^{15,17} In response to the need for better and earlier treatment, there has been a dramatic increase in clinical and basic-science research attention in recent years on the topics of FAI and dysplasia. For example, a search of “femoroacetabular impingement” on the Pubmed.gov data base resulted in a single manuscript from the years 1950 to 2000, compared to over 630 from 2000 to 2012. Unfortunately, clinical measures used to diagnose FAI and dysplasia still have substantial

limitations, including questions about their reliability, assumptions about hip joint geometry and their ability to definitively distinguish pathologic from normal hips.¹⁸⁻²³

Most diagnostic measures are based on radiographic, CT or MR images.²⁴⁻²⁶ Thus, measures of hip morphology are primarily two-dimensional (2D). However, 2D measurements cannot fully characterize the three-dimensional (3D) nature or the spectrum of complex bony deformities with which FAI and dysplasia patients present. Although recent research has produced a number of 3D techniques to visualize pathologic hip morphology, much of what has been presented is qualitative, complicated, and does not produce data that translate well for clinical interpretation.²⁷⁻³⁰

Also, many questions remain regarding the mechanics of dysplastic and FAI hips. For example, few empirical data of intra-articular mechanics in FAI or dysplastic hip exist to support the suspected links between altered morphology, altered mechanics, and development of hip OA. As a result, deductions about abnormal shape, mechanics and damage come largely from intra-operative observations, theoretical models of bony impingement, and simplified mechanical models that either treat the hip as a perfect ball and socket or as a 2D analytical problem.^{5,27,31,32} Further, an increasing number of follow-up and prevalence studies are demonstrating that radiographic evidence of FAI or dysplasia does not reliably predict symptoms and development of OA.^{20,33-37}

Thus, quantitative descriptions of hip joint morphology must be developed to better distinguish healthy from pathologic hips, and our understanding of hip joint mechanics in both healthy and pathologic subjects must be improved.

1.2 Research Goals

The goals of this dissertation were twofold. First, a set of tools are presented and applied to quantify anatomical differences between hips with FAI and control subjects. The second goal of this dissertation is to improve our understanding of intra-articular contact mechanics as well as joint kinematics and muscle forces in healthy and dysplastic hips.

The osseous anatomy is a major focus when diagnosing and treating FAI, and is commonly measured using 2D radiographs. In Chapters 3 through 5, 3D tools are developed, validated, and applied to patients with a subtype of FAI, called cam FAI. The objective of Chapters 3 through 5 was to improve basic understanding of the spectrum of cam FAI deformities, and to provide meaningful new metrics of morphology that are relatable to current diagnostic methods and that translate easily for clinical use.

Clinical evidence suggests that the altered anatomy of FAI and dysplasia leads to altered mechanics, and initiation of OA. However, there is still much to be learned about intra-articular mechanics even within healthy joints. In this dissertation, two studies were completed to further our understanding of hip joint mechanics in healthy and pathologic conditions. The study described in Chapter 6 provides estimations of cartilage contact stresses in healthy joints using a validated finite element (FE) modeling protocol. Chapter 7 demonstrates the feasibility of using musculoskeletal models to estimate hip joint kinematics and muscle forces in healthy subjects and patients with acetabular dysplasia.

1.3 Summary of Chapters

There are 8 chapters in this dissertation. Chapter 2 provides background information to contextualize the research. Chapter 2 cannot feasibly discuss all studies related to hip morphology and mechanics, but it does seek to provide readers with sufficient information to appreciate the importance of the hip joint, the body of work committed to the study of the hip, and the need for the work completed in this dissertation. Specifically, hip anatomy, development, and function are described. Relevant prior work and the current state of the art with respect to the characterization of hip joint morphology and mechanics are discussed and metrics used to diagnose FAI, especially cam FAI, and acetabular dysplasia are outlined.

Chapters 3 through 7 represent work completed between 2008 and 2013 to meet the research goals stated above. Chapters 3 through 6 are reproductions of manuscripts that have been accepted or are under review in orthopaedic and biomedical engineering journals. Chapter 3 was reprinted with kind permission from Springer Science+Business Media B.V. Chapter 6 was reprinted with permission from John Wiley and Sons Publishing. Permission was not necessary to reprint the remaining manuscripts. Chapter 7 describes a study that is in preparation for submission. Chapter 8 discusses the general impact of this dissertation and describes planned and potential future extensions of the tools and results from Chapters 3 through 7.

The following paragraphs provide a short description of the motivation for, and objectives of, Chapters 3 through 7.

The hip joint is often idealized as a perfect ball and socket. However, both the acetabulum and the femoral head have been shown to have some level of asphericity (i.e.,

deviation from a perfect sphere).³⁸⁻⁴⁰ In Chapter 3, subject-specific 3D femur models are used to quantify the amount of deviation from idealized geometries (e.g., spheres and rotational conchoids) that may be expected in control femurs and patients with cam FAI. The study offers a novel, objective measurement technique that describes femoral head morphology better than 2D radiographs or single CT and MR image slices. The study also provides information about where and how large deviations from ideal shapes are on a subject-specific basis. Chapter 3 is in press with the *Annals of Biomedical Engineering*.

While techniques which capture 3D morphology provide a more complete characterization of hip morphology, 2D clinical measures taken from x-rays or radial CT/MR images are likely to remain a primary clinical detection tool for cam FAI. In Chapter 4 the objective 3D measures of femoral asphericity presented in Chapter 3, are extended to the clinic. Specifically, 3D measures of asphericity are correlated with the most popular radiographic measure of cam FAI – the alpha angle.⁴¹ Despite the alpha angle's popularity, there is considerable debate about the correct radiographic or radial CT/MR view of the femur from which it should be measured.^{21,42-44} Results from Chapter 4 demonstrate the strength of each alpha angle measurement for describing true femoral head asphericity. Chapter 4 is in review with the journal, *Radiology*.

Chapters 3 and 4 provide information about the magnitude and location of osseous deformities when compared to idealized geometry. However, these measurements cannot directly characterize the degree to which cam FAI patients differ in anatomical shape from normal femurs. In Chapter 5, statistical shape modeling (SSM) is applied to normal and cam FAI femurs to facilitate direct quantitative and qualitative comparisons of femur anatomy between patients with cam FAI and controls. A major advantage of SSM over

other 3D techniques is that SSM makes no assumptions about femoral shape. Accordingly, Chapter 5 provides the first objectively determined average femur shapes from control and cam FAI groups, as well as information about shape variation within the groups, which can serve to better characterize the spectrum of bony deformities with which FAI patients present. With future development, SSM may be used to generate pre- or intraoperative rubrics to guide resection of cam deformities. SSM applied to FAI also has the potential to elucidate additional morphologic features of cam FAI that cannot be easily determined by human visual inspection or measurements of 3D asphericity alone. The study reported in Chapter 5 has been accepted pending minor revisions in the *Journal of Orthopaedic Research*.

As mentioned, little quantitative data exist to characterize in vivo cartilage mechanics in normal or pathomorphologic hips. The lack of reliable data with respect to cartilage mechanics may come from the difficulty in developing models that include subject-specific joint morphology or represent tissue behavior that agrees with in vitro experimental data. Prior to the start of this dissertation, extensive work was completed by Anderson et al. to develop and validate a model that accurately incorporated the osseous and cartilaginous geometry, and as a result, provided excellent predictions of cartilage contact stresses.⁴⁵⁻⁴⁹ In Chapter 6 the methods of Anderson et al. were refined and applied, for the first time, to a cohort of live human subjects who have anatomically normal appearing hips. Chapters 3 through 5 illustrated the importance of morphologic differences between healthy and pathologic hips. Chapter 6 demonstrates how morphologic differences, even among healthy subjects, result in highly individualized cartilage contact stress patterns. Results from the study, besides illustrating important

characteristics of the normal hip joint, have served as a foundation for subsequent investigations of contact stresses in hips with acetabular dysplasia. Chapter 6 was featured as the cover article in the July 2012 issue of the *Journal of Orthopaedic Research*.

Much of the focus when diagnosing and treating FAI and dysplasia has been upon the geometry of the articulating surfaces (i.e., the bone and cartilage of the femoral head and acetabulum). However, FAI and dysplasia are complex pathomechanical diseases that likely involve mechanical alterations to not only the articulating area of the hip joint but also the ligaments of the hip capsule and the musculature surrounding the hip. It is possible that patients with FAI and dysplasia alter muscle-driven motions of the hip to reduce pain or compensate for feelings of instability. The final study of this dissertation involves modeling of the musculature of the lower limbs in healthy subjects and dysplasia patients. The objectives of this study were to assess the feasibility of using an available musculoskeletal model to estimate muscle and joint forces at the hip and to compare hip joint kinematics and muscle forces between healthy control subjects and those with acetabular dysplasia. The study demonstrates the feasibility of using musculoskeletal models to compare whole joint mechanics between healthy controls and patients with pathologic hips, and provides preliminary data about possible muscular differences between such groups.

1.4 References

1. Ganz R, Leunig M, Leunig-Ganz K, Harris WH. 2008. The etiology of osteoarthritis of the hip: An integrated mechanical concept. *Clin Orthop Relat Res* 466:264-272.

2. Hoaglund FT, Steinbach LS. 2001. Primary osteoarthritis of the hip: Etiology and epidemiology. *J Am Acad Orthop Surg* 9:320-327.
3. Buckwalter JA, Saltzman C, Brown T. 2004. The impact of osteoarthritis: Implications for research. *Clin Orthop Relat Res*:S6-15.
4. Murphy L, Helmick CG. 2012. The impact of osteoarthritis in the united states: A population-health perspective. *Am J Nurs* 112:S13-19.
5. Beck M, Kalhor M, Leunig M, Ganz R. 2005. Hip morphology influences the pattern of damage to the acetabular cartilage: Femoroacetabular impingement as a cause of early osteoarthritis of the hip. *J Bone Joint Surg Br* 87:1012-1018.
6. Harris WH. 1986. Etiology of osteoarthritis of the hip. *Clin Orthop Relat Res*:20-33.
7. Jessel RH, Zurakowski D, Zilkens C, et al. 2009. Radiographic and patient factors associated with pre-radiographic osteoarthritis in hip dysplasia. *J Bone Joint Surg Am* 91:1120-1129.
8. Ganz R, Parvizi J, Beck M, et al. 2003. Femoroacetabular impingement: A cause for osteoarthritis of the hip. *Clin Orthop Relat Res*:112-120.
9. Harris-Hayes M, Royer NK. 2011. Relationship of acetabular dysplasia and femoroacetabular impingement to hip osteoarthritis: A focused review. *PM R* 3:1055-1067 e1051.
10. Jacobsen S, Sonne-Holm S. 2005. Hip dysplasia: A significant risk factor for the development of hip osteoarthritis. A cross-sectional survey. *Rheumatology (Oxford)* 44:211-218.
11. Sanchez-Sotelo J, Trousdale RT, Berry DJ, Cabanela ME. 2002. Surgical treatment of developmental dysplasia of the hip in adults: I. Nonarthroplasty options. *J Am Acad Orthop Surg* 10:321-333.
12. Nishii T, Sugano N, Tanaka H, et al. 2001. Articular cartilage abnormalities in dysplastic hips without joint space narrowing. *Clin Orthop Relat Res*:183-190.
13. Neumann G, Mendicuti AD, Zou KH, et al. 2007. Prevalence of labral tears and cartilage loss in patients with mechanical symptoms of the hip: Evaluation using mr arthrography. *Osteoarthritis Cartilage* 15:909-917.
14. Clohisy JC, Barrett SE, Gordon JE, et al. 2006. Periacetabular osteotomy in the treatment of severe acetabular dysplasia. Surgical technique. *J Bone Joint Surg Am* 88 Suppl 1 Pt 1:65-83.

15. Peters CL, Erickson JA, Anderson L, et al. 2009. Hip-preserving surgery: Understanding complex pathomorphology. *J Bone Joint Surg Am* 91 Suppl 6:42-58.
16. Clohisy JC, St John LC, Nunley RM, et al. 2009. Combined periacetabular and femoral osteotomies for severe hip deformities. *Clin Orthop Relat Res* 467:2221-2227.
17. Clohisy JC, Knaus ER, Hunt DM, et al. 2009. Clinical presentation of patients with symptomatic anterior hip impingement. *Clin Orthop Relat Res* 467:638-644.
18. Hansen BJ, Harris MD, Anderson LA, et al. 2012. Correlation between radiographic measures of acetabular morphology with 3d femoral head coverage in patients with acetabular retroversion. *Acta Orthop* 83:233-239.
19. Sutter R, Dietrich TJ, Zingg PO, Pfirrmann CW. 2012. How useful is the alpha angle for discriminating between symptomatic patients with cam-type femoroacetabular impingement and asymptomatic volunteers? *Radiology* 264:514-521.
20. Audenaert EA, Peeters I, Van Onsem S, Pattyn C. 2011. Can we predict the natural course of femoroacetabular impingement? *Acta Orthop Belg* 77:188-196.
21. Domayer SE, Ziebarth K, Chan J, et al. 2011. Femoroacetabular cam-type impingement: Diagnostic sensitivity and specificity of radiographic views compared to radial mri. *Eur J Radiol* 80:805-810.
22. Jacobsen S, Sonne-Holm S, Lund B, et al. 2004. Pelvic orientation and assessment of hip dysplasia in adults. *Acta Orthop Scand* 75:721-729.
23. Clohisy JC, Carlisle JC, Trousdale R, et al. 2009. Radiographic evaluation of the hip has limited reliability. *Clin Orthop Relat Res* 467:666-675.
24. Clohisy JC, Carlisle JC, Beaulé PE, et al. 2008. A systematic approach to the plain radiographic evaluation of the young adult hip. *J Bone Joint Surg Am* 90 Suppl 4:47-66.
25. Tannast M, Siebenrock KA, Anderson SE. 2007. Femoroacetabular impingement: Radiographic diagnosis--what the radiologist should know. *AJR Am J Roentgenol* 188:1540-1552.
26. Fadul DA, Carrino JA. 2009. Imaging of femoroacetabular impingement. *J Bone Joint Surg Am* 91 Suppl 1:138-143.

27. Bedi A, Dolan M, Hetsroni I, et al. 2011. Surgical treatment of femoroacetabular impingement improves hip kinematics: A computer-assisted model. *Am J Sports Med* 39 Suppl:43S-49S.
28. Tannast M, Kubiak-Langer M, Langlotz F, et al. 2007. Noninvasive three-dimensional assessment of femoroacetabular impingement. *J Orthop Res* 25:122-131.
29. Audenaert EA, Baelde N, Huysse W, et al. 2011. Development of a three-dimensional detection method of cam deformities in femoroacetabular impingement. *Skeletal Radiol* 40:921-927.
30. Bedi A, Dolan M, Magennis E, et al. 2012. Computer-assisted modeling of osseous impingement and resection in femoroacetabular impingement. *Arthroscopy* 28:204-210.
31. Audenaert EA, Mahieu P, Pattyn C. 2011. Three-dimensional assessment of cam engagement in femoroacetabular impingement. *Arthroscopy* 27:167-171.
32. Mavcic B, Pompe B, Antolic V, et al. 2002. Mathematical estimation of stress distribution in normal and dysplastic human hips. *J Orthop Res* 20:1025-1030.
33. Kapron AL, Anderson AE, Aoki SK, et al. 2011. Radiographic prevalence of femoroacetabular impingement in collegiate football players: Aaos exhibit selection. *J Bone Joint Surg Am* 93:e111(111-110).
34. Croft P, Cooper C, Wickham C, Coggon D. 1991. Osteoarthritis of the hip and acetabular dysplasia. *Ann Rheum Dis* 50:308-310.
35. Cooperman DR, Wallensten R, Stulberg SD. 1983. Acetabular dysplasia in the adult. *Clin Orthop Relat Res*:79-85.
36. Hartofilakidis G, Bardakos NV, Babis GC, Georgiades G. 2011. An examination of the association between different morphotypes of femoroacetabular impingement in asymptomatic subjects and the development of osteoarthritis of the hip. *J Bone Joint Surg Br* 93:580-586.
37. Laborie LB, Lehmann TG, Engesaeter IO, et al. 2011. Prevalence of radiographic findings thought to be associated with femoroacetabular impingement in a population-based cohort of 2081 healthy young adults. *Radiology* 260:494-502.
38. Afoke NY, Byers PD, Hutton WC. 1980. The incongruous hip joint. A casting study. *J Bone Joint Surg Br* 62-B:511-514.

39. Cerveri P, Manzotti A, Baroni G. 2012. Patient-specific acetabular shape modelling: Comparison among sphere, ellipsoid and conchoid parameterisations. *Comput Methods Biomech Biomed Engin*.
40. Menschik F. 1997. The hip joint as a conchoid shape. *J Biomech* 30:971-973.
41. Notzli HP, Wyss TF, Stoecklin CH, et al. 2002. The contour of the femoral head-neck junction as a predictor for the risk of anterior impingement. *J Bone Joint Surg Br* 84:556-560.
42. Dudda M, Albers C, Mamisch TC, et al. 2009. Do normal radiographs exclude asphericity of the femoral head-neck junction? *Clin Orthop Relat Res* 467:651-659.
43. Konan S, Rayan F, Haddad FS. 2010. Is the frog lateral plain radiograph a reliable predictor of the alpha angle in femoroacetabular impingement? *J Bone Joint Surg Br* 92:47-50.
44. Meyer DC, Beck M, Ellis T, et al. 2006. Comparison of six radiographic projections to assess femoral head/neck asphericity. *Clin Orthop Relat Res* 445:181-185.
45. Allen BC, Peters CL, Brown NA, Anderson AE. 2010. Acetabular cartilage thickness: Accuracy of three-dimensional reconstructions from multidetector ct arthrograms in a cadaver study. *Radiology* 255:544-552.
46. Anderson AE, Ellis BJ, Maas SA, et al. 2008. Validation of finite element predictions of cartilage contact pressure in the human hip joint. *J Biomech Eng* 130:051008.
47. Anderson AE, Ellis BJ, Maas SA, Weiss JA. 2010. Effects of idealized joint geometry on finite element predictions of cartilage contact stresses in the hip. *J Biomech* 43:1351-1357.
48. Anderson AE, Ellis BJ, Peters CL, Weiss JA. 2008. Cartilage thickness: Factors influencing multidetector ct measurements in a phantom study. *Radiology* 246:133-141.
49. Anderson AE, Peters CL, Tuttle BD, Weiss JA. 2005. Subject-specific finite element model of the pelvis: Development, validation and sensitivity studies. *J Biomech Eng* 127:364-373.

CHAPTER 2

BACKGROUND

2.1 The Human Hip Joint: Anatomy and Function

The human hip is a diarthroidal joint formed at the interface of the proximal head of the femur and the acetabulum, or socket, of the pelvis (Fig. 2.1). The hip connects the upper and lower halves of the body and serves as the largest weight bearing joint of the body, regularly experiencing loads 2.5 to 5 times bodyweight.¹⁻³ Articulation at the hip facilitates a variety of movement patterns, including flexion and extension, abduction and adduction, medial and lateral rotation, and circumduction. Power generated at the hip joint through coordinated muscular contractions facilitates complicated yet energy-efficient motion.⁴

The subsections below provide cursory descriptions of hip joint anatomy and physiology, each of which could be the focus of large bodies of research. In light of the work reported in this dissertation, the intent of each subsection is to highlight important attributes of the hip that relate to its geometry and function.

2.1.1 Pelvis and Femur Bones

The pelvis is comprised of two halves, which are each formed through the fusion of three bones – the ischium, pubis, and ilium. During early development these three

bones converge within the acetabulum to form the triradiate cartilage. The chondro-osseous relationships at the triradiate cartilage allow for integrated acetabular growth concurrent with formation and growth of the femoral head.^{5,6} Closure, or ossification, of the triradiate cartilage occurs during puberty with full fusion by 18 years old.^{7,8} The articulating surface of the acetabulum is horseshoe shaped and concave to allow cupping of the femoral head.^{5,9} Proper formation, expansion, and eventual fusion of the triradiate cartilage are all necessary to ensure a congruent joint interface, appropriate coverage of the femoral head, and overall hip joint stability.^{5,10}

Away from the hip joint itself, each hemipelvis forms stabilizing relationships with the opposing hemipelvis at the pubic symphysis joint, and with the sacrum at the sacroiliac joint. The fibro-cartilaginous pubic symphysis joint forms between the anterior pubis of each hemipelvis. The pubic symphysis is nonsynovial and amphiarthroidal, allowing only slight movement during normal physiological motion.¹¹ The sacroiliac joint, between the lateral sacrum and the posterior medial ilium, facilitates transverse motion (i.e., nodding or nutation) between the pelvis and the sacrum, but motion is limited due to the stabilizing effect of a series of ligaments surrounding the joint and connecting the pelvis and sacrum.

The femur is the longest bone in the body, extending from the hip joint proximally to the knee joint distally. The rounded head of the femur interfaces with the acetabulum, forming the ball-and-socket connection that facilitates a large rotational range of motion in healthy hips. Properly developed, the femoral head can rotate to approximately 120° flexion, 25° extension, 45° abduction, 25° adduction, 15° internal rotation, and 35° external rotation.^{12,13} Distal to the femoral head, the femoral neck

extends infero-laterally and bridges the head to the femoral diaphysis (i.e., shaft). Bony outcroppings in the superior portion of the femoral shaft, known as the greater and lesser trochanters, are the attachment sites of tendons/muscles and ligaments, which are important for stabilization, rotation and abd/adduction of the hip. Distally, the femur ends in rounded condyles that interface with the tibia at the knee joint.

Development of the proximal femoral head occurs during a series of postnatal stages extending into early adulthood. Proper ossification of physeal cartilage in the head, neck and greater trochanter allows the femur to articulate properly within the acetabulum and muscle paths to be directed correctly to produce normal, efficient movement of the hip.⁶ The internal architecture of the femoral head, including trabecular and subchondral bone, allows distribution of physiological loads.^{14,15} Disruption of femoral bone development can detrimentally alter hip biomechanics. For instance, slipping of physeal plates in the femoral head can cause misalignment of the upper and lower halves of the head and are characteristic of diseases such as slipped capital femoral epiphysis (SCFE) and femoroacetabular impingement (FAI), which have both been associated with early cartilage degeneration and osteoarthritis.^{16,17}

2.1.2 Articular Cartilage

The femoral head and acetabulum are each covered with hyaline cartilage that, assisted by intra-articular synovial fluid, facilitates low-friction rotational movement of the hip joint. Articular cartilage layers in healthy adult hips range in thickness from 1.2 to 2.3 mm in the acetabulum and 1.0 to 2.5 mm on the femur.

Although relatively thin, cartilage is able to distribute large loads during daily activities.¹⁸ The mechanical properties of articular cartilage result from its unique structure and composition. An extracellular matrix, consisting primarily of type II collagen and relatively fewer aggregating hydrophilic proteoglycans, provides a highly porous but strong base support structure.^{19,20} The matrix is produced and maintained by chondrocytes, the only cell type present in hyaline cartilage. Compared to other tissues, articular cartilage is relatively avascular with chondrocytes occupying only 2% of the total cartilage volume in adults (10% of wet weight).^{20,21} The remaining components are interstitial water/electrolytes (~60% - 85% of wet weight) and the extracellular matrix.²¹ Because cartilage is largely acellular, avascular and aneural, nutrient delivery is likely facilitated via movement of interstitial fluid in and out of the cartilage matrix.²²

Articular cartilage has a highly ordered structure that is often divided into zones by depth. The superficial zone provides the highest tensile properties found in articular cartilage and contains thin collagen fibrils running parallel to the articular surface and interspersed with elongated, inactive chondrocytes.²³ The middle zone is composed of more spherical chondrocytes and larger collagen fibrils rich with proteoglycans and random orientation.²⁰ Below the middle zone is the deep zone, wherein spheroidal chondrocytes and collagen fibrils are oriented in a columnar fashion perpendicular the articular surface.^{24,25} Finally, a layer of partly calcified cartilage exists in which collagen fibrils create a mechanical fixation between cartilage and underlying subchondral bone.^{20,24}

2.1.3 Acetabular Labrum and Hip Joint Capsule

The acetabular labrum is a fibrocartilaginous structure that spans the length of the acetabular rim. At the inferior gap of the horseshoe shaped acetabulum (i.e., at the acetabular notch), the labrum becomes contiguous with the transverse acetabular ligament. The labrum can increase the surface area of the acetabulum by up to 27% and is thought to assist with load distribution and stabilization of the hip joint.²⁶⁻²⁸ Although unconfirmed, the labrum is also thought to provide a seal around the hip joint that increases hydrostatic fluid pressure, thereby facilitating synovial lubrication and resisting distraction between opposing layers of cartilage.^{29,30}

The ligamentous hip capsule lies outside of the acetabular labrum and connects the proximal femur and pelvis. The capsule has a cylindrical sleeve-like shape and inserts medially into the acetabular rim and laterally at the base of the femoral neck; insertions of the capsule are deeper on the anterior femur than posterior.^{31,32} The most prominent structures of the capsule are the iliofemoral, pubofemoral, and ischiofemoral ligaments, which run longitudinally, and the circumferentially oriented zona orbicularis.³¹ The capsule plays an important role in stabilization of the hip by limiting extension, rotation, and distraction of the femur.³¹⁻³³

2.1.4 Surrounding Musculature

Movement of the hip joint is governed by muscles. Muscles controlling hip motion can be grouped into the gluteal (superficial and deep) region, and the anterior, posterior and medial compartments of the thigh.³⁴

Superficial gluteal muscles, including the gluteus maximus, gluteus minimus, gluteus medius, and tensor fascia latae serve to stabilize the hip and produce extension, medial rotation, lateral rotation and abduction of the femur.³⁴ Muscles deep in the gluteal region (i.e., deep hip rotator muscles) are the piriformis, superior gemellus, obturator internus, inferior gemellus, and quadratus femoris. These muscles originate at different points on the pelvis but share attachments at the greater trochanter, thereby producing lateral rotation of the hip.³⁴

In the anterior compartment of the thigh, iliopsoas (iliacus and psoas major), sartorius, and quadriceps (rectus femoris, vastus lateralis, vastus medialis, vastus intermedius) serve as the major flexors of the hip. Muscles of the medial thigh compartment are primarily hip adductors and include the pectineus, adductor longus, adductor magnus, adductor brevis, gracilis, and obturator externus. Finally, hamstring muscles, including semitendinosus, semimembranosus, and biceps femoris (long and short heads) make up the posterior thigh and are the major extensors of the hip. Contributions from these muscles not only produce rotational movements, but also level and stabilize the pelvis during ambulation.³⁵ The rectus femoris and hamstring muscles are biarticular, meaning that they span the hip as well as the knee, and make important contributions to the rotation and stabilization of each joint.

2.2 Pathologies of the Hip

Abnormal bony anatomy is suspected to detrimentally alter the mechanical environment of the hip by altering both intra-articular contact stresses and muscle forces. Osteoarthritis (OA) often ensues if geometric abnormalities go uncorrected. FAI and

acetabular dysplasia are characterized by abnormal development of the acetabulum and/or femur and have each been associated with soft-tissue damage in the hip joint and early onset of OA.³⁶ The etiology of OA, FAI, and acetabular dysplasia are described in detail below. A general description of clinical diagnostic and intervention strategies each is provided.

2.2.1 Osteoarthritis

OA is symptomatic damage and degeneration of tissues within the hip, especially the articular cartilage. In a healthy state, compressive mechanical loading of the hip is important for maintaining joint health and cartilage chondrocyte viability.³⁷⁻³⁹ When the biomechanical environment of the hip is altered, a chemical imbalance of metabolic and degradative signals occurs, which is exacerbated through initiation of cytokine cascades and the production of inflammatory mediators.^{40,41} Altered mechanical stresses on cartilage have also been shown to increase chondrocyte apoptosis and expression of nitric oxide synthase, which further promotes cartilage degeneration by inhibiting collagen and proteoglycan synthesis, degrading existing collagen matrix, and enhancing cartilage susceptibility to other oxidative injury.^{40,42-44}

As damage to articular cartilages advances, macroscopic signs of OA become clinically apparent. Early symptoms of OA are stiffness and pain surrounding the joint that cause discomfort and reduced range of motion.⁴⁵ Clinically, diagnosis of early OA relies primarily on patient history and physical evaluation, as joint changes may not be detectable radiographically.^{46,47} Experimentally, it has been suggested that cartilage in the early stages of OA swells due to increased hydration of the tissue and up-regulation

of inflammatory mediators.^{40,43} Progression of OA in the hip causes increasing pain as the cartilage structure degrades, begins to thin, and bony changes begin. These changes become apparent on radiographs as sclerotic changes to the femur and acetabulum, osteophyte (i.e., bone spur) formation on the femoral head, and narrowing of the joint space (i.e., the radiographic distance between the femoral head and the acetabulum).^{48,49} Damage to articular cartilage is difficult to arrest, especially when concomitant with damage to the acetabular labrum.^{14,50}

Severe OA is most often treated with total hip arthroplasty. However, other surgical and nonsurgical techniques are emerging that seek to slow or repair cartilage and labrum damage in cases of less advanced OA.²⁴ Nonsurgical techniques vary in nature and effectiveness, but randomized controlled studies have shown modest improvement in patients that have undergone lifestyle interventions (e.g., aquatic therapy, weight loss, acupuncture) and pharmacologic therapy (e.g., nonsteroidal anti-inflammatory drugs).⁴⁹ Surgical interventions have also been moderately successful, and include microfracture, autologous cartilage transplantation, osteoarticular autograft, fibrin gluing, and partial arthroplasty.^{24,51,52} Because of the difficulty associated with cartilage repair, increasing attention is being given to early recognition of OA and precursor diseases like acetabular dysplasia and FAI before substantial cartilage damage has occurred.⁵³⁻⁵⁵

2.2.2 Acetabular Dysplasia

Acetabular dysplasia is characterized by a shallow acetabulum that fails to adequately cover and stabilize the femoral head (Fig. 2.2).^{56,57} Instability is often accompanied with loss of congruency. The shallow and malformed dysplastic hips are

thought to alter joint mechanics and cause degenerative changes to the cartilage and labrum. Specifically, contact forces in dysplastic hips are thought to be more localized (i.e., smaller contact areas), higher, and directed more lateral than those in healthy hips, which may cause overloading and subsequent focal damage to of articular cartilage and the acetabular labrum.⁵⁸

While often thought of as a pediatric disease, dysplasia is suspected to be the underlying cause of primary hip replacements in 30%-50% of patients under 60 years old, likely due to subtle, yet potentially damaging, deformities that are undetected during pediatric screening.^{55,59,60} If dysplasia-related bony abnormalities are missed during screening, the hip takes one of four courses: it may become normal as development proceeds, it may remain intact and relatively stable but retain dysplastic features, it may go on to subluxation and only partial contact between the femur and the acetabulum, or it may completely dislocate and remain in that state.^{57,61}

Diagnosis of dysplasia in adults relies primarily upon patient reported pain and two-dimensional (2D) radiographic measures. For most patients, pain is insidious, becoming progressively worse with time, while others experience acute pain that results from traumatic damage to the acetabular labrum.⁶² Some dysplasia patients experience discomfort in the absence of soft-tissue damage, possibly due to alterations of the surrounding musculature or conscious effort to maintain normal movement, but with abnormal muscle activation and force generation.⁶³ Pain is often felt in the groin or lateral aspect of the hip, with concurrent buttock pain and mechanical symptoms such as limping, or catching, clicking, popping and locking of the hip.⁶²

A number of surgical and nonsurgical interventions have been proposed to improve stability, reduce pain, and extend the lifetime of the dysplastic hip. Patients presenting with minimal symptoms and no obvious indication of soft-tissue degeneration may be given nonsteroidal anti-inflammatory agents and advised to limit or avoid high-impact activities. Surgical techniques aimed to preserve the hip include arthroscopic correction of minor chondro-labral damage, debridement of abnormal bony growths, and/or release of the psoas tendon to reduce clicking and locking.^{64,65} However, arthroscopic surgery for severe cases of dysplasia may not be recommended due to an increased risk of rapid OA.^{66,67} Instead, open surgeries, including a number of different pelvis osteotomy techniques seek to reorient the acetabulum to improve coverage of the femur and stabilize hip.⁶⁸⁻⁷⁰ Follow-up results of such osteotomies have been favorable with respect to pain alleviation and joint stability, but whether or not surgical intervention restores hip biomechanics to a normal state or consistently delays OA development has not been firmly established.^{67,71} This is, in part, because of the lack of understanding of not only dysplastic hip biomechanics, but the mechanics of healthy hips as well.

2.2.3 Femoroacetabular Impingement

Like dysplasia, FAI is characterized by deformities in the shape of the hip joint. Specifically, hips with FAI are thought to have excess bony growths on the femoral head and/or the acetabular rim, which cause premature abutment between the proximal femur and the acetabulum during hip articulation.^{53,72} When a bony growth occurs primarily on the head and neck of the femur, it is termed “cam FAI.”⁵³ Impingement due to excess bone along the rim of the acetabulum is termed “pincer FAI.”⁵³ While cam and pincer

FAI can occur in isolation, many patients present with both types of FAI and are termed “mixed FAI” cases.

While the effects of dysplasia have been documented for over a century, the association between FAI and early development of OA was not appreciated until recently.⁵³ Although, FAI has long existed before the current understanding of the disease was established, impingement cases were anecdotally reported only as residuals from childhood diseases such as slipped capital femoral epiphysis (SCFE) or pediatric acetabular dysplasia.^{72,73} It was largely the work of Reinhold Ganz and associates in Switzerland that presented the concept of FAI as a mechanical initiator of OA due to subtle geometric alterations and malorientation of the hip in the absence of grossly obvious childhood disease.^{36,53} The mechanisms of FAI may differ in predominantly cam versus pincer FAI, but each are thought to cause repetitive collisions that damage the acetabular labrum and articular cartilage.⁷⁴

In cases of cam FAI the normally concave junction of the femoral head-neck junction is flattened or convex, which reduces the range of motion the femur can achieve when articulating within the acetabulum (Fig. 2.3).^{75,76} Instead of rotating freely, the deformed femur abuts against the lateral acetabular rim and/or shears into the acetabular cavity, causing damage to cartilage on the femoral head, outside-in delamination of the acetabular cartilage where it joins the acetabular labrum, and tearing of the labrum.^{53,74,77-}

81

In cases of pincer FAI the acetabular rim is thought to have excess bone or be maloriented such that the acetabulum collides with the femoral neck or lateral head. Cases of pincer FAI can be caused by a globally over-covering acetabulum, known as

protrusio acetabuli, or focal over-coverage of the anterior femur (a condition often associated with a form of dysplasia known as acetabular retroversion).^{53,72,82-84} Contact between the acetabulum and the femur deforms or crushes the labrum; chronically or in traumatic collisions the labrum can fray or tear, with subsequent damage to the articular cartilage.^{36,78,84,85}

The etiology of FAI deformities is unknown. Some cam lesions may truly be abnormalities of the capital femoral epiphysis secondary to SCFE, but many lesions occur in the absence of abnormal growth plate orientation typical of SCFE.^{16,17} The cause of acetabular over-growth is also poorly understood, but could result from metabolic or inflammatory diseases that contribute to remodeling and ossification of the acetabular rim and labrum.⁷³

Physical examinations are the first diagnostic tool when identifying FAI. FAI patients who present in the clinic are often young adults with groin pain that becomes progressively worse and is exacerbated with physical activity.^{79,86,87} In contrast to dysplasia patients, FAI patients do not generally have feelings of instability; instead, pain and reduced range of motion are the mainstay. Physicians trained to identify FAI will perform basic physical examinations to determine pain during hip flexion and internal rotation, which have been shown to indicate anterior FAI in upwards of 90% of patients.^{79,86} However, physical examinations cannot isolate the location of geometric deformities that may be causing impingement and are insufficient for prescribing an appropriate intervention. Furthermore, many clinical practitioners are still unfamiliar with the physical manifestations of FAI and may inadvertently come to an improper diagnosis and prescribe ineffective interventions (e.g., hernia surgery).⁸⁷

When surgical intervention is believed warranted for FAI it can be arthroscopic or open, depending upon surgeon preference and the anticipated type and severity of deformities. Arthroscopic techniques focus primarily on debridement of anterior deformities of the femoral head and debridement or repair of the acetabular rim and labrum.^{88,89} If the surgeon seeks a more complete intraoperative view of the hip joint or intends to address FAI deformities that extend to the posterior half of the joint (e.g., global pincer FAI, acetabular retroversion), open or limited-open surgery may be appropriate.^{90,91} While many surgeries have successfully improved patient comfort and show promising short-term results, inefficient correction of FAI (e.g., inadequate debridement of a cam lesion) is still common and results in residual pain and a need for additional surgery.⁹²⁻⁹⁴

2.3 Measurement of Hip Morphology

2.3.1 Radiographic Measures

The most common radiographic measure used to diagnose acetabular dysplasia is the lateral center edge angle of Wiberg, which gives an indication of the shallowness of the acetabulum (Fig. 2.4).⁹⁵ Reports of normal ranges for this angle have been debated but a lateral center edge angle $<20^{\circ}$ is most commonly accepted as being indicative of dysplasia.⁹⁶ Other radiographic measures of dysplasia are used to various degrees by different clinics and include the acetabular index, extrusion index, acetabular depth ratio, and the acetabular angle of Sharp.^{62,96,97} Unfortunately, there is no consensus as to which radiographic measures should be used. Also, studies suggest that many of these measures of dysplasia cannot reliably predict if a patient will develop OA.^{56,96,98-100}

Many radiographic measures have been proposed to identify FAI deformities.^{101,102} By nature, most radiographic measures are 2D and are obviously limited in their ability to describe what are inherently three-dimensional (3D) deformities (Fig. 2.4). As a result, there is considerable debate within the literature about the reliability of various 2D views and corresponding measures.¹⁰³⁻¹⁰⁷ Measures of geometry that are derived from volumetric image sets (i.e., CT or MRI) have also been proposed.¹⁰⁸⁻¹¹⁰ Unfortunately, most such measures are taken on a single image or image plane, which reverts back to a 2D description. Furthermore, like measures of dysplasia, radiographic suggestions of FAI do not definitively predict soft-tissue damage to the joint or early development of OA.¹¹¹⁻¹¹³ Finally, because of the limitations of traditional 2D diagnostic techniques, much surgical decision making (e.g., where and how much to debride a cam deformity) is done during surgery itself, which relies largely on intraoperative range of motion testing and surgeon experience. Additional empirical evidence and objective data are needed to improve our understanding of the mechanical and morphological differences between dysplastic, FAI and healthy hips. These data could provide the definitive evidence necessary to directly link FAI and dysplasia with OA as well as identify which factors deserve attention for preoperative surgical planning and postoperative assessments of treatment efficacy.

2.3.2 Three-dimensional Characterization of Hip Morphology

Recently, there has been an increase in studies that seek to characterize FAI, especially cam FAI, in 3D. Some studies use surface reconstructions of bony hip geometry and arbitrary joint angles to theorize where impingement may occur.¹¹⁴⁻¹¹⁷ A

few studies have also proposed new 3D methods for characterizing cam lesion morphology.^{118,119} These studies have made great strides in improving our understanding of FAI. However, crucial limitations still exist, such as assumptions about the ideal shape of the femoral head and a lack of techniques that objectively describe bony morphology and are also easy to interpret in a clinical setting.^{114-117,119} For example, there currently is not a methodology to objectively isolate the femoral head from the neck and identify the 3D location and size of cam-type deformities. Furthermore, while there is an increasing understanding that natural femoral heads do not conform to an ideal geometry, 3D quantitative descriptions of deviations from ideal geometries, such as the sphere, have not been made available.

Also, despite their limitations, 2D measurements of radiographs and radial CT/MR images continue to be the major diagnostic tools for detection and surgical planning of both FAI and dysplasia. Because radiographs are relatively inexpensive and can be quickly obtained, they will continue to have a prominent clinical role. Thus, in addition to the need for new measures to characterize FAI deformities in 3D, it is also important to understand how such measures relate to 2D radiographic measures and to determine which 2D measures are best able to describe bony hip deformities.

An area of 3D computational modeling that shows promise for describing FAI is statistical shape modeling (SSM). SSM provides methods for quantitatively describing complex geometric variation without any assumption about shape or subjective measurements (e.g., radiographic measurements). Relevant to cam FAI, SSM can be used to consider the shape of the entire proximal femur, which may be advantageous for identifying geometric abnormalities that are subtle or extend beyond the femoral head.

Most SSM strategies work by distributing labeled point sets across representative shapes, based on anatomic landmarks, finite element meshes or point-to-point minimization of distance and entropy.¹²⁰⁻¹²³ Regardless of the method, by optimizing and comparing the positional configurations of the labeled points, SSM can quantify and visualize geometric variation existing within a population. Application of SSM to orthopaedics is still limited but has included analyses of tibiofemoral and patellofemoral joints and methods to reconstruct femur or pelvis shape from sparse image data.^{122,124-126} Because many orthopaedic diseases involve abnormal or altered geometry, SSM has great potential in this field.

2.4 Measurement of Hip Mechanics

While identification and characterization of abnormal geometry in the hip improves the process to diagnose and treat FAI and dysplasia, there is still much to be known about how hip geometry affects joint mechanics. The following sections briefly describe experimental and computational research that has been performed to quantify intra-articular and whole joint (kinematics, kinetics, and muscle forces) hip biomechanics. In accordance with the goals of this dissertation, focus is upon computational modeling of cartilage contact mechanics and musculoskeletal modeling of the hip. Because each modeling technique draws from extensive prior work in very distinct disciplines, this report does not attempt to comprehensively describe the history and development of each. For an in-depth study of cartilage contact modeling of the hip, the reader is directed to the review article by Henak et al.¹²⁷ For in depth discussion of common techniques and

requirements in musculoskeletal modeling, the reader is directed to reviews by Pandy and Andriacchi.^{4,128}

2.4.1 Intra-articular Cartilage Contact Mechanics

Direct measurement of cartilage contact mechanics can be achieved using in vitro or in vivo experimental techniques. In vitro methods traditionally involve dissection and disarticulation of cadaveric joints, followed by placement of pressure sensitive film or electronic pressure sensors between articulating surfaces.¹²⁹⁻¹³¹ The articulating surfaces are then loaded to predetermined boundary and loading conditions. Using this approach, loading of the hip joint is inherently affected by the type of loading scheme involved and the joint may not seat experimentally as it does physiologically. Furthermore, it is difficult to quantify contact stress on the entire articulating surface with these techniques, and there is a limited range of stresses that can be measured. In vivo studies of intra-articular joint mechanics are highly complicated. They involve implantation of instrumented hip prostheses that measure equivalent hip joint reaction forces during activities of daily living.^{1,132,133} Such in vivo measurements can only approximate the true cartilage stresses since one joint surface has been replaced with a perfectly shaped metal implant. Also, in vitro and in vivo techniques are inherently invasive, yield data only at the measurement area, and have been difficult to visualize for clinical interpretation.

Computational modeling offers the ability to estimate cartilage mechanics for individual joints, and provide estimates for the entire contact interface. Prior computational approaches have included the discrete element analysis (DEA) technique¹³⁴⁻¹³⁶ and the finite element (FE) method.¹³⁷⁻¹³⁹ Early computational models of

intra-articular hip mechanics were two-dimensional and/or assumed the hip joint to be perfectly round and congruent.¹³⁷ Such assumptions may have been necessary due to limitations in the technology at the time. However, modeling studies persist with the spherical hip assumption, and as a result, model estimations of contact stresses do not match experimental results and are severely limited in their ability to extract clinically relevant data.^{136,140,141}

Some analysts have used volumetric imaging modalities such as CT to represent the subject-specific geometry of the hip.¹⁴²⁻¹⁴⁴ Unfortunately, models which incorporate subject-specific geometry, including bone and cartilage, are relatively rare. Presumably, this is due to the difficulty in creating meshes that accurately capture variations in subject geometry and the complexity of multistructure, multimaterial models in contact. As a result, most models of intra-articular contact mechanics that include subject-specific bone geometry have primarily been proof of concept or parameter studies. Perhaps most critical is the fact that most contact models of the hip lack validation against experimentally derived data.¹⁴⁵

Anderson et al. developed a novel finite element (FE) model of the hip that incorporated subject-specific bone and cartilage geometry and produced contact stress results in good agreement when directly compared to experimental data.¹⁴⁶ In the validated model of Anderson et al., subject-specific 3D reconstructions of the pelvis and proximal femur bone and cartilage were generated from segmentation of CT image data. The 3D reconstructions were then used to create finite element meshes of the bone and cartilage. Experiment-based material properties and constitutive models were assigned to the meshes to represent the behavior of the different tissues during compressive loading.

Finally, the hip joint was loaded using in vivo kinematic and kinetic data and estimations of cartilage contact stresses under different loading conditions were calculated using an implicit finite element solver. During development of the model, Anderson et al. provided evidence of model quality with respect to segmentation accuracy,¹⁴⁷⁻¹⁴⁹ material behavior during compressive loading at the rate expected during the simulated activities^{147,150} and mesh element choice and refinement.¹⁴⁶ Most importantly, in a cadaver model, the protocol produced cartilage contact stress magnitudes and distributions that were in agreement with directly measured in vitro contact stresses.¹⁴⁶ The validated model of Anderson et al. served as the framework for the finite element modeling of contact stresses in live subjects described in this dissertation.

2.4.2 Whole-joint Mechanics (Kinematics and Kinetics)

Altered biomechanics are regarded as the primary initiators of hip OA, so attention often focuses on intra-articular abnormalities. However, FAI and dysplasia are complex pathomechanical diseases, with contributions to disease progression also arising from the ligaments and muscles responsible for stabilizing and moving the joint. Studies addressing muscular changes in FAI and dysplasia patients are scarce but suggest that FAI patients may indeed exhibit abnormal muscle activations and forces.^{63,151,152} In an MRI study, Babst et al. found that the iliocapsularis muscle, which runs anterior to the hip capsule, was hypertrophied in patients with acetabular dysplasia, suggesting that this muscle experiences excessive activation in dysplasia patients to stabilize the joint.⁶³ Cassertelli et al. used dynamometry and EMG to estimate isometric maximum voluntary contraction strength and found hip muscles to be weaker in FAI patients compared to

matched controls.¹⁵² While these studies suggest alterations to muscle forces in dysplasia and FAI patients, estimates of muscles forces for these populations during routine daily activities have not been reported. Furthermore, direct measurement of muscle forces in vivo is not currently possible.

A few studies have reported kinematics and kinetics, as represented by joint angles and moments, in dysplastic and FAI groups. The majority of such studies have focused on changes in gait after corrective surgery for FAI and dysplasia and found a return to more normal joint angles postsurgery.^{116,153-155} Romano et al. reported the kinematic and kinetic patterns of patients with varying severity of dysplasia and found reduced hip extension for all subjects on the affected leg compared to the contralateral leg.¹⁵⁶ Other studies have reported that cam FAI patients have reduced sagittal range of motion (ROM) and lower hip abduction peaks compared to control subjects.^{157,158} These studies make progress toward establishing relationships between altered hip geometry and mechanics. However, muscular force and activation differences between controls and dysplasia or FAI patients are still unknown.

2.4.3 Muscle Force Modeling

Musculoskeletal modeling allows estimation of muscle forces by coupling experimentally gathered in vivo motion data with muscle representations derived from in vitro studies of muscle architecture and strength. Musculoskeletal modeling strategies are diverse and an explanation of each is not within the scope of the current dissertation. The interested reader is directed to review articles by Pandy et al., which provide details of the evolution and much of the theory involved with musculoskeletal modeling.^{4,128}

Computational determination of muscle function requires accurate measurements of external forces applied to the body, accurate measurements of body motion (e.g., skin marker trajectories, joint angles), and knowledge of muscle and joint contact loading.⁴ Motion and external force data can be collected using traditional gait analysis equipment such as force plates and video-based motion capture from retro-reflective skin markers. Motion data may also be collected using newer technology such as dual fluoroscopy, which reduces artifact from soft-tissue, but exposes subjects to ionizing radiation.¹⁵⁹ Using the in vivo data, musculoskeletal modeling programs (e.g., AnyBody, OpenSim, LifeMOD) incorporate experimental data about muscle behavior (e.g., maximum isometric forces, physiological cross-sectional areas, pennation angles, tendon slack lengths, muscle activation dynamics) and optimization theory to resolve individual muscle and joint contact loading.¹⁶⁰⁻¹⁶² Validation of musculoskeletal models is challenging.¹⁶³ Errors from input data, modeling assumptions about anatomy, and resolution of indeterminate force problems (i.e., many muscles spanning a single joint) can each contribute to errors in final model estimations. In this dissertation, OpenSim software was used to demonstrate the feasibility of using musculoskeletal modeling to study whole joint and muscle mechanics at the hip.¹⁶⁴ Specifically, an OpenSim model was modified and then used to calculate joint angles, moments, muscle forces, and joint reaction forces at the hip. Results were compared to in vivo electromyography (EMG) data and values from the literature. The model was then applied to cohorts of healthy subjects and acetabular dysplasia patients. The musculoskeletal modeling study comprises the final of five studies completed to develop tools and further our

understanding of the morphology and mechanics of human hips, for improved diagnosis and treatment of FAI and acetabular dysplasia patients.

2.5 References

1. Bergmann G, Deuretzbacher G, Heller M, et al. 2001. Hip contact forces and gait patterns from routine activities. *J Biomech* 34:859-871.
2. Hashimoto N, Ando M, Yayama T, et al. 2005. Dynamic analysis of the resultant force acting on the hip joint during level walking. *Artif Organs* 29:387-392.
3. Schwachmeyer V, Damm P, Bergmann G. 2013. In vivo hip joint loading during post-operative physiotherapeutic exercises. In, 2013 Annual Meeting of the Orthopaedic Research Society. San Antonio, TX: Orthopaedic Research Society.
4. Pandy MG, Andriacchi TP. 2010. Muscle and joint function in human locomotion. *Annu Rev Biomed Eng* 12:401-433.
5. Ponseti IV. 1978. Growth and development of the acetabulum in the normal child. Anatomical, histological, and roentgenographic studies. *J Bone Joint Surg Am* 60:575-585.
6. Lee MC, Eberson CP. 2006. Growth and development of the child's hip. *Orthop Clin North Am* 37:119-132.
7. Dimeglio A. 2001. Growth in pediatric orthopaedics. *J Pediatr Orthop* 21:549-555.
8. Ogden JA. 1990. Skeletal injury in the child. W.B. Saunders Company, Philadelphia, PA.
9. Field RE, Rajakulendran K. 2011. The labro-acetabular complex. *J Bone Joint Surg Am* 93 Suppl 2:22-27.
10. Ralis Z, McKibbin B. 1973. Changes in shape of the human hip joint during its development and their relation to its stability. *J Bone Joint Surg Br* 55:780-785.
11. Becker I, Woodley SJ, Stringer MD. 2010. The adult human pubic symphysis: A systematic review. *J Anat* 217:475-487.
12. Roach KE, Miles TP. 1991. Normal hip and knee active range of motion: The relationship to age. *Phys Ther* 71:656-665.

13. Norkin CC. 2009. Measurement of joint motion: A guide to goniometry. F.A. Davis Company, Philadelphia, PA.
14. Bowman KF, Jr., Fox J, Sekiya JK. 2010. A clinically relevant review of hip biomechanics. *Arthroscopy* 26:1118-1129.
15. Radin EL. 1995. Osteoarthritis--the orthopedic surgeon's perspective. *Acta Orthop Scand Suppl* 266:6-9.
16. Goodman DA, Feighan JE, Smith AD, et al. 1997. Subclinical slipped capital femoral epiphysis. Relationship to osteoarthritis of the hip. *J Bone Joint Surg Am* 79:1489-1497.
17. Siebenrock KA, Wahab KH, Werlen S, et al. 2004. Abnormal extension of the femoral head epiphysis as a cause of cam impingement. *Clin Orthop Relat Res*:54-60.
18. Shepherd DE, Seedhom BB. 1999. Thickness of human articular cartilage in joints of the lower limb. *Ann Rheum Dis* 58:27-34.
19. Ateshian GA, Lai WM, Zhu WB, Mow VC. 1994. An asymptotic solution for the contact of two biphasic cartilage layers. *J Biomech* 27:1347-1360.
20. Poole AR, Kojima T, Yasuda T, et al. 2001. Composition and structure of articular cartilage: A template for tissue repair. *Clin Orthop Relat Res*:S26-33.
21. Cohen NP, Foster RJ, Mow VC. 1998. Composition and dynamics of articular cartilage: Structure, function, and maintaining healthy state. *J Orthop Sports Phys Ther* 28:203-215.
22. O'Hara BP, Urban JP, Maroudas A. 1990. Influence of cyclic loading on the nutrition of articular cartilage. *Ann Rheum Dis* 49:536-539.
23. Kempson GE, Muir H, Pollard C, Tuke M. 1973. The tensile properties of the cartilage of human femoral condyles related to the content of collagen and glycosaminoglycans. *Biochimica et Biophysica Acta (BBA) - General Subjects* 297:456-472.
24. Newman AP. 1998. Articular cartilage repair. *Am J Sports Med* 26:309-324.
25. Venn M, Maroudas A. 1977. Chemical composition and swelling of normal and osteoarthrotic femoral head cartilage. I. Chemical composition. *Ann Rheum Dis* 36:121-129.

26. Tan V, Seldes RM, Katz MA, et al. 2001. Contribution of acetabular labrum to articulating surface area and femoral head coverage in adult hip joints: An anatomic study in cadavera. *Am J Orthop (Belle Mead NJ)* 30:809-812.
27. Henak CR, Ellis BJ, Harris MD, et al. 2011. Role of the acetabular labrum in load support across the hip joint. *J Biomech* 44:2201-2206.
28. Konrath GA, Hamel AJ, Olson SA, et al. 1998. The role of the acetabular labrum and the transverse acetabular ligament in load transmission in the hip. *J Bone Joint Surg Am* 80:1781-1788.
29. Crawford MJ, Dy CJ, Alexander JW, et al. 2007. The 2007 frank stinchfield award. The biomechanics of the hip labrum and the stability of the hip. *Clin Orthop Relat Res* 465:16-22.
30. Ferguson SJ, Bryant JT, Ganz R, Ito K. 2003. An in vitro investigation of the acetabular labral seal in hip joint mechanics. *J Biomech* 36:171-178.
31. Jenkins DB. 2009. Hollinshead's functional anatomy of the limbs and back. Saunders Elsevier, St. Louis, MO.
32. Stewart KJ, Edmonds-Wilson RH, Brand RA, Brown TD. 2002. Spatial distribution of hip capsule structural and material properties. *J Biomech* 35:1491-1498.
33. Ito H, Song Y, Lindsey DP, et al. 2009. The proximal hip joint capsule and the zona orbicularis contribute to hip joint stability in distraction. *J Orthop Res* 27:989-995.
34. Morton D, Albertine K, Foreman B. 2011. The big picture: Gross anatomy. McGraw Hill, New York.
35. Krebs DE, Robbins CE, Lavine L, Mann RW. 1998. Hip biomechanics during gait. *J Orthop Sports Phys Ther* 28:51-59.
36. Ganz R, Leunig M, Leunig-Ganz K, Harris WH. 2008. The etiology of osteoarthritis of the hip: An integrated mechanical concept. *Clin Orthop Relat Res* 466:264-272.
37. Guilak F, Fermor B, Keefe FJ, et al. 2004. The role of biomechanics and inflammation in cartilage injury and repair. *Clin Orthop Relat Res*:17-26.
38. Grodzinsky AJ, Levenston ME, Jin M, Frank EH. 2000. Cartilage tissue remodeling in response to mechanical forces. *Annu Rev Biomed Eng* 2:691-713.

39. Wilkins RJ, Browning JA, Urban JP. 2000. Chondrocyte regulation by mechanical load. *Biorheology* 37:67-74.
40. Krasnokutsky S, Attur M, Palmer G, et al. 2008. Current concepts in the pathogenesis of osteoarthritis. *Osteoarthritis Cartilage* 16 Suppl 3:S1-3.
41. Lee JH, Fitzgerald JB, Dimicco MA, Grodzinsky AJ. 2005. Mechanical injury of cartilage explants causes specific time-dependent changes in chondrocyte gene expression. *Arthritis Rheum* 52:2386-2395.
42. Fermor B, Weinberg JB, Pisetsky DS, et al. 2001. The effects of static and intermittent compression on nitric oxide production in articular cartilage explants. *J Orthop Res* 19:729-737.
43. Jeffrey JE, Gregory DW, Aspden RM. 1995. Matrix damage and chondrocyte viability following a single impact load on articular cartilage. *Arch Biochem Biophys* 322:87-96.
44. Loening AM, James IE, Levenston ME, et al. 2000. Injurious mechanical compression of bovine articular cartilage induces chondrocyte apoptosis. *Arch Biochem Biophys* 381:205-212.
45. Manek NJ, Lane NE. 2000. Osteoarthritis: Current concepts in diagnosis and management. *Am Fam Physician* 61:1795-1804.
46. Swagerty DL, Jr., Hellinger D. 2001. Radiographic assessment of osteoarthritis. *Am Fam Physician* 64:279-286.
47. Cibulka MT, Threlkeld J. 2004. The early clinical diagnosis of osteoarthritis of the hip. *J Orthop Sports Phys Ther* 34:461-467.
48. Neuman P, Hulth A, Linden B, et al. 2003. The role of osteophytic growth in hip osteoarthritis. *Int Orthop* 27:262-266.
49. Lane NE. 2007. Clinical practice. Osteoarthritis of the hip. *N Engl J Med* 357:1413-1421.
50. McCarthy JC, Noble PC, Schuck MR, et al. 2001. The otto e. Aufranc award: The role of labral lesions to development of early degenerative hip disease. *Clin Orthop Relat Res*:25-37.
51. Sekiya JK, Martin RL, Lesniak BP. 2009. Arthroscopic repair of delaminated acetabular articular cartilage in femoroacetabular impingement. *Orthopedics* 32.
52. Hunziker EB. 2002. Articular cartilage repair: Basic science and clinical progress. A review of the current status and prospects. *Osteoarthritis Cartilage* 10:432-463.

53. Ganz R, Parvizi J, Beck M, et al. 2003. Femoroacetabular impingement: A cause for osteoarthritis of the hip. *Clin Orthop Relat Res*:112-120.
54. Nakamura J, Oinuma K, Ohtori S, et al. 2013. Distribution of hip pain in osteoarthritis patients secondary to developmental dysplasia of the hip. *Mod Rheumatol* 23:119-124.
55. Harris WH. 1986. Etiology of osteoarthritis of the hip. *Clin Orthop Relat Res*:20-33.
56. Cooperman DR, Wallensten R, Stulberg SD. 1983. Acetabular dysplasia in the adult. *Clin Orthop Relat Res*:79-85.
57. Dezateux C, Rosendahl K. 2007. Developmental dysplasia of the hip. *Lancet* 369:1541-1552.
58. Russell ME, Shivanna KH, Grosland NM, Pedersen DR. 2006. Cartilage contact pressure elevations in dysplastic hips: A chronic overload model. *J Orthop Surg Res* 1:6.
59. Furnes O, Lie SA, Espehaug B, et al. 2001. Hip disease and the prognosis of total hip replacements. A review of 53,698 primary total hip replacements reported to the norwegian arthroplasty register 1987-99. *J Bone Joint Surg Br* 83:579-586.
60. David TJ, Poynor M, Simm S, et al. 1983. Reasons for late detection of hip dislocation in childhood. *The Lancet* 322:147-149.
61. Weinstein SL. 1998. The sequelae of pediatric hip disease. In: Callaghan, J.J. editor, *The adult hip*. Philadelphia: Lippincott-Raven Publishers, pp. 409-435.
62. Nunley RM, Prather H, Hunt D, et al. 2011. Clinical presentation of symptomatic acetabular dysplasia in skeletally mature patients. *J Bone Joint Surg Am* 93 Suppl 2:17-21.
63. Babst D, Steppacher SD, Ganz R, et al. 2011. The iliocapsularis muscle: An important stabilizer in the dysplastic hip. *Clin Orthop Relat Res* 469:1728-1734.
64. Byrd JW, Jones KS. 2003. Hip arthroscopy in the presence of dysplasia. *Arthroscopy* 19:1055-1060.
65. Ilizaliturri VMJ, Reveles-Castillo R, Ramos-Aviña C, Camacho-Galindo J. 2005. Arthroscopy for hip dysplasia: Indications and limitations. *Techniques in Orthopaedics* 20:52-55.

66. Parvizi J, Bican O, Bender B, et al. 2009. Arthroscopy for labral tears in patients with developmental dysplasia of the hip: A cautionary note. *J Arthroplasty* 24:110-113.
67. Matsuda DK, Khatod M. 2012. Rapidly progressive osteoarthritis after arthroscopic labral repair in patients with hip dysplasia. *Arthroscopy* 28:1738-1743.
68. Sanchez-Sotelo J, Trousdale RT, Berry DJ, Cabanela ME. 2002. Surgical treatment of developmental dysplasia of the hip in adults: I. Nonarthroplasty options. *J Am Acad Orthop Surg* 10:321-333.
69. Clohisy JC, Barrett SE, Gordon JE, et al. 2006. Periacetabular osteotomy in the treatment of severe acetabular dysplasia. Surgical technique. *J Bone Joint Surg Am* 88 Suppl 1 Pt 1:65-83.
70. Ganz R, Klaue K, Vinh TS, Mast JW. 1988. A new periacetabular osteotomy for the treatment of hip dysplasias. Technique and preliminary results. *Clin Orthop Relat Res*:26-36.
71. Steppacher SD, Tannast M, Ganz R, Siebenrock KA. 2008. Mean 20-year followup of bernese periacetabular osteotomy. *Clin Orthop Relat Res* 466:1633-1644.
72. Leunig M, Beaulé PE, Ganz R. 2009. The concept of femoroacetabular impingement: Current status and future perspectives. *Clin Orthop Relat Res* 467:616-622.
73. Leunig M, Ganz R. 2009. FAI - concept and etiology. *Der Orthopäde* 38:394-401.
74. Beck M, Kalhor M, Leunig M, Ganz R. 2005. Hip morphology influences the pattern of damage to the acetabular cartilage: Femoroacetabular impingement as a cause of early osteoarthritis of the hip. *J Bone Joint Surg Br* 87:1012-1018.
75. Beaulé PE, Harvey N, Zaragoza E, et al. 2007. The femoral head/neck offset and hip resurfacing. *J Bone Joint Surg Br* 89:9-15.
76. Meermans G, Konan S, Haddad FS, Witt JD. 2010. Prevalence of acetabular cartilage lesions and labral tears in femoroacetabular impingement. *Acta Orthop Belg* 76:181-188.
77. Kassarian A, Brisson M, Palmer WE. 2007. Femoroacetabular impingement. *Eur J Radiol* 63:29-35.
78. Tannast M, Goricki D, Beck M, et al. 2008. Hip damage occurs at the zone of femoroacetabular impingement. *Clin Orthop Relat Res* 466:273-280.

79. Sink EL, Gralla J, Ryba A, Dayton M. 2008. Clinical presentation of femoroacetabular impingement in adolescents. *J Pediatr Orthop* 28:806-811.
80. Wagner S, Hofstetter W, Chiquet M, et al. 2003. Early osteoarthritic changes of human femoral head cartilage subsequent to femoro-acetabular impingement. *Osteoarthritis Cartilage* 11:508-518.
81. Siebenrock KA, Schoeniger R, Ganz R. 2003. Anterior femoro-acetabular impingement due to acetabular retroversion. Treatment with periacetabular osteotomy. *J Bone Joint Surg Am* 85-A:278-286.
82. Reynolds D, Lucas J, Klaue K. 1999. Retroversion of the acetabulum. A cause of hip pain. *J Bone Joint Surg Br* 81:281-288.
83. Krych AJ, Thompson M, Larson CM, et al. 2012. Is posterior hip instability associated with cam and pincer deformity? *Clin Orthop Relat Res* 470:3390-3397.
84. Leunig M, Nho SJ, Turchetto L, Ganz R. 2009. Protrusio acetabuli: New insights and experience with joint preservation. *Clin Orthop Relat Res* 467:2241-2250.
85. Beaulé PE, O'Neill M, Rakhra K. 2009. Acetabular labral tears. *J Bone Joint Surg Am* 91:701-710.
86. Philippon MJ, Maxwell RB, Johnston TL, et al. 2007. Clinical presentation of femoroacetabular impingement. *Knee Surg Sports Traumatol Arthrosc* 15:1041-1047.
87. Clohisy JC, Knaus ER, Hunt DM, et al. 2009. Clinical presentation of patients with symptomatic anterior hip impingement. *Clin Orthop Relat Res* 467:638-644.
88. Philippon MJ, Schenker ML. 2006. Arthroscopy for the treatment of femoroacetabular impingement in the athlete. *Clin Sports Med* 25:299-308, ix.
89. Buchler L, Neumann M, Schwab JM, et al. 2013. Arthroscopic versus open cam resection in the treatment of femoroacetabular impingement. *Arthroscopy*.
90. Peters CL, Erickson JA. 2006. Treatment of femoro-acetabular impingement with surgical dislocation and debridement in young adults. *J Bone Joint Surg Am* 88:1735-1741.
91. Clohisy JC, McClure JT. 2005. Treatment of anterior femoroacetabular impingement with combined hip arthroscopy and limited anterior decompression. *Iowa Orthop J* 25:164-171.

92. Beaulé PE, Le Duff MJ, Zaragoza E. 2007. Quality of life following femoral head-neck osteochondroplasty for femoroacetabular impingement. *J Bone Joint Surg Am* 89:773-779.
93. Philippon MJ, Schenker ML, Briggs KK, et al. 2007. Revision hip arthroscopy. *Am J Sports Med* 35:1918-1921.
94. Ward JP, Rogers P, Youm T. 2012. Failed hip arthroscopy: Causes and treatment options. *Orthopedics* 35:612-617.
95. Wiberg G. 1939. Studies on dysplastic acetabula and congenital subluxation of the hip joint. *Acta Chir Scand*. 83 28-38.
96. Harris-Hayes M, Royer NK. 2011. Relationship of acetabular dysplasia and femoroacetabular impingement to hip osteoarthritis: A focused review. *PM R* 3:1055-1067 e1051.
97. Sharp IK. 1961. Acetabular dysplasia: The acetabular angle. *J Bone Joint Surg Br* 43-B:268-272.
98. Murphy SB, Ganz R, Muller ME. 1995. The prognosis in untreated dysplasia of the hip. A study of radiographic factors that predict the outcome. *J Bone Joint Surg Am* 77:985-989.
99. Birrell F, Silman A, Croft P, et al. 2003. Syndrome of symptomatic adult acetabular dysplasia (saad syndrome). *Ann Rheum Dis* 62:356-358.
100. Hoaglund FT, Steinbach LS. 2001. Primary osteoarthritis of the hip: Etiology and epidemiology. *J Am Acad Orthop Surg* 9:320-327.
101. Clohisy JC, Carlisle JC, Beaulé PE, et al. 2008. A systematic approach to the plain radiographic evaluation of the young adult hip. *J Bone Joint Surg Am* 90 Suppl 4:47-66.
102. Tannast M, Siebenrock KA, Anderson SE. 2007. Femoroacetabular impingement: Radiographic diagnosis--what the radiologist should know. *AJR Am J Roentgenol* 188:1540-1552.
103. Domayer SE, Ziebarth K, Chan J, et al. 2011. Femoroacetabular cam-type impingement: Diagnostic sensitivity and specificity of radiographic views compared to radial mri. *Eur J Radiol* 80:805-810.
104. Clohisy JC, Carlisle JC, Trousdale R, et al. 2009. Radiographic evaluation of the hip has limited reliability. *Clin Orthop Relat Res* 467:666-675.

105. Siebenrock KA, Kalbermatten DF, Ganz R. 2003. Effect of pelvic tilt on acetabular retroversion: A study of pelvis from cadavers. *Clin Orthop Relat Res*:241-248.
106. Zaltz I, Kelly BT, Hetsroni I, Bedi A. 2012. The crossover sign overestimates acetabular retroversion. *Clin Orthop Relat Res*.
107. Sutter R, Dietrich TJ, Zingg PO, Pfirrmann CW. 2012. How useful is the alpha angle for discriminating between symptomatic patients with cam-type femoroacetabular impingement and asymptomatic volunteers? *Radiology* 264:514-521.
108. Nepple JJ, Martel JM, Kim YJ, et al. 2012. Do plain radiographs correlate with ct for imaging of cam-type femoroacetabular impingement? *Clin Orthop Relat Res* 470:3313-3320.
109. Anda S, Terjesen T, Kvistad KA, Svenningsen S. 1991. Acetabular angles and femoral anteversion in dysplastic hips in adults: Ct investigation. *J Comput Assist Tomogr* 15:115-120.
110. Anda S, Svenningsen S, Dale LG, Benum P. 1986. The acetabular sector angle of the adult hip determined by computed tomography. *Acta Radiol Diagn (Stockh)* 27:443-447.
111. Audenaert EA, Peeters I, Van Onsem S, Pattyn C. 2011. Can we predict the natural course of femoroacetabular impingement? *Acta Orthop Belg* 77:188-196.
112. Hartofilakidis G, Bardakos NV, Babis GC, Georgiades G. 2011. An examination of the association between different morphotypes of femoroacetabular impingement in asymptomatic subjects and the development of osteoarthritis of the hip. *J Bone Joint Surg Br* 93:580-586.
113. Laborie LB, Lehmann TG, Engesaeter IO, et al. 2011. Prevalence of radiographic findings thought to be associated with femoroacetabular impingement in a population-based cohort of 2081 healthy young adults. *Radiology* 260:494-502.
114. Audenaert EA, Baelde N, Huyse W, et al. 2011. Development of a three-dimensional detection method of cam deformities in femoroacetabular impingement. *Skeletal Radiol* 40:921-927.
115. Tannast M, Kubiak-Langer M, Langlotz F, et al. 2007. Noninvasive three-dimensional assessment of femoroacetabular impingement. *J Orthop Res* 25:122-131.

116. Bedi A, Dolan M, Hetsroni I, et al. 2011. Surgical treatment of femoroacetabular impingement improves hip kinematics: A computer-assisted model. *Am J Sports Med* 39 Suppl:43S-49S.
117. Kubiak-Langer M, Tannast M, Murphy SB, et al. 2007. Range of motion in anterior femoroacetabular impingement. *Clin Orthop Relat Res* 458:117-124.
118. Milone MT, Bedi A, Poultsides L, et al. 2013. Novel ct-based three-dimensional software improves the characterization of cam morphology. *Clin Orthop Relat Res*.
119. Audenaert EA, Mahieu P, Pattyn C. 2011. Three-dimensional assessment of cam engagement in femoroacetabular impingement. *Arthroscopy* 27:167-171.
120. Davies RH, Twining CJ, Cootes TF, et al. 2002. A minimum description length approach to statistical shape modeling. *IEEE Trans Med Imaging* 21:525-537.
121. Cates J, Fletcher PT, Styner M, et al. 2007. Shape modeling and analysis with entropy-based particle systems. *Inf Process Med Imaging* 20:333-345.
122. Fitzpatrick CK, Baldwin MA, Laz PJ, et al. 2011. Development of a statistical shape model of the patellofemoral joint for investigating relationships between shape and function. *J Biomech* 44:2446-2452.
123. Cootes TF, Taylor CJ. 2004. Anatomical statistical models and their role in feature extraction. *Br J Radiol* 77 Spec No 2:S133-139.
124. Bredbenner TL, Eliason TD, Potter RS, et al. 2010. Statistical shape modeling describes variation in tibia and femur surface geometry between control and incidence groups from the osteoarthritis initiative database. *J Biomech* 43:1780-1786.
125. Bryan R, Mohan PS, Hopkins A, et al. 2010. Statistical modelling of the whole human femur incorporating geometric and material properties. *Med Eng Phys* 32:57-65.
126. Zheng G, Dong X, Rajamani KT, et al. 2007. Accurate and robust reconstruction of a surface model of the proximal femur from sparse-point data and a dense-point distribution model for surgical navigation. *IEEE Trans Biomed Eng* 54:2109-2122.
127. Henak CR, Anderson AE, Weiss JA. 2013. Subject-specific analysis of joint contact mechanics: Application to the study of osteoarthritis and surgical planning. *J Biomech Eng* doi: 10.1115/1.4023386.

128. Pandy MG. 2001. Computer modeling and simulation of human movement. *Annu Rev Biomed Eng* 3:245-273.
129. Afoke NY, Byers PD, Hutton WC. 1987. Contact pressures in the human hip joint. *J Bone Joint Surg Br* 69:536-541.
130. von Eisenhart R, Adam C, Steinlechner M, et al. 1999. Quantitative determination of joint incongruity and pressure distribution during simulated gait and cartilage thickness in the human hip joint. *J Orthop Res* 17:532-539.
131. Brown TD, Shaw DT. 1983. In vitro contact stress distributions in the natural human hip. *J Biomech* 16:373-384.
132. Carlson CE, Mann RW, Harris WH. 1974. A radio telemetry device for monitoring cartilage surface pressures in the human hip. *IEEE Trans Biomed Eng* 21:257-264.
133. Hodge WA, Fijan RS, Carlson KL, et al. 1986. Contact pressures in the human hip joint measured in vivo. *Proc Natl Acad Sci U S A* 83:2879-2883.
134. Genda E, Iwasaki N, Li G, et al. 2001. Normal hip joint contact pressure distribution in single-leg standing--effect of gender and anatomic parameters. *J Biomech* 34:895-905.
135. Genda E, Konishi N, Hasegawa Y, Miura T. 1995. A computer simulation study of normal and abnormal hip joint contact pressure. *Arch Orthop Trauma Surg* 114:202-206.
136. Yoshida H, Faust A, Wilckens J, et al. 2006. Three-dimensional dynamic hip contact area and pressure distribution during activities of daily living. *J Biomech* 39:1996-2004.
137. Brown TD, DiGioia AM, 3rd. 1984. A contact-coupled finite element analysis of the natural adult hip. *J Biomech* 17:437-448.
138. Macirowski T, Tepic S, Mann RW. 1994. Cartilage stresses in the human hip joint. *J Biomech Eng* 116:10-18.
139. Rapperport DJ, Carter DR, Schurman DJ. 1985. Contact finite element stress analysis of the hip joint. *J Orthop Res* 3:435-446.
140. Mavcic B, Pompe B, Antolic V, et al. 2002. Mathematical estimation of stress distribution in normal and dysplastic human hips. *J Orthop Res* 20:1025-1030.

141. Anderson AE, Ellis BJ, Maas SA, Weiss JA. 2010. Effects of idealized joint geometry on finite element predictions of cartilage contact stresses in the hip. *J Biomech* 43:1351-1357.
142. Dalstra M, Huiskes R, van Erning L. 1995. Development and validation of a three-dimensional finite element model of the pelvic bone. *J Biomech Eng* 117:272-278.
143. Bachtar F, Chen X, Hisada T. 2006. Finite element contact analysis of the hip joint. *Med Biol Eng Comput* 44:643-651.
144. Lutz A, Fletz K, Nackenhorst U. 2009. Simulation of the physiological contact pressure distribution in the human hip joint. *Proc Appl Math Mech* 9:149-150.
145. Henninger HB, Reese SP, Anderson AE, Weiss JA. 2010. Validation of computational models in biomechanics. *Proc Inst Mech Eng H* 224:801-812.
146. Anderson AE, Ellis BJ, Maas SA, et al. 2008. Validation of finite element predictions of cartilage contact pressure in the human hip joint. *J Biomech Eng* 130:051008.
147. Anderson AE, Peters CL, Tuttle BD, Weiss JA. 2005. Subject-specific finite element model of the pelvis: Development, validation and sensitivity studies. *J Biomech Eng* 127:364-373.
148. Anderson AE, Ellis BJ, Peters CL, Weiss JA. 2008. Cartilage thickness: Factors influencing multidetector ct measurements in a phantom study. *Radiology* 246:133-141.
149. Allen BC, Peters CL, Brown NA, Anderson AE. 2010. Acetabular cartilage thickness: Accuracy of three-dimensional reconstructions from multidetector ct arthrograms in a cadaver study. *Radiology* 255:544-552.
150. Ateshian GA, Ellis BJ, Weiss JA. 2007. Equivalence between short-time biphasic and incompressible elastic material responses. *J Biomech Eng* 129:405-412.
151. Casartelli NC, Leunig M, Item-Glatthorn JF, et al. 2012. Hip flexor muscle fatigue in patients with symptomatic femoroacetabular impingement. *Int Orthop* 36:967-973.
152. Casartelli NC, Maffiuletti NA, Item-Glatthorn JF, et al. 2011. Hip muscle weakness in patients with symptomatic femoroacetabular impingement. *Osteoarthritis Cartilage* 19:816-821.

153. Rylander JH, Shu B, Andriacchi TP, Safran MR. 2011. Preoperative and postoperative sagittal plane hip kinematics in patients with femoroacetabular impingement during level walking. *Am J Sports Med* 39 Suppl:36S-42S.
154. Endo H, Mitani S, Senda M, et al. 2003. Three-dimensional gait analysis of adults with hip dysplasia after rotational acetabular osteotomy. *J Orthop Sci* 8:762-771.
155. Brisson N, Lamontagne M, Kennedy MJ, Beaulé PE. 2013. The effects of cam femoroacetabular impingement corrective surgery on lower-extremity gait biomechanics. *Gait Posture* 37:258-263.
156. Romano CL, Frigo C, Randelli G, Pedotti A. 1996. Analysis of the gait of adults who had residua of congenital dysplasia of the hip. *J Bone Joint Surg Am* 78:1468-1479.
157. Krekel PR, Vochteloo AJ, Bloem RM, Nelissen RG. 2011. Femoroacetabular impingement and its implications on range of motion: A case report. *J Med Case Rep* 5:143.
158. Kennedy MJ, Lamontagne M, Beaulé PE. 2009. Femoroacetabular impingement alters hip and pelvic biomechanics during gait walking biomechanics of fai. *Gait Posture* 30:41-44.
159. Bey MJ, Kline SK, Tashman S, Zauel R. 2008. Accuracy of biplane x-ray imaging combined with model-based tracking for measuring in-vivo patellofemoral joint motion. *J Orthop Surg Res* 3:38.
160. Seth A, Pandy MG. 2007. A neuromusculoskeletal tracking method for estimating individual muscle forces in human movement. *J Biomech* 40:356-366.
161. Fernandez JW, Pandy MG. 2006. Integrating modelling and experiments to assess dynamic musculoskeletal function in humans. *Exp Physiol* 91:371-382.
162. Besier TF, Gold GE, Beaupre GS, Delp SL. 2005. A modeling framework to estimate patellofemoral joint cartilage stress in vivo. *Med Sci Sports Exerc* 37:1924-1930.
163. Lund ME, de Zee M, Andersen MS, Rasmussen J. 2012. On validation of multibody musculoskeletal models. *Proc Inst Mech Eng H* 226:82-94.
164. Delp SL, Anderson FC, Arnold AS, et al. 2007. Opensim: Open-source software to create and analyze dynamic simulations of movement. *IEEE Trans Biomed Eng* 54:1940-1950.

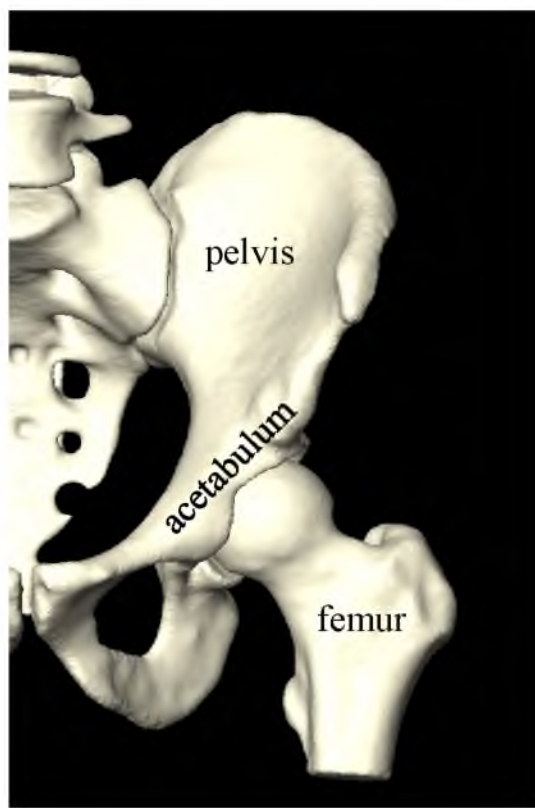


Figure 2.1. Bony anatomy of the hip. The proximal femur terminates in a ball like head that articulates within the acetabulum of the pelvis.

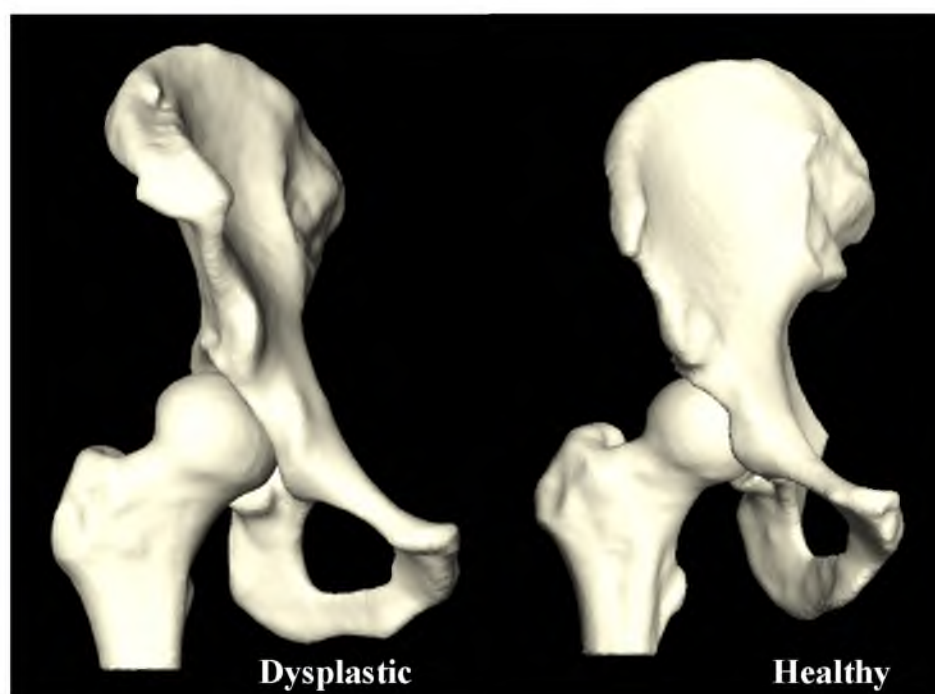


Figure 2.2 Bony reconstructions of dysplastic and healthy hips. The shallow acetabulum of the dysplastic patient causes reduced coverage of the femoral head.

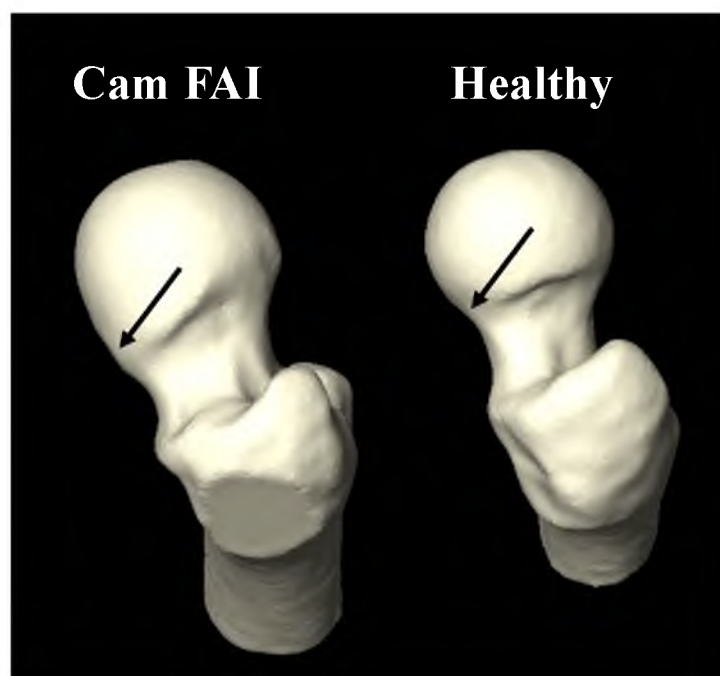


Figure 2.3. Femoral morphology in a cam FAI patient compared to a healthy control. In cam FAI patients, bony abnormalities in the anterior region of the head (arrow) reduce the ability of the femur to rotate within the acetabulum. Collisions between the femoral head and the acetabulum in cam FAI hips can damage articular cartilage and the acetabular labrum.

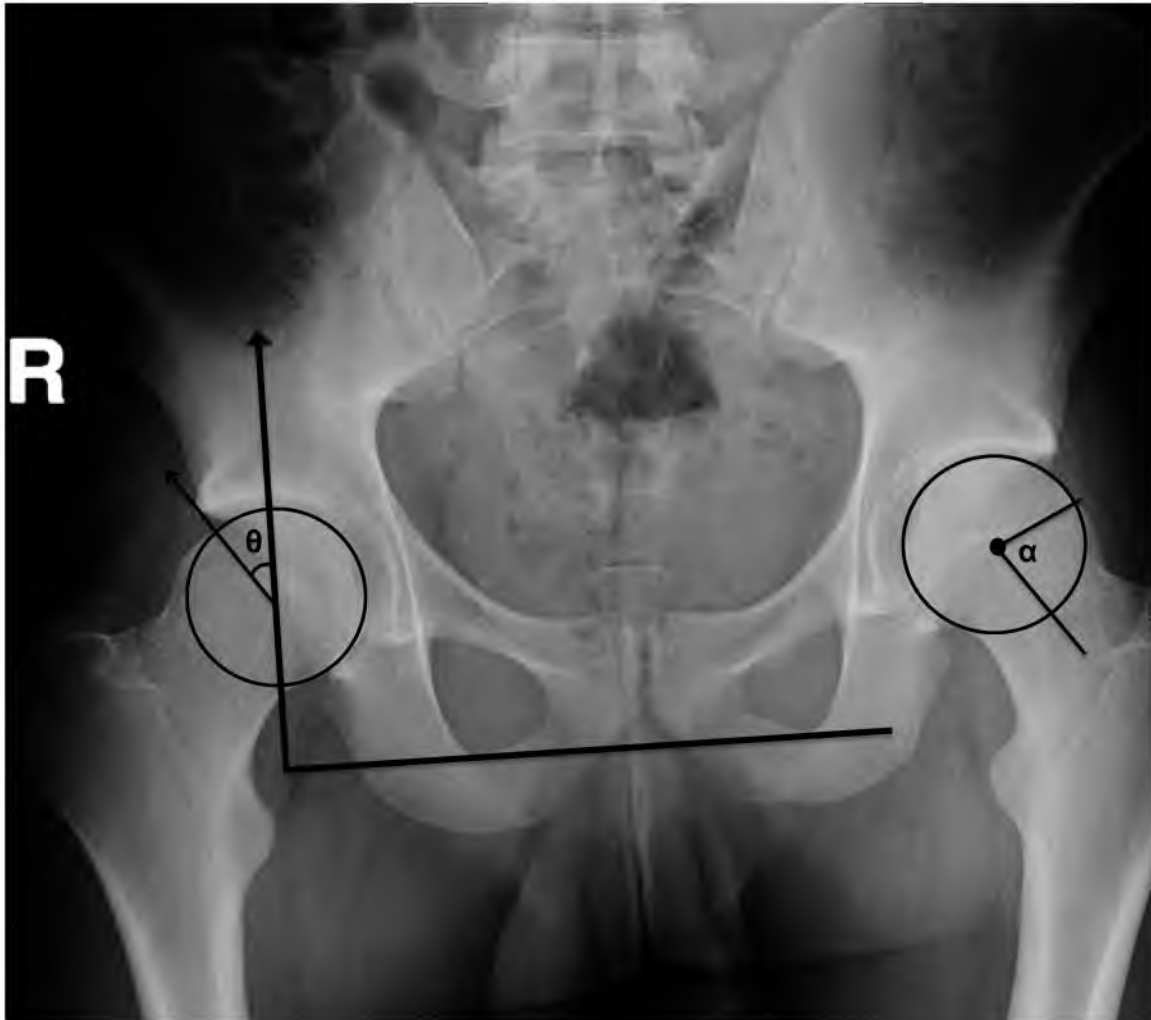


Figure 2.4. Two common radiographic measures of acetabular dysplasia and FAI. The lateral center edge angle (θ) is used for patients suspected to have dysplasia and measures the lateral coverage of the acetabulum over the femur. The alpha angle (α) is used to measure where a femur deviates from a circle fit to the femoral head and is used to diagnose cam FAI. Radiographic measures are useful for fast clinical screening but cannot fully describe the 3D deformities of dysplastic and FAI hips.

CHAPTER 3

THREE-DIMENSIONAL QUANTIFICATION OF FEMORAL HEAD SHAPE IN CONTROLS AND PATIENTS WITH CAM-TYPE FEMOROACETABULAR IMPINGEMENT¹

3.1 Abstract

An objective measurement technique to quantify 3D femoral head shape was developed and applied to normal subjects and patients with cam-type femoroacetabular impingement (FAI). 3D reconstructions were made from high-resolution CT images of 15 cam and 15 control femurs. Femoral heads were fit to ideal geometries consisting of rotational conchoids and spheres. Geometric similarity between native femoral heads and ideal shapes was quantified. The maximum distance native femoral heads protruded above ideal shapes and the protrusion area were measured. Conchoids provided a significantly better fit to native femoral head geometry than spheres for both groups. Cam-type FAI femurs had significantly greater maximum deviations (4.99 ± 0.39 mm and 4.08 ± 0.37 mm) than controls (2.41 ± 0.31 mm and 1.75 ± 0.30 mm) when fit to spheres or

¹Reprint of article “Three-dimensional quantification of femoral head shape in controls and patients with cam-type femoroacetabular impingement,” *Ann Biomed Eng.* Harris MD, Reese SP, Peters CL, Weiss JA, Anderson AE. 2013; DOI: 10.1007/s10439-013-0762-1 (in press). Reprinted with kind permission from Springer Science + Business Media B.V.

conchoids, respectively. The area of native femoral heads protruding above ideal shapes was significantly larger in controls when a lower threshold of 0.1 mm (for spheres) and 0.01 mm (for conchoids) was used to define a protrusion. The 3D measurement technique described herein could supplement measurements of radiographs in the diagnosis of cam-type FAI. Deviations up to 2.5 mm from ideal shapes can be expected in normal femurs while deviations of 4 to 5 mm are characteristic of cam-type FAI.

3.2 Introduction

Femoroacetabular impingement is a recently described disease of the hip that involves reduced clearance between the femoral head and acetabulum due to morphologic abnormalities of the femur (termed cam FAI), acetabulum (termed pincer FAI), or both (termed mixed FAI).¹ Cam-type FAI is marked by bony deformities of the femoral head epiphysis and/or reduction of head-neck offset.^{2,3} Cam deformities appear most often in the anterosuperior or anterolateral region of the femoral head and may cause shearing of hyaline cartilage, labral tears and early onset osteoarthritis (OA) in young adults.^{1,4,5}

Radiographs and physical examinations are the first tools to diagnose cam-type FAI.⁶⁻⁸ Physical examinations, involving passive flexion, adduction, and internal rotation of the hip, can often replicate pain and demonstrate loss of range of motion in patients with cam-type FAI, but cannot localize intra-articular bony abnormalities.⁸ Standard radiographic measurements, such as the alpha angle, provide an estimate of how femoral head shape in hips with suspected cam-type FAI deviates from a perfect circle.^{6,7,9} However, there is disagreement in the literature regarding the optimal radiographic

projection to view cam deformities.¹⁰⁻¹² In addition, the reliability of two-dimensional (2D) radiographic measurements has been debated.¹³⁻¹⁵

Computed tomography (CT) and magnetic resonance (MR) imaging improve the visualization of cam deformities as well as provide a qualitative assessment of the biological response of adjacent tissue.¹⁶⁻¹⁸ Unfortunately, published CT/MR based techniques for measuring cam-type FAI, such as radial MRI or acetabular sector angles, still yield only a 2D characterization of femoral head deformities, since measurements are made on a single image slice or limited series of slices.^{10,17,19,20} To this end, patient-specific 3D reconstructions of femoral head geometry, generated from segmentation of volumetric CT or MR images, have been described to quantify femoral head shape. Most often, 3D reconstructions are fit to spheres.²¹⁻²³ However, there is evidence that even healthy femurs are aspherical and that the articulating surfaces of the whole hip joint may be more accurately described by rotational ellipsoids or conchoids.²⁴⁻²⁶

Currently, there lacks methodology to objectively isolate the femoral head from the neck and identify the 3D location and size of cam-type deformities. Furthermore, quantitative descriptions of how 3D femoral head shapes deviate with respect to ideal shapes are not available. Finally, anatomical deviations from ideal shapes that can be expected in femoral heads with suspected cam-type FAI compared to normal femurs have not been reported. Thus, the purpose of this study was to develop an objective measurement technique to quantify and compare 3D femoral head shape between normal subjects and cam-type FAI patients.

3.3 Patients and Methods

3.3.1 Subject Selection

Institutional Review Board (IRB) approval (#10983) was obtained to prospectively acquire high-resolution multidetector CT scans of the pelvis and proximal femur in 15 patients (14 males, 1 female) with cam-type FAI. At the time of this study, all patients had hip and groin pain during activity, a positive impingement test, and radiographic evidence of cam-type FAI. In addition, all patients received or were scheduled for femoral osteochondroplasty and treatment of corresponding chondrolabral injury. Three patients were also treated for mixed FAI with correction to the acetabulum, but still had clear radiographic evidence of cam-type FAI.

CT scans were acquired using a Siemens SOMATOM 128 Definition CT Scanner (120 kVp tube voltage, 512 x 512 acquisition matrix, 1.0 mm slice thickness, 0.9 to 1.0 pitch). The baseline tube current was 250 mAs (CareDose used to minimize radiation exposure) and the estimated dose equivalent was 0.969 rem. The field of view covered the lateral border of both hips and varied between 300-400 mm across patients.

Control femurs were retrospectively selected from a collection of dissected and CT scanned cadavers (IRB #11755). Specimens had been screened to exclude those with signs of osteoarthritis and gross bony abnormalities. A cadaveric femur was chosen to match each patient by sex, age, weight, height, and body mass index (BMI). Femurs were aligned anatomically and imaged in a GE High Speed CTI Single Slice Helical CT scanner (100 kVp tube voltage, 512 x 512 acquisition matrix, 1.0 mm slice thickness, 1.0 pitch, 100 mAs tube current, 160 mm field of view).²⁷

Digitally reconstructed radiographs (DRR) were generated from the CT images to measure the alpha angle and head-neck offset of both patients and controls using the standing frog-leg lateral view of the femur.²⁸ First, CT image data of only the femur were isolated from the complete CT image stack using segmentation masks and a Boolean operation within Amira software (v5.3, Visage Imaging, San Diego, CA). The femur images were then rotated into the standing frog-leg position (femur flexed approximately 35° and externally rotated approximately 60°) and a DRR was generated to simulate plain film x-rays (Fig. 3.1). Alpha angle and head-neck offset were measured as described by Notzli et al. and Eijer et al., respectively, and adapted for the frog-leg lateral view by Clohisy et al.^{9,29,30} (Fig. 3.1).

3.3.2 3D Reconstruction

Bone surfaces were semiautomatically segmented from CT image data using Amira and validated threshold settings.^{31,32} To improve resolution of the segmentation mask, CT images were up-sampled to 1536×1536, 0.3 mm thickness for patients and 1024×1024, 0.5 mm for controls. A sensitivity study found that further up-sampling of either control or patient images did not appreciably alter the shape of resulting 3D reconstructions. Reconstructed surfaces were triangulated and segmentation artifacts were removed by slightly smoothing surfaces using tools available in Amira.

The femoral head-neck junction was delineated using a custom Matlab script (r2010a; MathWorks, Natick, MA). First, a contour map of principal curvatures was created for the entire femoral surface and points of inflection (curvature = 0) were connected circumferentially around the head to define the transition between the head and

neck (Fig 3.2a). Next, a flexible 3D cutting surface was fit to the inflection points (Fig. 3.2b). The femoral head was identified as the section of the femur proximal to the cutting surface (Fig. 3.2c).

3.3.3 Comparison to Ideal Geometries

Femoral head reconstructions were fit to two ideal geometries: spheres and rotational conchoids.³³ First, the sphere that best fit the nodal coordinates of the femoral head was determined. Next, a spherical surface was created by projecting nodes from the native femoral head onto the best-fit sphere. Likewise, a best-fit conchoid was determined and fit for each femoral head according to:

$$r = a + b \cos \theta , \quad (3.1)$$

where r is a curve with length measured from the geometric center of the conchoid, θ is the angle between r and the polar axis, and a and b are radii extending from the center (Fig. 3.3). The center of the conchoid was defined as the center of the best-fit sphere.

A custom C++ script measured the distance between nodes on the native femoral head and the best-fit geometries; the maximum distance was identified as “maximum deviation”, with units of mm. Fitting errors between the native femoral head and the best-fit geometry were calculated as the root-mean-squared distance between nodes on the native head and the best-fit geometry. Lower fitting errors indicated a better fit. The fovea of the femoral head was visually identified and excluded during sphere/conchoid fitting and calculation of maximum deviation.

3.3.4 Regionalization of the Femoral Head and Characterization of the Protrusion

Regional analysis was completed by dividing each femoral head into four regions: anterolateral (AL), anteromedial (AM), posterolateral (PL), and posteromedial (PM). First, a plane was created based on three points: (1) the geometric center of the head when fit to a sphere, (2) the center of the narrowest cross-section of the neck (i.e., the average Cartesian coordinates of the surface nodes at the narrowest section of the neck), and (3) the circumferential center of the femoral shaft at the superior aspect of the lesser trochanter (i.e., the average Cartesian coordinates of surface nodes at a cross section of the superior aspect of the lesser trochanter). The first plane was approximately equivalent to a coronal slice as it divided the anterior and posterior halves of the femoral head. Using direction cosine values from the first plane and the center of the best-fit sphere, a second plane was created perpendicular to the first to divide the medial and lateral halves of the head. These bisecting planes defined the four regions of the femoral head (Fig. 3.2d), which were used for all subsequent analyses at the regional level (i.e., same planes used for conchoid and sphere analysis).

The region containing the maximum deviation from ideal geometry was identified as the location of the protrusion. Protrusion area was measured as the deviation threshold (i.e., the lower bound defining a protrusion) was increased logarithmically from 0 mm to 1.0 mm, with an additional deviation threshold at 0.5 mm. Protrusion areas were reported as absolutes (mm^2) and as a percentage of total area of the region in which they were located.

3.3.5 Statistical Analysis

Variables of interest were assessed for normality using the Shapiro-Wilk test. A paired t-test detected statistically significant differences between normally distributed variables. A nonparametric Mann-Whitney U test was used for data that were not normally distributed. Significance was set at $p \leq 0.05$.

Alpha angles and head-neck offsets measured on the frog-leg lateral view were compared using paired t-tests. Fitting errors and maximum and mean deviations from a sphere and conchoid were compared between patients and controls. Fitting errors were also compared between sphere and conchoid fits within each subject group (e.g., sphere vs. conchoid for controls). Regionalized maximum and mean deviations from a sphere and conchoid were compared between patients and controls. Finally, differences in protrusion areas between controls and patients were tested at each deviation threshold for both spheres and conchoids. Data were reported as mean \pm standard error of the mean unless otherwise noted.

3.4 Results

The average and standard deviation of the age, weight, height and BMI of the patients and (controls) was 26 ± 7 (27 ± 8) years, 84 ± 10 (83 ± 10) kg, 181 ± 8 (182 ± 7) cm, and 25.3 ± 3.4 (24.9 ± 3.2) kg/m², respectively. Alpha angles for control subjects were $45.9 \pm 7.8^\circ$ and fell within a range previously reported for asymptomatic subjects.^{29,34} Alpha angles for patients ($68.5 \pm 13.5^\circ$) were significantly greater than those of controls ($p < 0.001$). The femoral head-neck offset in patients (4.9 ± 1.9 mm) was significantly less when compared to controls (7.1 ± 2.2 mm) ($p=0.01$).

Compared to a sphere, the rotational conchoid provided a better fit to both patients ($p = 0.001$) and controls ($p < 0.001$) (Fig. 3.4). In addition, control femurs fit the ideal geometry better than patient femurs for both the sphere ($p < 0.001$) and the conchoid ($p < 0.001$). Patients had greater maximum deviations from both the sphere and conchoid when compared to controls ($p \leq 0.001$). Maximum deviations, maximum deviation 95% confidence intervals (CI), and average fitting errors are shown in Table 3.1.

Maximum deviations from a sphere were less for control femurs than for patients in all regions. Differences were significant in the AL ($p < 0.001$), AM ($p = 0.023$), and PL ($p = 0.016$) regions. Mean deviations for the control femurs were less than for patients, but were only statistically significant in the PL region ($p = 0.011$) (Fig. 3.5).

Maximum deviations from a conchoid were significantly smaller for control femurs than for patients in all regions (Fig. 3.5). As with the sphere, mean deviations from a conchoid for the control femurs were less than for patients, but were only statistically significant in the PL region ($p = 0.045$) (Fig. 3.5).

The maximum deviation from ideal geometries occurred most often in the AL region. This trend was true for all patients when fit to both spheres and conchoids. For the control femurs fit to spheres, 14 of 15 showed a maximum deviation in the AL region, with 1 being in the PM region. For controls fit to conchoids, there were 4 femurs with maximum deviation in the PM region, with the remaining 11 being in the AL region.

When fit to spheres and with a 0 mm deviation threshold, protrusion areas were $827.1 \pm 42.2 \text{ mm}^2$ ($68.9 \pm 3.7\%$ of region) and $675.8 \pm 39.3 \text{ mm}^2$ ($53.0 \pm 3.1\%$) for controls and patients, respectively (Fig. 3.6). Using conchoids and a 0 mm deviation

threshold, protrusion areas for controls and patients were $685.8 \pm 56.3 \text{ mm}^2$ ($54.0 \pm 3.5\%$) and $518.4 \pm 41.3 \text{ mm}^2$ ($40.8 \pm 3.4\%$), respectively (Fig. 3.6).

Protrusion areas for the control group were significantly larger than that of the patients at lower deviation thresholds (Fig. 3.6). For the sphere, area differences between controls and patients were significant at deviation thresholds of 0 mm, 0.01 mm, and 0.1 mm (all $p \leq 0.016$). For the conchoid, area differences were significant at thresholds of 0 mm and 0.01 mm (both $p \leq 0.021$). At a deviation threshold of 1.0 mm for the sphere and 0.5 mm for the conchoid, the relationship between control and patient protrusion areas was inverted; above these thresholds the areas of patient protrusions were larger (Fig. 3.6).

3.5 Discussion

The purpose of this study was to develop an objective technique to isolate, quantify, and compare 3D femoral head shape between normal subjects and cam-type FAI patients. We determined that patients with cam-type FAI had femoral heads that deviated significantly more from ideal shapes than controls. While this result is to be expected, until now a quantified description of 3D deviations from ideal shapes in cam-type femurs relative to their normal counterparts has not been presented. In addition, to our knowledge, the characteristic features of bony protrusions beyond ideal geometries in normal subjects and patients with cam-type FAI had not been reported. Here, we found the counter-intuitive result that protrusion areas on the control femurs were significantly greater than protrusions on the cam-type FAI femurs. Nonetheless, protrusions on the cam-type FAI femurs were associated with significantly higher maximum deviations,

which may be a greater contributor to joint damage and pain than the broad, yet low-lying, protrusions found on the control femurs.

The femurs analyzed in this study deviated from both spheres and rotational conchoids but were more similar to conchoids. This relationship was true for both control and patient femurs as indicated by conchoid fitting errors that were significantly lower than those from sphere-fitting. The better fit to rotational conchoids supports the theoretical findings of another study.²⁴ Thus, when analyzing femoral head shape for surgical planning purposes, the conchoid is likely to give a more accurate indication of deviation from normal than a perfect sphere.

Maximum deviations were significantly smaller for control femurs than for patients. Still, maximum deviations for the control subjects averaged 2.41 mm (sphere-fit) and 1.75 mm (conchoid-fit), suggesting that some level of deviation from any ideal geometry can be expected among normal femurs. This amount of deviation is similar to the 2.8 mm of asphericity found in a prior study of subjects with no evidence of FAI.¹⁰ Patient femurs had maximum deviations that were roughly 2.5 times greater than control subjects. Control femurs were also a significantly better fit to both the sphere and the conchoid than were the patients. Hence, when comparing deviations from ideal shapes using either the sphere or the conchoid, measuring maximum deviation and fitting error facilitates a quantifiable distinction between normal and cam-type femurs that may be relevant when determining debridement surgery to treat cam-type FAI.

In this study, the largest deviations from ideal geometries were most often in the anterolateral region. This was an expected result for the patient femurs, as the anterolateral and anterosuperior sections of the femoral head have been identified as the

primary locations for cam lesions.^{2,35} Considering this region also contained the maximum deviation for most control subjects reinforces the conjecture that this area is sensitive to developmental deformities that could result in impingement. Outside the anterolateral region, controls had maximum and mean regional deviations that were generally less, yet not always significantly so, than patients. So, while deviations in the anterolateral region were the most prominent in our study, a cam-type FAI femur may have lesions or deformities throughout the surface of the femoral head.

An interesting phenomenon was observed with respect to the maximum deviation and protrusion area. Although patients had larger maximum deviations than controls, protrusion areas on control subjects were actually greater than that of patients. However, this trend was inverted when deviation thresholds defining a protrusion were raised above 0.5 mm and 1.0 mm for conchoids and spheres, respectively. These results suggest that broad, but smooth/flat, protrusions may be present in normal femurs. In subjects with cam-type FAI, protrusions were more localized with higher maximum deviations. The difference in the shape of the protrusion between control and patient femurs may support the suspected high-pressure, high-shear mechanism of damage that is thought to occur in cam-type FAI hips.¹

There were limitations to this study that should be considered when interpreting the findings. First, controls in this study did not have a documented patient history, which limited the clinical characterization of joint health to that of gross observation. Categorization as a control femur relied upon qualifications, including cartilage/subchondral appearance. However, alpha angle and head-neck offset values for the control subjects fell within acceptable ranges for normal femurs.^{29,34}

An additional limitation was that patients were included only if they had radiographic evidence of cam impingement and associated symptoms consistent with FAI. Asymptomatic subjects who may have radiographic cam signs were not included, possibly excluding a subsection of the FAI population. It has been previously shown that deviation from ideal geometry does not guarantee that a femur will become symptomatic or lead to OA.³⁶⁻³⁸ However, this exclusion provided clarity and distinction when quantifying anatomical differences between cam-type FAI patients and controls.

Another limitation was that the acetabulum and articular cartilage topology were not included in the analysis. While acetabular anatomy may contribute to impingement, this study intentionally focused on patients with deformities primarily on the femoral head. Certainly, when planning surgery to reduce impingement, acetabular orientation and shape should be considered. Articular cartilage may develop in such a way to form a congruent articulating surface between the femur and acetabulum, thereby compensating for minor asphericity of the bone. As such, cartilage topology should be considered, especially intraoperatively, when determining the severity of geometric deviations. However, altered bone geometry is the focus when diagnosing cam-type FAI from CT images and radiographs, not cartilage topology as it is often not available. Thus, for the current study, which serves as a 3D supplement to conventional diagnostic tools, only bony anatomy of the femur was considered. Another limitation is that, because CT image data were segmented semiautomatically, there may be some observer-dependence in the resulting segmentations. However, the accuracy of the segmentation and reconstruction protocols has already been evaluated and found to produce errors minor compared to the

degree in which protrusions statistically differed between subject groups in the current study.^{31,32}

A final limitation is that CT arthrography was used on the patients to obtain high-resolution CT images. This procedure is invasive with respect to ionizing radiation. The Food and Drug Administration (FDA) Guidelines for Research Subjects sets an estimated dose equivalent (EDE) limit of 3 rem for a single session and no more than 5 rem annually, equal to that stipulated for employees who utilize radiation as part of their employment. The EDE for our CT arthrogram procedure is 0.969 rem. Therefore, subjects obtained roughly 20% of the annual exposure stipulated by the FDA. In the future, noninvasive methods could be utilized to create 3D reconstructions, such as high-resolution MR imaging.

Surgical correction of cam-type FAI seeks to recontour the femoral head to improve range of motion and correct deleterious joint contact mechanics.³⁹⁻⁴² Under-correction has been reported to cause persistent pain while over-correction can weaken the femoral head and neck and disrupt vasculature.⁴³⁻⁴⁵ A-priori knowledge regarding the size and location of cam deformities, such as that provided in Figure 3.4, may assist surgeons when making pre- or intraoperative decisions. In fact, the methodology presented in this study could provide a basis to develop intraoperative hardware and software to determine, precisely, the location of cam-type deformities that require surgical correction.

While best-fit circles and 2D measures (e.g., alpha angle, head-neck offset) are the reference standard for diagnosing cam-type FAI, they provide a limited view of deformities that occur outside the radiographic projection plane. As such, we recommend

the use of 3D reconstructions of the femoral head and subsequent objective quantification of pathoanatomy to characterize the severity of cam-type FAI, especially for those patients having hip pain, but presenting with unimpressive radiographs.⁴⁶ The 3D methods proposed in this study can be used as a supplement to radiographic diagnostics by clinics that have the ability to make 3D femoral surface reconstructions from CT or MR images. The results of this study suggest that anatomical deviations of up to 2.5 mm from ideal geometries can be expected in normal femurs while deviations of 4 to 5 mm are characteristic of femoral heads that present symptomatic cam-type FAI.

3.6 Acknowledgements

Funding for the recruitment and CT scanning of cam-type FAI patients was received through NIH grant #R01AR053344. Procurement and CT scanning of the control femurs was done with funds from a U.S. Department of the Army Award #W81XWH-06-1-0574.

3.7 References

1. Ganz R, Parvizi J, Beck M, et al. 2003. Femoroacetabular impingement: A cause for osteoarthritis of the hip. Clin Orthop Relat Res:112-120.
2. Ito K, Minka MA, 2nd, Leunig M, et al. 2001. Femoroacetabular impingement and the cam-effect. A mri-based quantitative anatomical study of the femoral head-neck offset. J Bone Joint Surg Br 83:171-176.
3. Siebenrock KA, Wahab KH, Werlen S, et al. 2004. Abnormal extension of the femoral head epiphysis as a cause of cam impingement. Clin Orthop Relat Res:54-60.
4. Harris WH. 1986. Etiology of osteoarthritis of the hip. Clin Orthop Relat Res:20-33.

5. Meermans G, Konan S, Haddad FS, Witt JD. 2010. Prevalence of acetabular cartilage lesions and labral tears in femoroacetabular impingement. *Acta Orthop Belg* 76:181-188.
6. Clohisy JC, Carlisle JC, Beaulé PE, et al. 2008. A systematic approach to the plain radiographic evaluation of the young adult hip. *J Bone Joint Surg Am* 90 Suppl 4:47-66.
7. Tannast M, Siebenrock KA, Anderson SE. 2008. [femoroacetabular impingement: Radiographic diagnosis--what the radiologist should know]. *Radiologia* 50:271-284.
8. Philippon MJ, Maxwell RB, Johnston TL, et al. 2007. Clinical presentation of femoroacetabular impingement. *Knee Surg Sports Traumatol Arthrosc* 15:1041-1047.
9. Notzli HP, Wyss TF, Stoecklin CH, et al. 2002. The contour of the femoral head-neck junction as a predictor for the risk of anterior impingement. *J Bone Joint Surg Br* 84:556-560.
10. Dudda M, Albers C, Mamisch TC, et al. 2009. Do normal radiographs exclude asphericity of the femoral head-neck junction? *Clin Orthop Relat Res* 467:651-659.
11. Konan S, Rayan F, Haddad FS. 2010. Is the frog lateral plain radiograph a reliable predictor of the alpha angle in femoroacetabular impingement? *J Bone Joint Surg Br* 92:47-50.
12. Meyer DC, Beck M, Ellis T, et al. 2006. Comparison of six radiographic projections to assess femoral head/neck asphericity. *Clin Orthop Relat Res* 445:181-185.
13. Barton C, Salineros MJ, Rakhra KS, Beaulé PE. 2011. Validity of the alpha angle measurement on plain radiographs in the evaluation of cam-type femoroacetabular impingement. *Clin Orthop Relat Res* 469:464-469.
14. Carlisle JC, Zebala LP, Shia DS, et al. 2011. Reliability of various observers in determining common radiographic parameters of adult hip structural anatomy. *Iowa Orthop J* 31:52-58.
15. Clohisy JC, Carlisle JC, Trousdale R, et al. 2009. Radiographic evaluation of the hip has limited reliability. *Clin Orthop Relat Res* 467:666-675.
16. Beaulé PE, Zaragoza E, Motamedi K, et al. 2005. Three-dimensional computed tomography of the hip in the assessment of femoroacetabular impingement. *J Orthop Res* 23:1286-1292.

17. Domayer SE, Ziebarth K, Chan J, et al. 2010. Femoroacetabular cam-type impingement: Diagnostic sensitivity and specificity of radiographic views compared to radial mri. *Eur J Radiol*.
18. Pfirrmann CW, Mengiardi B, Dora C, et al. 2006. Cam and pincer femoroacetabular impingement: Characteristic mr arthrographic findings in 50 patients. *Radiology* 240:778-785.
19. Rakhra KS, Sheikh AM, Allen D, Beaulé PE. 2009. Comparison of mri alpha angle measurement planes in femoroacetabular impingement. *Clin Orthop Relat Res* 467:660-665.
20. Anda S, Terjesen T, Kvistad KA, Svenningsen S. 1991. Acetabular angles and femoral anteversion in dysplastic hips in adults: Ct investigation. *J Comput Assist Tomogr* 15:115-120.
21. Almoussa S, Barton C, Speirs AD, et al. 2011. Computer-assisted correction of cam-type femoroacetabular impingement: A sawbones study. *J Bone Joint Surg Am* 93 Suppl 2:70-75.
22. Audenaert EA, Baelde N, Huysse W, et al. 2011. Development of a three-dimensional detection method of cam deformities in femoroacetabular impingement. *Skeletal Radiol* 40:921-927.
23. Tannast M, Kubiak-Langer M, Langlotz F, et al. 2007. Noninvasive three-dimensional assessment of femoroacetabular impingement. *J Orthop Res* 25:122-131.
24. Menschik F. 1997. The hip joint as a conchoid shape. *J Biomech* 30:971-973.
25. Cerveri P, Manzotti A, Baroni G. 2012. Patient-specific acetabular shape modelling: Comparison among sphere, ellipsoid and conchoid parameterisations. *Comput Methods Biomech Biomed Engin*.
26. Rasquinha BJ, Sayani J, Rudan JF, et al. 2012. Articular surface remodeling of the hip after periacetabular osteotomy. *Int J Comput Assist Radiol Surg* 7:241-248.
27. Ruff CB, Hayes WC. 1988. Sex differences in age-related remodeling of the femur and tibia. *J Orthop Res* 6:886-896.
28. Metz CT. 2005. Digitally reconstructed radiographs. Utrecht University.
29. Clohisy JC, Nunley RM, Otto RJ, Schoenecker PL. 2007. The frog-leg lateral radiograph accurately visualized hip cam impingement abnormalities. *Clin Orthop Relat Res* 462:115-121.

30. Eijer H, Leunig M, Mahomed N, Ganz R. 2001. Cross table lateral radiographs for screening of anterior femoral head-neck offset in patients with femoroacetabular impingement. *Hip international : the journal of clinical and experimental research on hip pathology and therapy* 11:37-41.
31. Anderson AE, Ellis BJ, Peters CL, Weiss JA. 2008. Cartilage thickness: Factors influencing multidetector ct measurements in a phantom study. *Radiology* 246:133-141.
32. Anderson AE, Peters CL, Tuttle BD, Weiss JA. 2005. Subject-specific finite element model of the pelvis: Development, validation and sensitivity studies. *J Biomech Eng* 127:364-373.
33. Anderson AE, Ellis BJ, Maas SA, Weiss JA. 2010. Effects of idealized joint geometry on finite element predictions of cartilage contact stresses in the hip. *J Biomech* 43:1351-1357.
34. Pollard TC, Villar RN, Norton MR, et al. 2010. Femoroacetabular impingement and classification of the cam deformity: The reference interval in normal hips. *Acta Orthop* 81:134-141.
35. Tannast M, Goricki D, Beck M, et al. 2008. Hip damage occurs at the zone of femoroacetabular impingement. *Clin Orthop Relat Res* 466:273-280.
36. Nepple JJ, Carlisle JC, Nunley RM, Clohisy JC. 2011. Clinical and radiographic predictors of intra-articular hip disease in arthroscopy. *Am J Sports Med* 39:296-303.
37. Audenaert EA, Peeters I, Van Onsem S, Pattyn C. 2011. Can we predict the natural course of femoroacetabular impingement? *Acta Orthop Belg* 77:188-196.
38. Kapron AL, Anderson AE, Aoki SK, et al. 2011. Radiographic prevalence of femoroacetabular impingement in collegiate football players: Aaos exhibit selection. *J Bone Joint Surg Am* 93:e111(111-110).
39. Byrd JW, Jones KS. 2009. Arthroscopic femoroplasty in the management of cam-type femoroacetabular impingement. *Clin Orthop Relat Res* 467:739-746.
40. Clohisy JC, Zebala LP, Nepple JJ, Pashos G. 2010. Combined hip arthroscopy and limited open osteochondroplasty for anterior femoroacetabular impingement. *J Bone Joint Surg Am* 92:1697-1706.
41. Ganz R, Gill TJ, Gautier E, et al. 2001. Surgical dislocation of the adult hip a technique with full access to the femoral head and acetabulum without the risk of avascular necrosis. *J Bone Joint Surg Br* 83:1119-1124.

42. Lavigne M, Parvizi J, Beck M, et al. 2004. Anterior femoroacetabular impingement: Part i. Techniques of joint preserving surgery. *Clin Orthop Relat Res*:61-66.
43. Lavigne M, Kalhor M, Beck M, et al. 2005. Distribution of vascular foramina around the femoral head and neck junction: Relevance for conservative intracapsular procedures of the hip. *Orthop Clin North Am* 36:171-176, viii.
44. Mardones RM, Gonzalez C, Chen Q, et al. 2006. Surgical treatment of femoroacetabular impingement: Evaluation of the effect of the size of the resection. *Surgical technique. J Bone Joint Surg Am* 88 Suppl 1 Pt 1:84-91.
45. Philippon MJ, Schenker ML, Briggs KK, et al. 2007. Revision hip arthroscopy. *Am J Sports Med* 35:1918-1921.
46. Matsuda DK. 2011. The case for cam surveillance: The arthroscopic detection of cam femoroacetabular impingement missed on preoperative imaging and its significance. *Arthroscopy* 27:870-876.



Figure 3.1. Alpha angle and head-neck offset measured on DRRs of the standing frog-leg lateral view. Left - A circle was fit to the femoral head and a line was drawn across the narrow section of the femoral neck. Alpha angle (α) was measured between a line from the center of the femoral neck to the center of the head and a second line from the center of the head to the point where the femur deviated from the best-fit circle. Right - Head-neck offset was measured by drawing line 1 along the axis of the femoral neck, line 2 parallel to line 1 tangent to the anterolateral neck and line 3 parallel to line 1 tangent to the anterolateral femoral head. Offset was measured as distance (d) between lines 2 and 3.

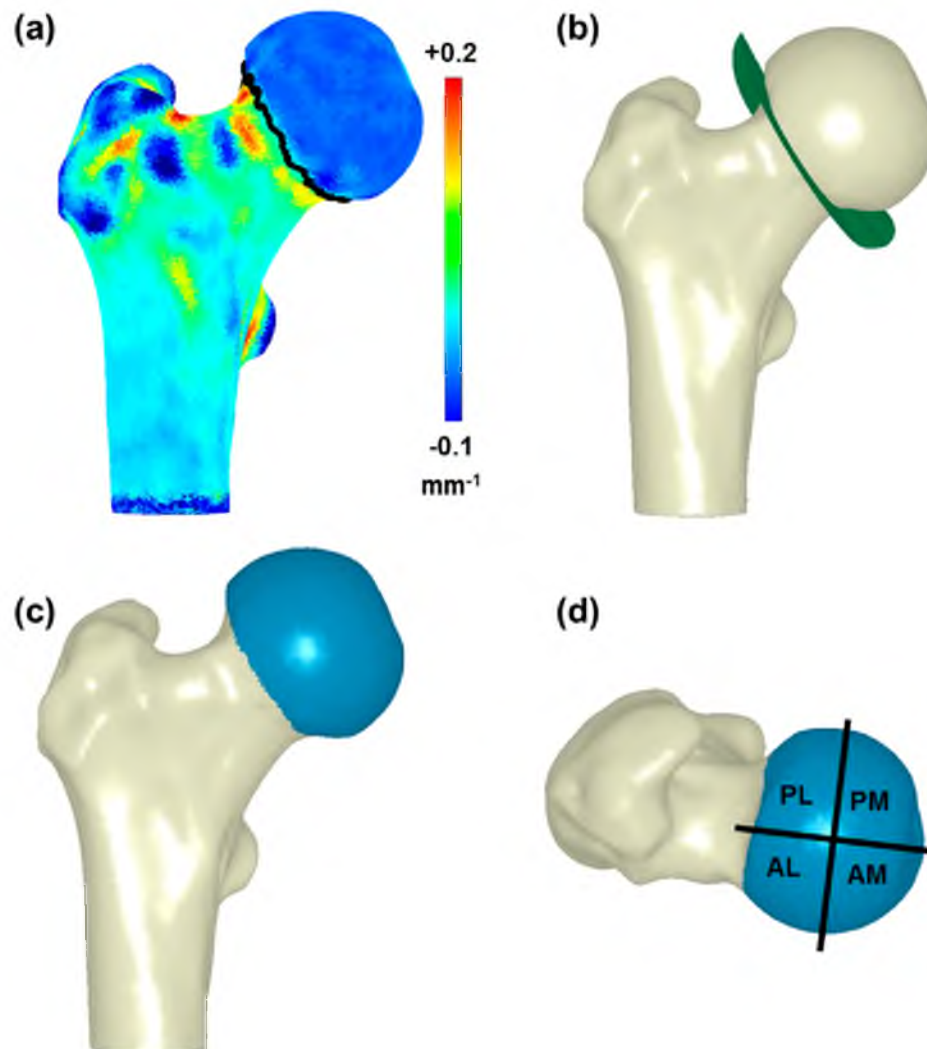


Figure 3.2. Three-dimensional reconstructions of the femur showing the process of identifying the head neck junction and regionalization of the femoral head. (a) First, a contour map of principal curvature was calculated for the entire proximal femur with inflection points identified by the dark line around the neck. (b) Next, a 3D cutting surface was fit to the inflection points. (c) The femoral head (blue) was identified as the section above the cutting surface. (d) Finally, the femoral head was regionalized into 4 regions.

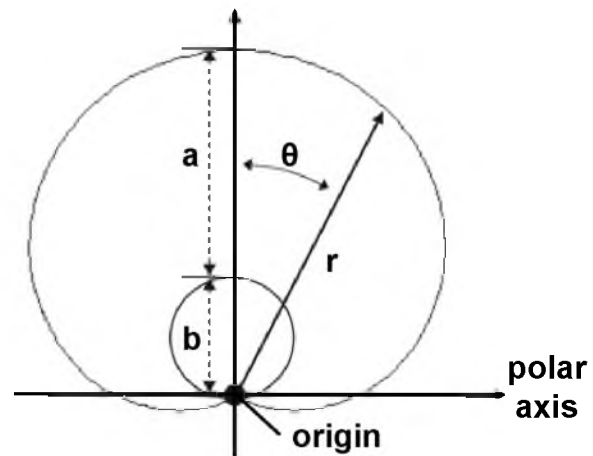


Figure 3.3. Geometric description of rotational conchoid according to equation $r=a+b*\cos(\theta)$. A conchoid was calculated for each femoral head by determining a and b radii values which resulted in a rotational vector, r , that best fit the native femur. Adapted from Anderson et al.³³

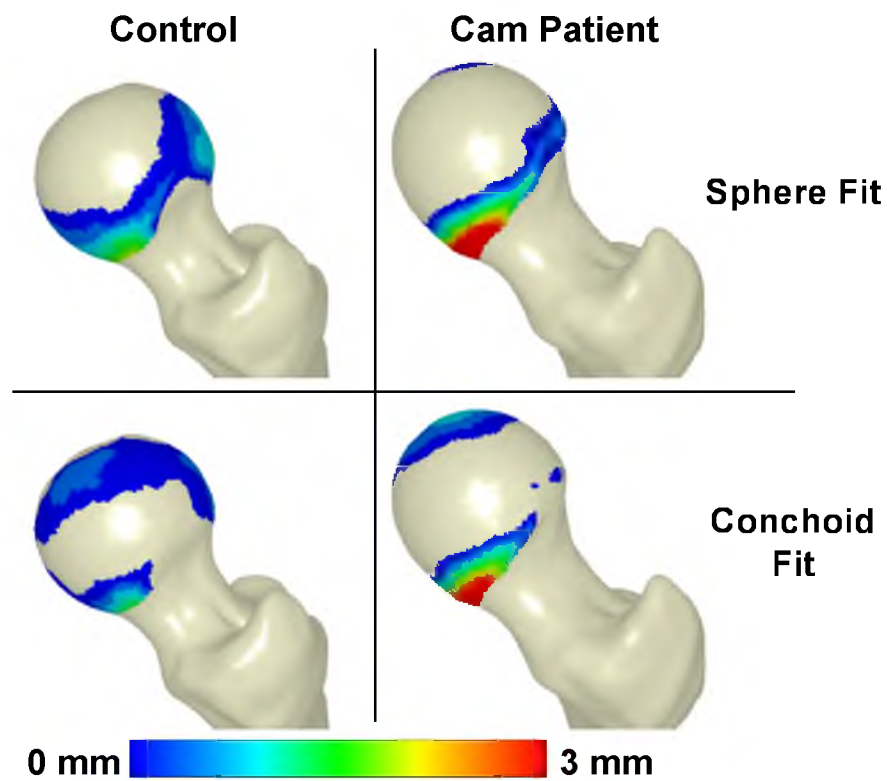


Figure 3.4. Deviations from ideal sphere and rotational conchoid shapes in representative control and patient femurs. Positive fringe plot values indicate areas where the native femur protruded above the ideal geometry.

Table 3.1. Mean \pm standard error maximum deviation values, 95% confidence intervals of maximum deviations, and mean \pm standard error fitting errors of control and patient femurs from best-fit spheres and conchoids.

	<u>Sphere Fit</u>			<u>Conchoid Fit</u>		
	Max. Deviation (mm)	Max. Deviation 95% CI (mm)	Fit Error (mm)	Max. Deviation (mm)	Max. Deviation 95% CI (mm)	Fit Error (mm)
Controls	2.41 \pm 0.31	1.81 – 3.01	0.739 \pm 0.158	1.75 \pm 0.30	1.16 – 2.33	0.296 \pm 0.230
Patients	4.99 \pm 0.39	4.22 – 5.75	0.949 \pm 0.138	4.08 \pm 0.37	3.36 – 7.80	0.660 \pm 0.242

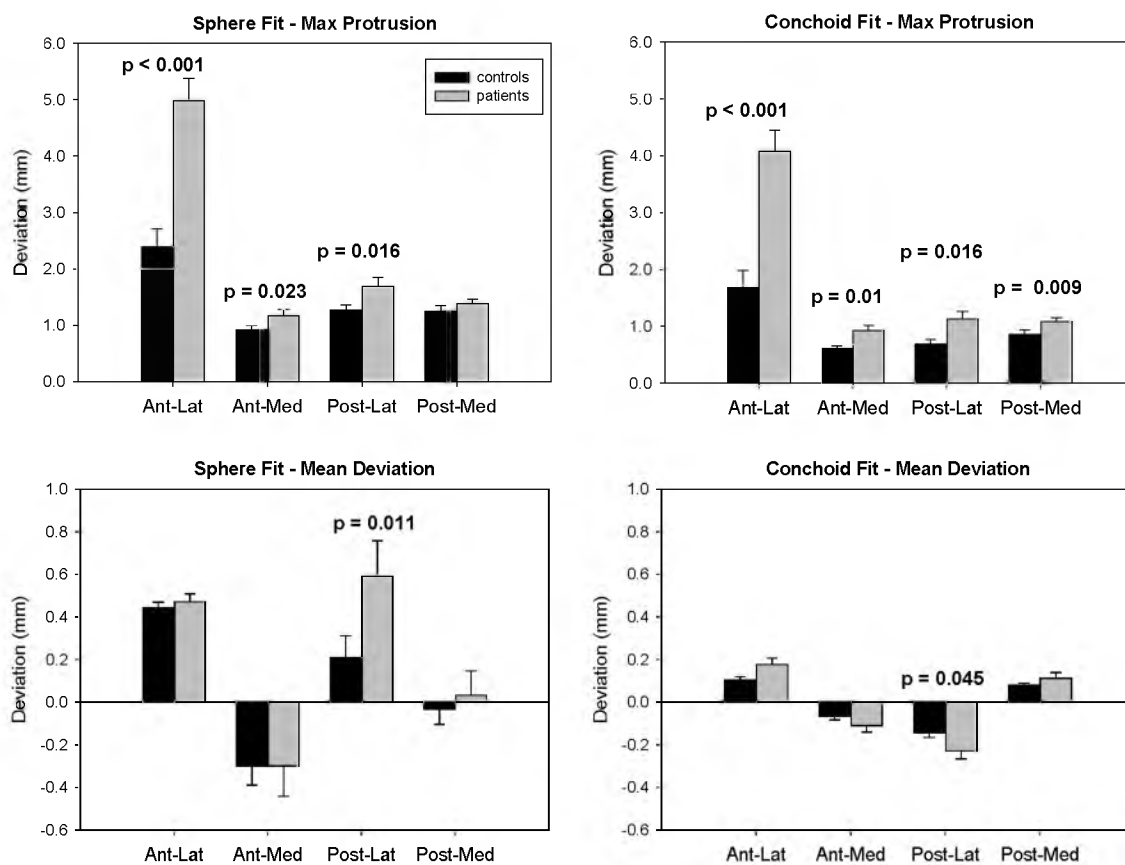


Figure 3.5. Maximum protrusion and mean deviation by region. Conchoids provided a better fit. Compared to patients, controls had significantly smaller maximum protrusions in almost every region. However, mean deviations between groups were only significant in the posterolateral region. Error bars indicate standard error. p-values indicate significant differences between groups.

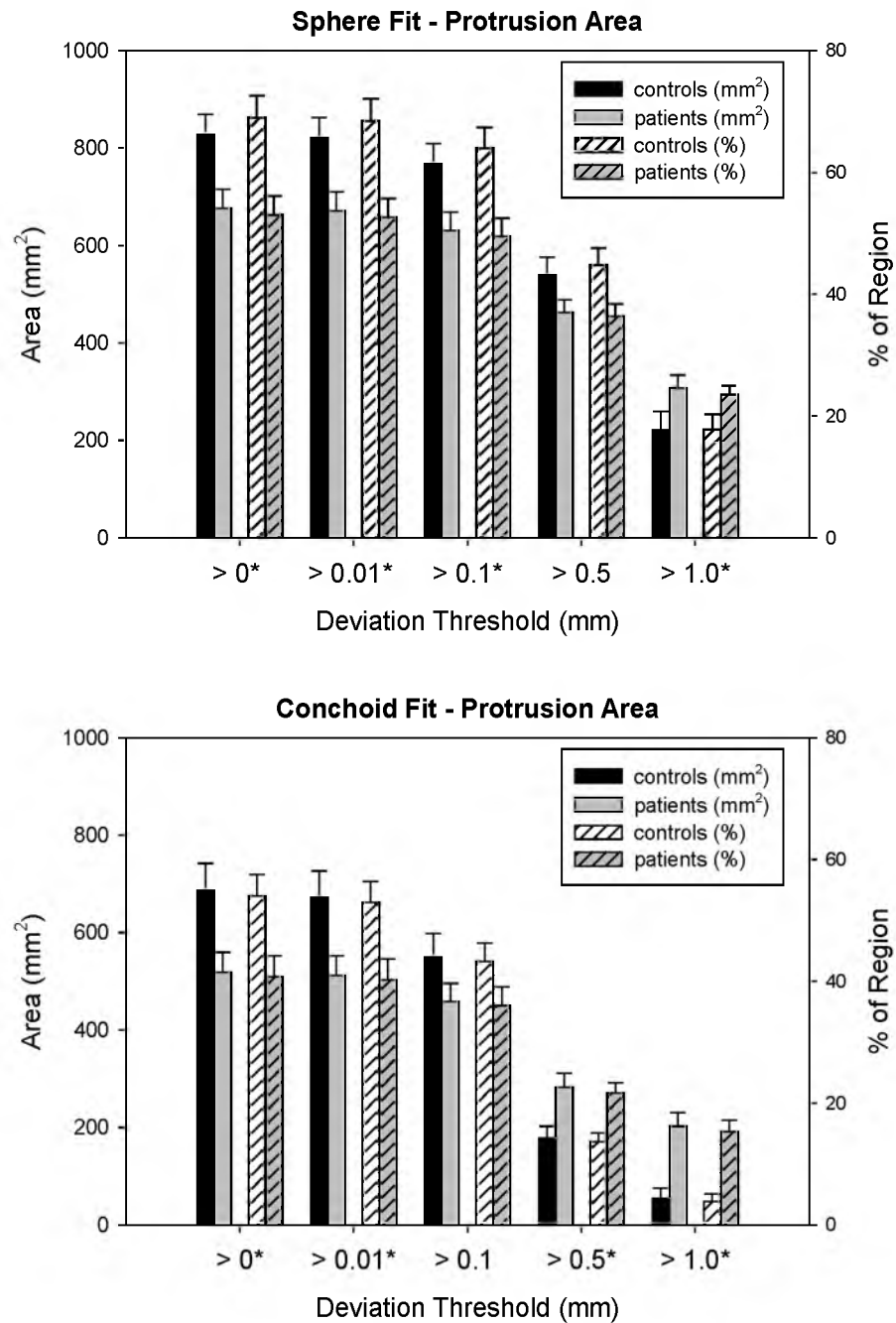


Figure 3.6. Protrusion areas determined in the region of maximum deviation from spheres (top) and conchoids (bottom). Error bars indicate standard error. At lower deviation thresholds, protrusions for the control group had larger areas than those of the patients. However, at higher thresholds protrusions for the patients outsized those of the controls. Asterisks indicate thresholds at which areas were significantly different between control and cam-type FAI femurs.

CHAPTER 4

CORRELATIONS BETWEEN THE ALPHA ANGLE AND FEMORAL HEAD ASPHERICITY: IMPLICATIONS AND RECOMMENDATIONS FOR DIAGNOSING CAM FEMOROACETABULAR IMPINGEMENT

4.1. Abstract

The purpose of this study was to determine the strength of common radiographic and radial CT views for measuring true femoral head asphericity. Alpha angles were measured by two observers using radial CT (0°, 30°, 60°, 90°) and digitally reconstructed radiographs (DRRs) (anterior-posterior (AP), standing frog-leg lateral, 45° Dunn with neutral rotation, 45° Dunn with 40° external rotation, cross-table lateral) generated from CT images of 15 patients with cam femoroacetabular impingement (FAI) and 15 controls. 3D femur reconstructions, with measurements of maximum deviation from a sphere, were utilized from a previous study. A DRR validation study was performed. Group-wise comparisons of alpha angles were assessed. Alpha angles were correlated with maximum deviation using Pearson's coefficient. DRRs were found to be a validated means to simulate standard radiographs of the hip. Alpha angles were significantly greater in patients for all views ($p \leq 0.002$). Alpha angles from the 45° Dunn with 40°

external rotation, cross-table lateral, and 60° radial views had the strongest correlations with maximum deviation ($r = 0.831$; $r = 0.823$; $r = 0.808$, respectively). The AP view had the weakest correlation ($r = 0.358$). The 45° Dunn with 40° external rotation, cross-table lateral, and 60° radial views best visualized femoral head asphericity. Although commonly used to screen for hip abnormalities, the AP view may fail to visualize cam FAI. Practitioners should standardize radiographic exams to avoid positioning artifact. The alpha angle was not a sure indicator of deformity size. Thus, asphericity measurements from 3D reconstructions may improve the diagnosis of cam FAI.

4.2 Introduction

Cam-type femoroacetabular impingement (FAI) has been implicated as a cause of chondrolabral damage and hip osteoarthritis (OA) in young adults.¹⁻³ Cam FAI is characterized by an aspherical femoral head and/or insufficient femoral head-neck offset.^{4,5} The alpha angle is a two-dimensional (2D) radiographic measure of femoral head asphericity that is commonly used to diagnose cam FAI.⁶⁻⁸ Although, first proposed by Notzli et al. for only an oblique axial view of the femur, use of the alpha angle has been extended to several radiographic projections and radial computed tomography (CT) or magnetic resonance (MR) views.^{7,9-13}

Identifying the size and location of the cam deformity is important since the goal of surgery is to remove offending bone. Unfortunately, alpha angle measurements are known to vary between views.^{10,14,15} Consequently, the ideal view to diagnose cam FAI remains unknown.^{14,16} One approach to evaluate the effectiveness of the alpha angle for a given view has been to quantify observer repeatability^{17,18}, but repeatability is not the

only measure of effectiveness. Another has been to correlate alpha angles from standard radiographic views to oblique axial or radial MRI views.^{12,14,16} However, alpha angle measurements from radial views are subjective, and thus do not provide a true reference standard. Finally, radial views do not consider the geometry of the entire femoral head.

Alpha angles from radiographs and radial views will continue to serve as an important means to diagnose cam FAI. However, there remains a need to identify the strength of common projections for quantifying true femoral head asphericity. Subject-specific 3D reconstructions of femur morphology, generated from volumetric CT or MR images, visualize the entire femur. By fitting the reconstruction to a sphere, one can quantify asphericity and size of a deformity as maximum deviation from a sphere.^{19,20}

The objective of this study was to determine the strength of common radiographic and radial CT views for measuring true femoral head asphericity. Specifically, we correlated alpha angle measurements of digitally reconstructed radiographs (DRRs) simulating 5 radiographic views and 4 radial CT views commonly obtained in the clinic with objective, 3D model-based measurements of asphericity in normal hips and hips with cam FAI, as measured in a previous study.

4.3 Patients and Methods

4.3.1 Subject Selection

Images of the pelvis and proximal femur were retrospectively acquired from 15 patients with cam FAI who had received a CT arthrogram as part of a previous study (IRB # 10983, 56086).²⁰ All patients had presented with hip and groin pain, had radiographic evidence of cam FAI and tested positive for impingement during clinical

examination. Patients received or were scheduled for femoral osteochondroplasty and treatment of chondrolabral injury. Three patients were treated for mixed FAI. A set of 15 control femurs were selected from a collection of cadavers to match the age, weight, height, and body mass index (BMI) of the cam FAI patients (IRB #56086).²⁰ Cadaver femurs did not have OA or bony deformities, as confirmed by visual inspection.

CT images of the patients had been acquired using a Siemens SOMATOM 128 Definition CT Scanner (120 kVp tube voltage, 512 x 512 acquisition matrix, 1.0 mm slice thickness, 0.9 to 1.0 pitch, 250 mAs baseline tube current with automated dose modulation using CareDose™, 300-400 mm field of view) in a previous study.²⁰ Each cadaveric control femur from the previous study²⁰ was aligned in neutral²¹ and imaged with a GE High Speed CTI Single Slice Helical CT Scanner (100 kVp tube voltage, 512 x 512 acquisition matrix, 1.0 mm slice thickness, 1.0 pitch, 100 mAs tube current, 160 mm field of view).

4.3.2 3D Reconstruction and Sphere Fitting

In the previous study,²⁰ femurs were semiautomatically segmented from the CT image data using Amira (v 5.4, Visage Imaging, San Diego, CA).²² To improve resolution of the segmentation mask, and decrease segmentation artifact, CT images had been up-sampled²³ to 1536×1536, 0.3 mm thickness for patients and 1024×1024, 0.5 mm for controls.

The femoral head of each femur had been fit to a sphere.²⁰ First, a contour map of principal curvatures was created for the entire femur. Next, a cutting surface was fit to points of inflection (curvature = 0) to define the head-neck boundary. Finally, the

femoral head was identified as the section of the femur proximal to the cutting surface (Fig. 4.1). PreView²⁴ had been used to determine the radius and center of the sphere which best fit the isolated head, via linear least-squares-minimization. Next, a spherical surface had been generated in PreView by projecting nodes from the native femoral head onto the best-fit sphere (Fig. 4.1). Asphericity was calculated as the maximum deviation (i.e., distance) between nodes on the native head and the best-fit sphere surface (Fig. 4.1).²⁰

4.3.3 Generation and Alignment of Digitally Reconstructed Radiographs

Digitally reconstructed radiographs (DRR) were used in the present study to simulate 5 common radiographic views used to diagnosis cam FAI. DRRs are generated from CT data using ray casting to produce an image similar to a clinical radiograph.²⁵ DRRs were utilized since they could be generated from controlled perspectives and avoid any bias in alpha angles due to positioning. A separate validation study demonstrated that alpha angles measured on DRRs were nearly identical to those from traditional radiographs (see Appendix).

DRRs were generated in Amira to simulate the: anterior-posterior (AP), standing frog-leg lateral, Dunn view with 45° flexion and neutral rotation, Dunn view with 45° flexion and 40° external rotation, and the cross-table lateral view. First, a DRR was generated from the complete CT image dataset (Fig. 4.2 a-b).²⁵ Then, the segmentation mask used to generate the femur reconstruction was combined with the DRR in a Boolean operation to isolate image data of the femur only (Fig. 4.2 c-d).

DRR images simulating each of the five projection views were created as follows (example for the standing frog-leg lateral in Fig. 4.3). First, traditional radiographs from the five projection views were obtained for a single, living control volunteer. This volunteer had CT image data acquired as part of a previous study (IRB # 10983). CT data for this subject were then used to generate a DRR of the femur, which was aligned in neutral orientation.²¹ From neutral, the DRR was rotated to match orientations of the traditional radiographs for the five views (see immediately below for information on positioning). The transformation was applied to DRRs of all subjects; this alignment routine was repeated for each projection.

Positioning of the single volunteer subject was as follows. For AP, the femur was in neutral flexion and abduction with 15° internal rotation. For the standing frog-leg, the femur was flexed approximately 35° and externally rotated approximately 60° with the foot resting on a 10 cm step. In the first Dunn view, the femur was flexed 45°, abducted 20° and maintained in neutral rotation.¹⁰ In the second Dunn view, the femur was flexed 45°, abducted 20°, and then rotated 40° externally. Applying external rotation for the second Dunn view is not a new view, rather it was found to yield radiographs that closely resembled several reported in the literature as 45° Dunn views.^{6,14} For the cross-table lateral view, the femur was in neutral flexion with 15° internal rotation and the beam parallel to the table and oriented 45° to the femoral head.²⁶

4.3.4 Generation and Alignment of Radial CT and Oblique Axial Views

Four radial CT views were generated in the present study, which covered the superior to anterior region quadrant of the femoral head. First, a plane was fit to points at

the center of the femoral head (when fit to a sphere), the center of the femoral neck, and the center of the femoral shaft.²⁷ The slice through the CT data at this plane was designated as 0° radial CT (Fig. 4.4). Using a line through the center of the femoral head and center of the neck as the axis of rotation, planes were created at 30° increments in an anterior progression (Fig. 4.4), resulting in 0°, 30°, and 60° radial CT views. A final plane was created at 90° of rotation about the head-to-neck axis, generating the oblique axial view described by Notzli et al.⁷

4.3.5 Measurement of the Alpha Angle

The alpha angle was semiautomatically measured on the DRRs and radial CT images using a custom Matlab script (Fig. 4.5).⁷ First, a circle was fit to the contour of the femoral head. Next, a line traversing the narrowest section of the neck was drawn. The alpha angle was measured as the angle between: 1) the line from the automatically calculated midpoint of the narrowest section of the neck to the center of the circle around the femoral head and 2) the line from the automatically calculated center of the circle to the point where the native femur began to deviate from the circle. Two observers independently measured the alpha angle on all views for all subjects. One observer repeated all measurements on two separate occasions.

4.3.6 Statistical Analysis

Statistical analysis was performed using SPSS (v16; IBM Corp., Armonk NY). Significance was set at $p \leq 0.05$. Maximum deviations between groups had been compared previously using the Student's t-test.²⁰ Interobserver and intraobserver

repeatability of alpha angle measurements was quantified using the intraclass correlation coefficient (ICC), with 95% confidence intervals. Interobserver repeatability was assessed between the first reads of both observers. Agreement was interpreted as: slight if the ICC < 0.20, fair if 0.21–0.40, moderate if 0.41–0.60, substantial if 0.61–0.80, and almost perfect if > 0.80.²⁸

For subsequent analysis, alpha angle measurements were averaged to include reads 1 and 2 from Observer A and read 1 from Observer B. Differences in alpha angles between the control and cam FAI subjects in each view were tested for statistical significance using Student's t-test. Next, data from patient and control groups were combined and linear correlation quantified the relationship between the alpha angle and maximum deviation. Specifically, the average alpha angles measured in each view were correlated to maximum deviation from a sphere using the Pearson correlation coefficient and linear regression. Posthoc power analysis was performed on the correlations to determine the correlation coefficient that could be detected with 80% power using a two-sided comparison with alpha = 0.05.

4.4 Results

Intraobserver ICC values for the alpha angle were almost perfect for all views, with a range of 0.868 to 0.981 (Table 4.1). Interobserver values were considered substantial to almost perfect, ranging from 0.722 to 0.978 (Table 4.1). Alpha angles for the cam FAI patients were significantly larger than those of control subjects in all views (all $p \leq 0.002$) (Table 4.1).

As previously reported, the average and standard deviation age, weight, height and BMI of the patients and (matched controls) was 26 ± 7 (27 ± 8) years, 84 ± 10 (83 ± 10) kg, 181 ± 8 (182 ± 7) cm, and 25.3 ± 3.4 (24.9 ± 3.2) kg/m², respectively.²⁰

As previously reported, the asphericity of cam FAI patient femurs, as indicated by maximum deviation from best-fit spheres, was 4.99 ± 0.39 mm and was significantly greater than that of the controls at 2.41 ± 0.31 mm ($p < 0.001$).²⁰ Maximum deviations occurred in the anterolateral region of the femoral head for all patients and 14 of 15 control femurs; 1 control femur had a maximum deviation located in the posteromedial region.²⁰

The strongest correlation between alpha angles and maximum deviations was found in the 45° Dunn view with 40° external rotation ($r = 0.831$). The remaining correlations, in order of decreasing strength, are shown in Figure 4.6. All correlations were significant ($p < 0.002$) except for the AP view ($p = 0.052$). From a two-sided post hoc power analysis, correlations with $r \geq 0.47$ were detectable with 80% power. Thus, 80% power was achieved for all correlations except the AP view.

4.5 Discussion

The purpose of this study was to determine the strength of common radiographic and radial CT views for measuring true femoral head asphericity. Maximum deviations from a sphere, quantified in a previous study, were used as the reference standard²⁰. Alpha angles measured from the 45° Dunn with 40° external rotation, cross-table lateral and 60° radial CT views were strongly correlated with maximum deviation.

The strength of the correlations for the 45° Dunn with 40° external rotation, cross-table lateral and 60° radial CT views corroborates previous reports.^{10,14,29} These “lateral views” captured maximum deviation well since they image the anterolateral/anterosuperior region; maximum deviations were most often noted in the anterolateral region in our study. Because intra- and inter-repeatability of alpha angle measurements was very good, we are confident that correlations for lateral views are the result of actual correspondence.

Given our results, we recommend that the 45° Dunn with 40° external rotation and cross-table lateral views be obtained for assessing cam FAI. The 60° radial CT may provide additional diagnostic value. We advocate against the use of the AP view as the primary means to diagnose cam FAI, although it may be useful to grade OA and assess pelvic alignment. However, correlations cannot ensure the lateral views alone are able to confirm/refute cam FAI as deformities vary. Thus, if the lateral views fail to visualize a cam deformity in a hip with symptoms consistent with FAI, we recommend clinicians obtain other views or CT/MRI.

Larger alpha angles are generally thought to be associated with more extensive damage.^{30,31} An unexpected finding of this study was that the view from which the highest alpha angles were measured did not have the strongest correlation to maximum deviation. The highest alpha angles were measured in the 45° Dunn view with neutral rotation but these angles were the third worst correlated to maximum deviation. Our study suggests that a large alpha angle in one view may not be a sure indicator of maximum deviation, and therefore, severity of the deformity. Thus, the threshold of the alpha angle to indicate a diagnosis of cam FAI may have to be adjusted between views.

Overall, obtaining views that are strongly correlated to maximum deviation is likely a better approach than ordering views that yield a high alpha angle.

Our results indirectly suggest that the manner in which a patient is positioned during a radiograph may influence measurements of the alpha angle and hence, estimates of maximum deviation. For example, the literature most often describes positioning for the 45° Dunn view as 45° flexion, 20° abduction and neutral rotation (Fig. 4.5).⁶ Maintaining neutral rotation in the 45° Dunn view resulted in a radiographic view that was relatively weak in correlation to maximum deviation. However, allowing approximately 40° of external rotation produced a view of the femur that matched images commonly identified as the regular 45° Dunn view in the literature (e.g., compare ^{6,14} to ¹⁰) and resulted in the strongest correlation. Hence, we recommend that clinicians and radiology technicians standardize patient positioning since this likely influences the appearance of the femoral head and associated measurements.

In addition to patient position during the radiograph, the manner in which a bump (i.e., deformity) presents may have important implications on the alpha angle. Anecdotally, we have noted that some femurs with cam FAI become aspheric more proximally, but do not have a sharply rising (i.e., prominent) bump; this would lead to a high alpha angle with relatively low maximum deviation. In contrast, we have observed femurs that become aspheric more distally, but have a prominent bump; this would lead to a lower alpha angle but a higher maximum deviation. Overall, 3D reconstructions and measurements of asphericity could delineate the manner in which a bump presents on a patient-specific basis.

Radial MRI is an increasingly popular tool to diagnose cam FAI.¹⁴⁻¹⁶ However, limiting the analysis of femoral head shape to a single radial view could be misleading. For example, in the current study, alpha angles from the 60° radial images were strongly correlated with maximum deviation, but angles from 30° radial images were weakly correlated. If volumetric imaging is to be used, we recommend the use of multiple radial views. Also, many clinical CT/MR scanners can automatically generate 3D reconstructions. Such reconstructions could provide improved, albeit qualitative, visualization of cam deformities.

A few limitations to the present study warrant discussion. First, for correlation with alpha angles, a single feature, maximum deviation, was chosen. Maximum deviation may not fully describe a cam deformity, including its area and morphology. However, maximum deviation provided an objective indication of the location and severity of a cam lesion and was straightforward to interpret. There may be additional variables that can be extracted in future studies, such as volume of the bump.

A second possible limitation is that patient positioning for each radiographic view can vary in the clinic, as opposed to the universal orientation of the DRRs obtained in the current study. However, by using DRRs, we avoided errors due to positional variability. Further, the validation study demonstrated that alpha angles measured on DRRs were nearly identical to those measured on traditional radiographs (see Appendix). Nevertheless, correlations presented herein should be considered the best-case results given the controlled methodology employed.

Another limitation was that detailed histories were not available for the cadaveric control group. However, angles for the current control subjects did fall within ranges

reported for asymptomatic, normal subjects.^{32,33} Furthermore, our study did not focus upon establishment of normal and abnormal alpha angle values, only correlation between 2D and 3D measurements of asphericity. More subjects could be included in the future for the purpose of defining normal/abnormal.

In conclusion, correlations between alpha angle and asphericity were strongest in the 45° Dunn with external rotation, cross-table lateral, and 60° radial views. The alpha angle was not a sure indicator of deformity size. Thus, asphericity measurements from 3D reconstructions may improve the diagnosis of cam FAI.

4.6 Appendix

4.6.1 DRR Validation: Methods

A separate study was conducted to demonstrate the validity of using DRRs in-lieu of traditional radiographs. First, seven 2 mm diameter steel beads were implanted into the femur of a cadaveric pelvis to toe-tips specimen. The specimen was radiographed using 7 projection views, including the 5 views described above (an additional iteration of the 45° Dunn view and the frog-leg lateral in a supine position were also captured). CT images of the cadaver were then collected and segmented as described above. A copy of the CT image set was created with the metallic beads intentionally obscured by converting pixels representing metal to those of the surrounding bone. Using the images in which beads had been obscured and 3D reconstructions of the femur, DRRs were generated and oriented to match each of the 7 projection views captured with traditional x-ray. Thus, orientation of the DRRs to match traditional radiographs was blinded to bead location and, instead, relied only upon bony landmarks and prescribed rotations.

The transformation applied to orient the bead-obsured CT images was then copied and applied to the original CT images that had visible beads. The result was a radiograph from each view and corresponding DRR with and without beads (Fig. 4.7).

The difference in orientation between the DRRs and corresponding traditional radiographs was quantified by measuring the distance between beads visible in both the DRR and radiograph. For each view, 10 interbead distances were measured on the traditional radiographs as the reference standard. Distances were then measured between the same beads on the DRR. Distances measured on the traditional radiographs and DRRs were tested for significant differences using paired Student's t-tests and for agreement with Bland-Altman plots.

The appropriateness of using DRRs as surrogates for radiographs in this study was further ascertained by measuring alpha angles on the radiograph/DRR pairs. This included 7 pairs from the cadaver, 5 pairs from the template volunteer, and 15 pairs from clinically acquired AP radiographs of FAI patients included in this study and their AP DRRs, totaling 27 pairs for statistical comparison. Differences and agreement between x-ray and DRR alpha angles were tested using a paired Student's t-test and Bland-Altman plots, respectively. Correspondence between alpha angles on the DRR versus those on the traditional radiograph was also assessed by correlation and linear regression.

4.6.2 DRR Validation: Results

No significant differences were found between interbead distances measured on cadaver radiographs compared to DRRs for any view ($p \geq 0.064$). The average \pm standard deviation difference of all measured interbead distances between the radiographs and

DRRs was -0.22 ± 0.77 mm with a 95% confidence interval (CI) of -0.04 to -0.40 mm and limits of agreement -1.76 mm and 1.33 mm. There were no significant differences between alpha angles measured on radiographs and their corresponding DRRs ($p = 0.72$). The average \pm standard deviation of alpha angle differences between radiographs and DRRs was $0.2^\circ \pm 2.9^\circ$ with a 95% CI of -0.9° to 1.3° ; limits of agreement were -5.6° and 6.0° . The correlation coefficient of alpha angles between the two image types was $r = 0.99$. The relationship between alpha angles on radiographs compared to DRRs was nearly linear ($y = 0.98x + 1.19$) with excellent agreement ($R^2 = 0.98$). Bland-Altman plots indicated strong agreement between alpha angles measured on DRRs compared to traditional radiographs (Fig. 4.8).

4.7 Acknowledgements

Funding for the recruitment and CT scanning of cam FAI patients was received through NIH grant #R01AR053344. Procurement and CT scanning of the control femurs was done with funds from a U.S. Department of the Army Award #W81XWH-06-1-0574.

4.8 References

1. Barros HJ, Camanho GL, Bernabe AC, et al. 2010. Femoral head-neck junction deformity is related to osteoarthritis of the hip. Clin Orthop Relat Res 468:1920-1925.
2. Beck M, Kalhor M, Leunig M, Ganz R. 2005. Hip morphology influences the pattern of damage to the acetabular cartilage: Femoroacetabular impingement as a cause of early osteoarthritis of the hip. J Bone Joint Surg Br 87:1012-1018.

3. Wagner S, Hofstetter W, Chiquet M, et al. 2003. Early osteoarthritic changes of human femoral head cartilage subsequent to femoro-acetabular impingement. *Osteoarthritis Cartilage* 11:508-518.
4. Ito K, Minka MA, 2nd, Leunig M, et al. 2001. Femoroacetabular impingement and the cam-effect. A mri-based quantitative anatomical study of the femoral head-neck offset. *J Bone Joint Surg Br* 83:171-176.
5. Siebenrock KA, Wahab KH, Werlen S, et al. 2004. Abnormal extension of the femoral head epiphysis as a cause of cam impingement. *Clin Orthop Relat Res*:54-60.
6. Clohisy JC, Carlisle JC, Beaulé PE, et al. 2008. A systematic approach to the plain radiographic evaluation of the young adult hip. *J Bone Joint Surg Am* 90 Suppl 4:47-66.
7. Notzli HP, Wyss TF, Stoecklin CH, et al. 2002. The contour of the femoral head-neck junction as a predictor for the risk of anterior impingement. *J Bone Joint Surg Br* 84:556-560.
8. Tannast M, Siebenrock KA, Anderson SE. 2007. Femoroacetabular impingement: Radiographic diagnosis--what the radiologist should know. *AJR Am J Roentgenol* 188:1540-1552.
9. Clohisy JC, Nunley RM, Otto RJ, Schoenecker PL. 2007. The frog-leg lateral radiograph accurately visualized hip cam impingement abnormalities. *Clin Orthop Relat Res* 462:115-121.
10. Meyer DC, Beck M, Ellis T, et al. 2006. Comparison of six radiographic projections to assess femoral head/neck asphericity. *Clin Orthop Relat Res* 445:181-185.
11. Beaulé PE, Zaragoza E, Motamedi K, et al. 2005. Three-dimensional computed tomography of the hip in the assessment of femoroacetabular impingement. *J Orthop Res* 23:1286-1292.
12. Dudda M, Albers C, Mamisch TC, et al. 2009. Do normal radiographs exclude asphericity of the femoral head-neck junction? *Clin Orthop Relat Res* 467:651-659.
13. Sutter R, Dietrich TJ, Zingg PO, Pfirrmann CW. 2012. How useful is the alpha angle for discriminating between symptomatic patients with cam-type femoroacetabular impingement and asymptomatic volunteers? *Radiology*.

14. Domayer SE, Ziebarth K, Chan J, et al. 2011. Femoroacetabular cam-type impingement: Diagnostic sensitivity and specificity of radiographic views compared to radial mri. *Eur J Radiol* 80:805-810.
15. Pfirrmann CW, Mengiardi B, Dora C, et al. 2006. Cam and pincer femoroacetabular impingement: Characteristic mr arthrographic findings in 50 patients. *Radiology* 240:778-785.
16. Rakhra KS, Sheikh AM, Allen D, Beaulé PE. 2009. Comparison of mri alpha angle measurement planes in femoroacetabular impingement. *Clin Orthop Relat Res* 467:660-665.
17. Carlisle JC, Zebala LP, Shia DS, et al. 2011. Reliability of various observers in determining common radiographic parameters of adult hip structural anatomy. *Iowa Orthop J* 31:52-58.
18. Konan S, Rayan F, Haddad FS. 2010. Is the frog lateral plain radiograph a reliable predictor of the alpha angle in femoroacetabular impingement? *J Bone Joint Surg Br* 92:47-50.
19. Anderson AE, Ellis BJ, Maas SA, Weiss JA. 2010. Effects of idealized joint geometry on finite element predictions of cartilage contact stresses in the hip. *J Biomech* 43:1351-1357.
20. Harris MD, Reese SP, Peters CL, et al. 2013. Three-dimensional quantification of femoral head shape in controls and patients with cam-type femoroacetabular impingement. *Ann Biomed Eng* doi 10.1007/s10439-013-0762-1.
21. Ruff CB, Hayes WC. 1983. Cross-sectional geometry of pecos pueblo femora and tibiae--a biomechanical investigation: I. Method and general patterns of variation. *Am J Phys Anthropol* 60:359-381.
22. Anderson AE, Peters CL, Tuttle BD, Weiss JA. 2005. Subject-specific finite element model of the pelvis: Development, validation and sensitivity studies. *J Biomech Eng* 127:364-373.
23. Harris MD, Anderson AE, Henak CR, et al. 2012. Finite element prediction of cartilage contact stresses in normal human hips. *J Orthop Res* 30:1133-1139.
24. Maas SA, Rawlins DS, Weiss JA. 2012. "Preview" finite element pre-processing. In. Salt Lake City: Musculoskeletal Research Laboratories.
25. Metz CT. 2005. Digitally reconstructed radiographs. MSc, Utrecht University, Utrecht.

26. Eijer H, Leunig M, Mahomed N, Ganz R. 2001. Cross table lateral radiographs for screening of anterior femoral head-neck offset in patients with femoro-acetabular impingement. *Hip Int* 11:37-41.
27. Hansen BJ, Harris MD, Anderson LA, et al. 2012. Correlation between radiographic measures of acetabular morphology with 3d femoral head coverage in patients with acetabular retroversion. *Acta Orthop* 83:233-239.
28. Landis JR, Koch GG. 1977. The measurement of observer agreement for categorical data. *Biometrics* 33:159-174.
29. Barton C, Salineros MJ, Rakhra KS, Beaulé PE. 2011. Validity of the alpha angle measurement on plain radiographs in the evaluation of cam-type femoroacetabular impingement. *Clin Orthop Relat Res* 469:464-469.
30. Johnston TL, Schenker ML, Briggs KK, Philippon MJ. 2008. Relationship between offset angle alpha and hip chondral injury in femoroacetabular impingement. *Arthroscopy* 24:669-675.
31. Beaulé PE, Hynes K, Parker G, Kemp KA. 2012. Can the alpha angle assessment of cam impingement predict acetabular cartilage delamination? *Clin Orthop Relat Res* 470:3361-3367.
32. Jung KA, Restrepo C, Hellman M, et al. 2011. The prevalence of cam-type femoroacetabular deformity in asymptomatic adults. *J Bone Joint Surg Br* 93:1303-1307.
33. Kang AC, Gooding AJ, Coates MH, et al. 2010. Computed tomography assessment of hip joints in asymptomatic individuals in relation to femoroacetabular impingement. *Am J Sports Med* 38:1160-1165.

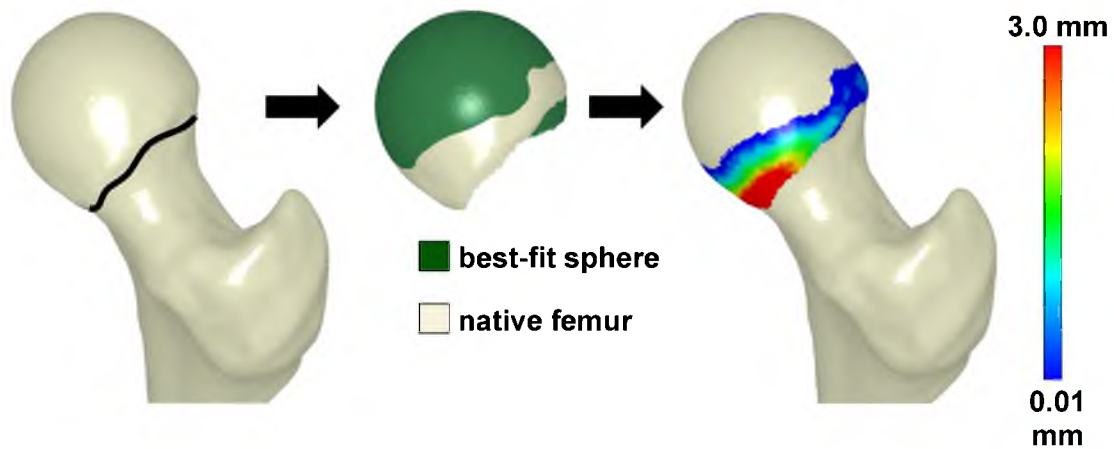


Figure 4.1. Process of femoral head isolation and sphere fitting. Left - The femoral head was delineated from the neck using inflection points around the circumference of the head-neck junction (black line). Middle - The isolated head (off-white) was then projected onto the best fitting sphere surface (green). Right - Deviations (mm) between the femur and the best-fit sphere were calculated across the isolated surface of the head.

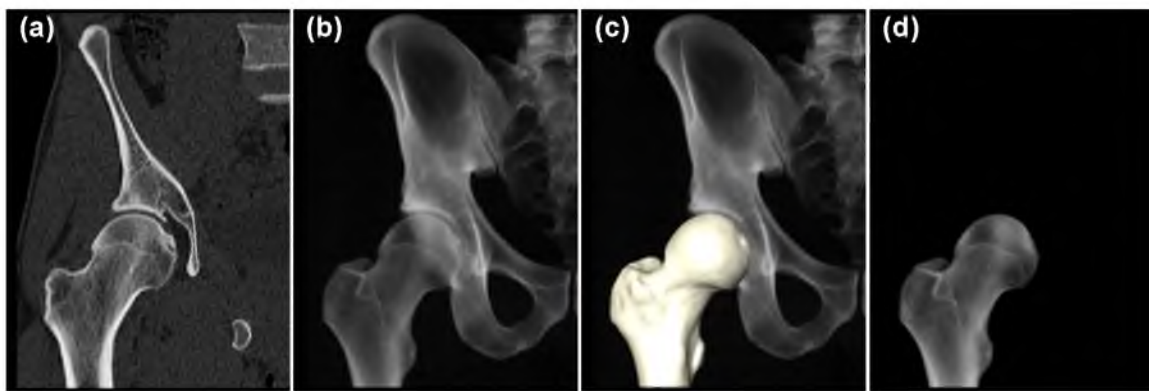


Figure 4.2. DRR generation. From volumetric CT data (a), a DRR was made to visualize only the pelvis and femur bones (b). The segmentation mask used to generate a 3D reconstruction of the femur (c) was then used to isolate a DRR of only the femur (d).

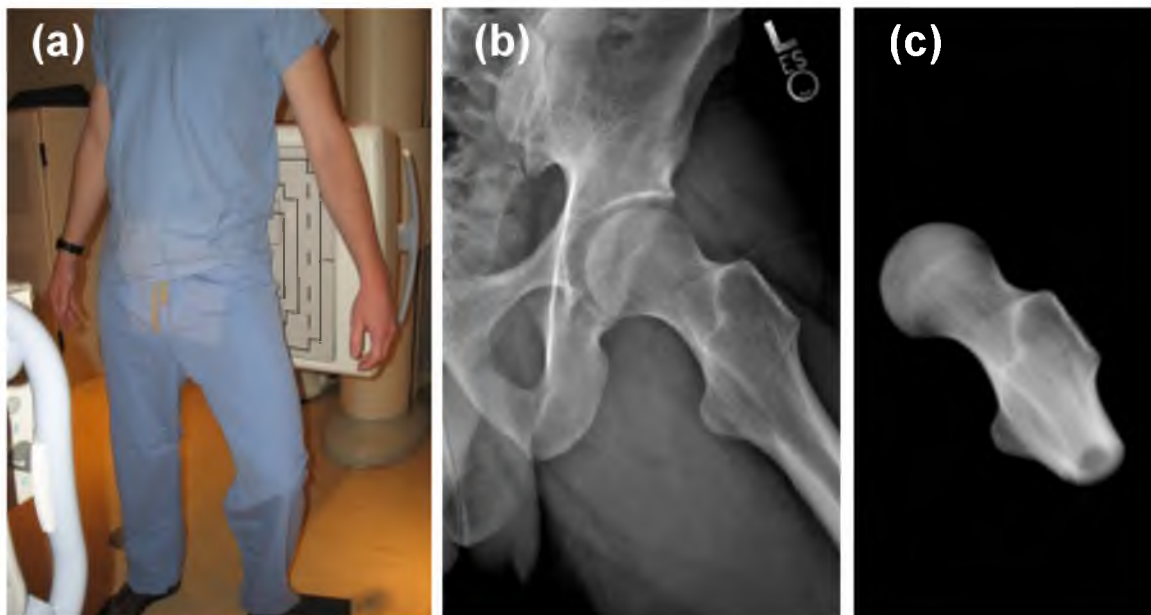


Figure 4.3. DRR alignment routine applied to standing frog-leg lateral. (a) A subject was positioned with the left leg on a 10 cm step with the hip flexed $\sim 35^\circ$ and externally rotated $\sim 60^\circ$. (b) Resulting frog-leg lateral radiograph. (c) A simulated frog-leg lateral DRR, created by transforming the neutral DRR to match the example radiograph.

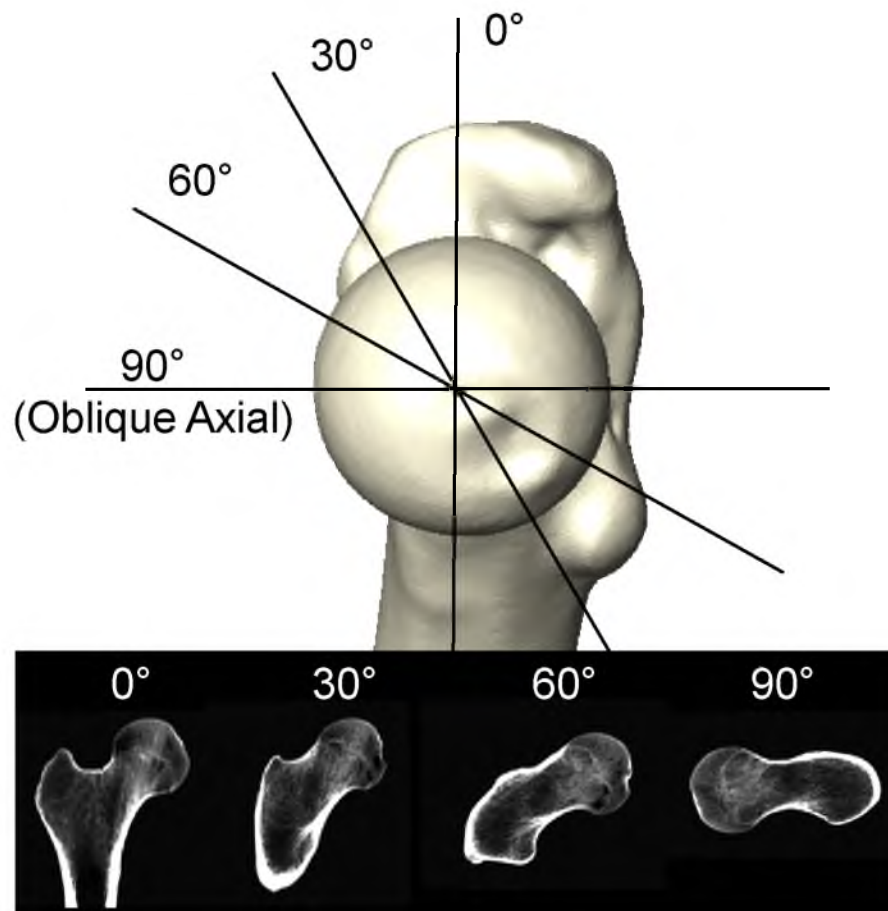


Figure 4.4. Planes and resulting radial CT views for 1 subject. Medial view of the right femur is directly along the axis of rotation between the center of the femoral head and the center of the neck. Four radial CT views were captured from the superior to anterior region of the femoral head.

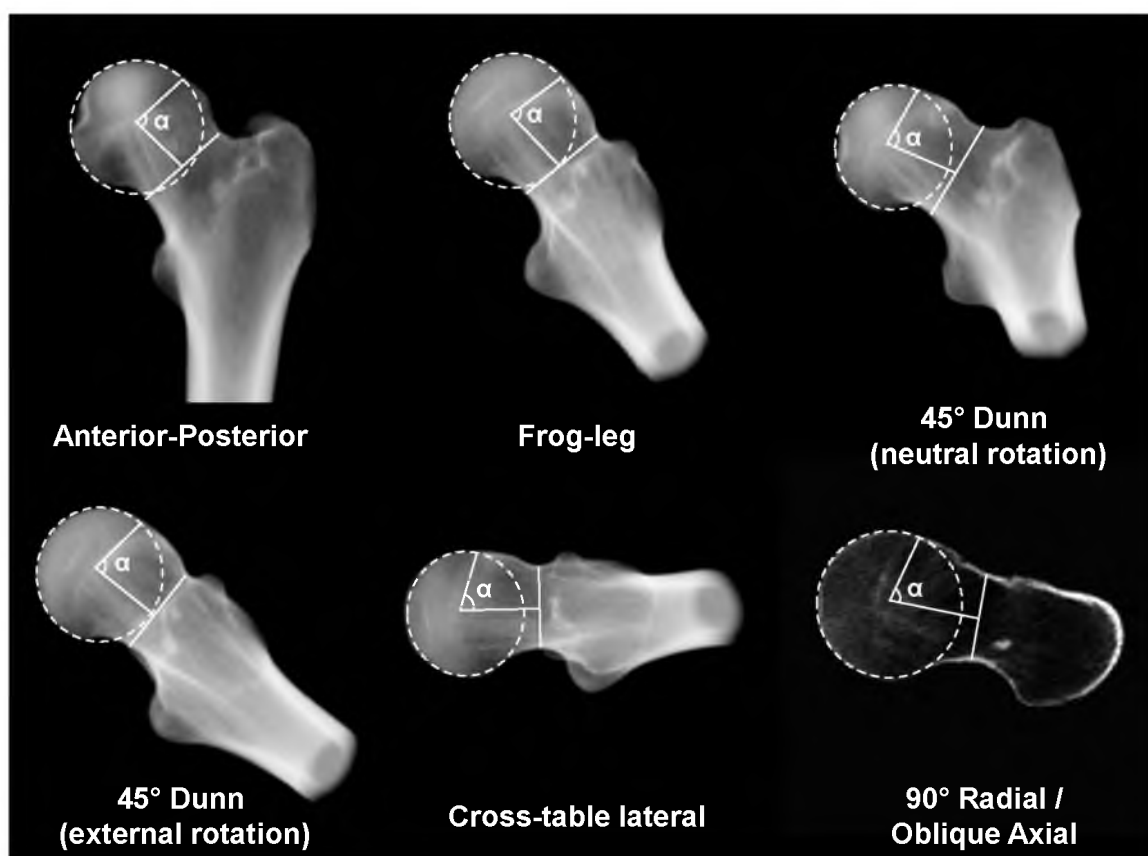


Figure 4.5. Representative DRRs and 90° Radial CT / oblique axial view with alpha angle (α) outlines for a single cam FAI patient.

Table 4.1. Alpha angles and ICCs with 95% confidence intervals for each view. Note – Alpha angles are means \pm standard deviation, ICC is intraclass correlation coefficient, CI is confidence interval.

View	Control Alpha Angle (°)	Cam FAI Alpha Angle (°)	Intraobserver ICC (95% CI)	Interobserver ICC (95% CI)
AP	50.2 \pm 8.8	73.1 \pm 19.6	0.868 (0.742-0.935)	0.832 (0.677-0.916)
Frog-leg Lateral	45.7 \pm 7.0	68.1 \pm 15.4	0.980 (0.958-0.990)	0.955 (0.907-0.978)
45° Dunn (neutral rotation)	56.8 \pm 8.2	80.3 \pm 15.0	0.981 (0.961-0.991)	0.877 (0.759-0.940)
45° Dunn (external rotation)	43.9 \pm 6.6	62.8 \pm 12.8	0.945 (0.889-0.974)	0.886 (0.774-0.944)
Cross-table Lateral	44.1 \pm 7.5	63.7 \pm 11.7	0.975 (0.947-0.988)	0.978 (0.954-0.989)
0° Radial CT	45.7 \pm 4.9	66.5 \pm 19.3	0.981 (0.960-0.991)	0.722 (0.493-0.857)
30° Radial CT	55.5 \pm 9.0	73.9 \pm 14.1	0.924 (0.847-0.963)	0.744 (0.529-0.870)
60° Radial CT	49.0 \pm 6.9	64.9 \pm 8.1	0.929 (0.856-0.965)	0.809 (0.636-0.904)
90° Radial CT (oblique axial)	42.8 \pm 7.0	56.3 \pm 13.0	0.919 (0.837-0.961)	0.885 (0.773-0.943)

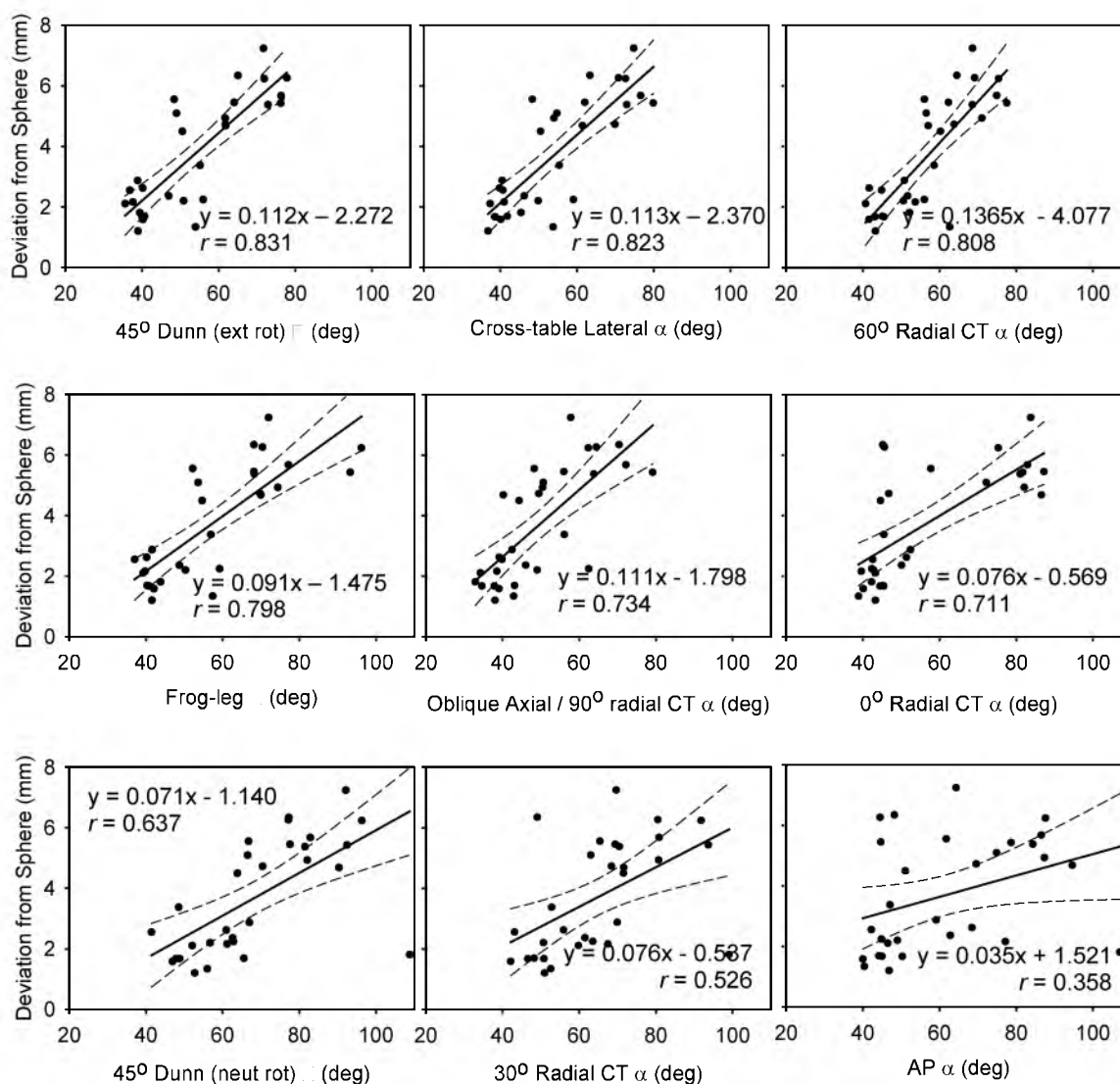


Figure 4.6. Linear regressions (solid line), including 95% confidence intervals (dashed lines), of alpha angles (α) compared to maximum deviations from spheres. Regressions presented in order of decreasing strength.

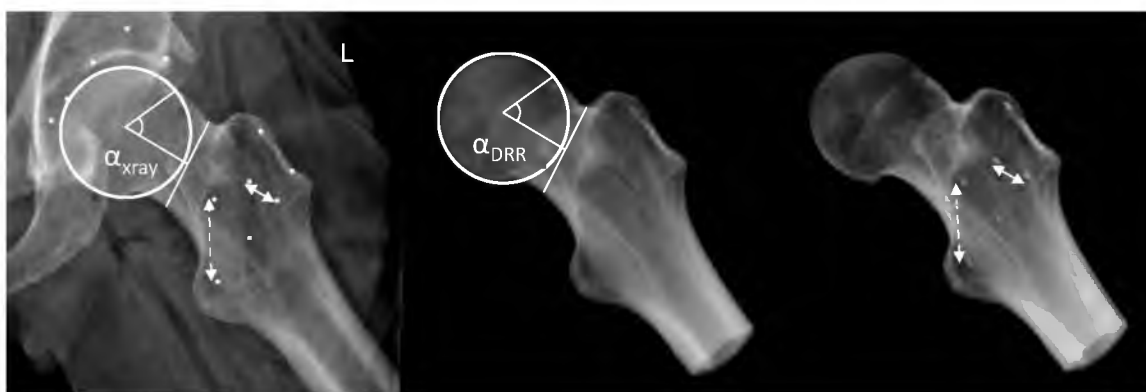


Figure 4.7. DRR validation. Beads were obscured in the CT data and a DRR image was created to match the representative traditional radiograph. Beads were then revealed and a second DRR was created using the transformation matrix used to orient the first DRR. Interbead distances and alpha angles between the DRRs and traditional radiograph were statistically compared. Dashed arrows indicate representative bead distances.

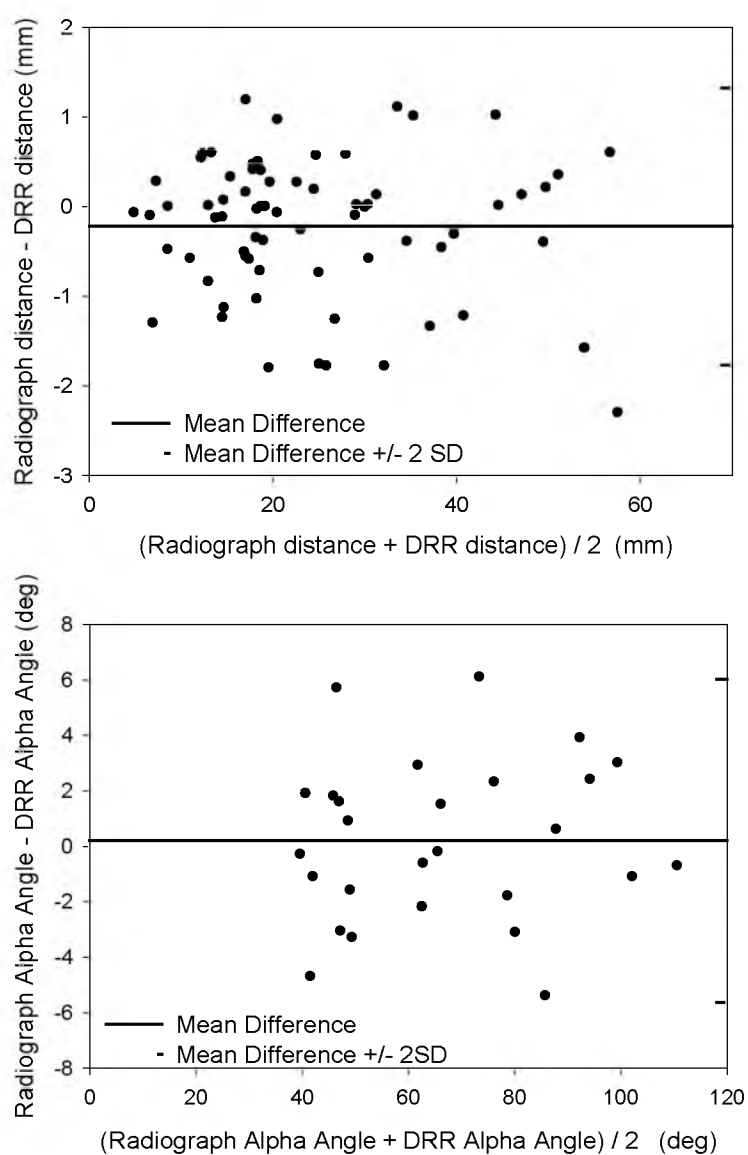


Figure 4.8. Bland-Altman plot of agreement between traditional radiograph and DRR measurements (top: interbead distances, bottom: alpha angles). Solid line represents the mean difference. Dashed lines represent limits of agreement calculated as mean \pm 2*standard deviation

CHAPTER 5

STATISTICAL SHAPE MODELING OF CAM FEMOROACETABULAR IMPINGEMENT

5.1 Abstract

In this study, statistical shape modeling (SSM) was used to quantify three-dimensional (3D) variation and morphologic differences between femurs with and without cam femoroacetabular impingement (FAI). 3D surfaces were generated from CT scans of femurs from 41 controls and 30 cam FAI patients. SSM correspondence particles were optimally positioned on each surface using a gradient descent energy function. Mean shapes for control and patient groups were defined from the resulting particle configurations. Morphological differences between group mean shapes and between the control mean and individual patients were calculated. Principal component analysis was used to describe anatomical variation present in both groups. The first 6 modes (or principal components) captured statistically significant shape variations, which comprised 84% of cumulative variation among the femurs. Shape variation was greatest in femoral offset, greater trochanter height, and the head-neck junction. The mean cam femur shape protruded above the control mean by a maximum of 3.3 mm with sustained protrusions of 2.5-3.0 mm along the anterolateral head-neck junction and distally along the anterior neck, corresponding well with reported cam lesion locations and soft-tissue

damage. This study provides initial evidence that SSM can describe variations in femoral morphology in both controls and cam FAI patients and may be useful for developing new measurements of pathological anatomy. SSM may also be applied to characterize cam FAI severity and provide templates to guide patient-specific surgical resection of bone.

5.2 Introduction

Femoroacetabular impingement (FAI) is caused by reduced clearance between the femoral head and acetabulum due to anatomic abnormalities of the femur (cam FAI), acetabulum (pincer FAI), or both (mixed FAI).¹ Cam FAI is characterized by an aspherical femoral head or reduced femoral head-neck offset. During hip flexion, the abnormally shaped femur may cause shearing at the chondrolabral junction thereby damaging articular cartilage and the acetabular labrum.²

Currently, diagnosis of cam FAI is largely accomplished using two-dimensional (2D) measurements of femur morphology acquired from radiographic projections or a series of radial planes from computed tomography (CT) or magnetic resonance (MR) images.³⁻⁵ Two-dimensional measures provide initial diagnosis of cam FAI, but their reliability has been debated.^{6,7} Also, there is no agreement on the range of measurements that should be considered normal.⁸⁻¹⁰ Furthermore, radiographic measures give only a limited description of femur anatomy or shape variation among cam FAI deformities. Together, these limitations of 2D measurements translate into a high misdiagnosis rate. In a series of FAI patients treated with surgery in our clinic, 40% had seen multiple previous musculoskeletal providers and 15% had undergone surgical procedures unrelated to the hip joint (hernia, etc.).¹¹

Three-dimensional (3D) femur reconstructions from CT images can visualize the entire femoral head. However, evaluations of cam FAI using 3D femur reconstructions have relied on the questionable assumption that a sphere is the ideal femoral head shape.^{12,13} In contrast, statistical shape modeling (SSM) can be applied to 3D reconstructions to objectively compare complex morphology without idealizing underlying geometry.^{14,15} Prior orthopaedic applications of SSM have included analyses of tibiofemoral and patellofemoral joints and methods to reconstruct femur or pelvis shape from sparse image data.¹⁶⁻²² Most SSM strategies distribute a labeled set of points across representative shapes for a given population.^{14,15} Methods of point placement may involve manual placement at anatomic landmarks, derivation from finite element meshes or automatic placement based on point-to-point minimization of distance and entropy.^{14,18,23} Regardless of the method, by optimizing and comparing the positional configurations of the labeled points, SSM can quantify and visualize geometric variation existing within the population.

Application of SSM to a study of cam FAI may facilitate improved diagnosis and preoperative planning. Specifically, SSM can be applied to reconstructions of cam FAI and healthy femurs to generate 3D representatives of the average cam FAI femur compared to the average control. SSM also facilitates quantitative and qualitative analysis of shape variations among femurs which may have clinical use in describing the spectrum of cam FAI deformities and classifying the severity of deformities on a patient-specific basis.

The objective of this study was to generate accurate 3D reconstructions of femoral heads from volumetric CT images and apply SSM to quantify 3D variation and morphologic differences between femurs with and without cam FAI.

5.3 Methods

5.3.1 Subject Selection

A cohort of cam FAI patients was retrospectively collected from patients treated at the University of Utah and Intermountain Healthcare orthopaedic centers. Subject selection and modeling was completed with approval from both institutions (#56086, 1024270). Volumetric CT images of the pelvis and proximal femur were retrospectively acquired from 30 cam FAI patients (28 male, 2 female). All patients had presented with hip and groin pain during activity, tested positive during a clinical impingement exam, showed radiographic evidence of a cam lesion and/or reduced femoral head-neck offset, and were scheduled for hip preservation surgery to address cam FAI. Sixteen CT image sets had been acquired using a Siemens SOMATOM 128 Definition CT Scanner (120kVP tube voltage, 512 x 512 acquisition matrix, 1.0 mm slice thickness, 0.9 to 1.0 pitch, 250 mAs + CareDose tube current, 300-400 mm field-of-view) as part of a previous IRB approved study. The remaining 14 image sets were acquired as part of standard patient care using a GE LightSpeed VCT scanner (120 kVP, 512 x 512, 0.625 slice thickness, 1.0 pitch, 135 mAs, ~230 mm field-of-view).

CT scans for a total of 79 possible control femurs were retrospectively obtained (IRB #56086). Of these, 20 subjects received a CT arthrogram as part of a previous study²⁴ using the Siemens scanner and settings listed above. The control subjects had no

history of hip pain and no radiographic evidence of OA as assessed by a senior musculoskeletal radiologist. The remaining 59 femurs were from a database of cadavers which had been previously CT scanned. Prior to CT scanning, each cadaveric femur was aligned in an anatomic neutral position.²⁵ Images were then acquired using a GE High Speed CTI Single Slice Helical CT Scanner (100 kVp tube voltage, 512 x 512 acquisition matrix, 1.0 mm slice thickness, 1.0 pitch, 100 mAs tube current, 160 mm field of view).

Using the CT images, digitally reconstructed radiographs (DRR) were generated to simulate a standing frog-leg lateral x-ray, with the femur flexed approximately 35° and externally rotated approximately 60°. Radiographic description of head shape was completed for all patients and possible controls by measuring the alpha angle and head neck offset described by Notzli et al. and Ejler et al., respectively, and adapted by Clohisy et al. for the frog-leg lateral view.²⁶⁻²⁸ Femurs were only included as controls if they had an alpha angle less than 55.5° and head-neck offset greater than 7 mm.²⁸ The femurs were also grossly screened for cartilage damage and bony abnormalities. As a result, 38 femurs were excluded from the control group, leaving 41 femurs (29 male, 12 female; 15 live, 26 cadaveric) available as controls for SSM.

5.3.2 Three-dimensional Reconstruction and SSM Preprocessing

The proximal femur to lesser trochanter of each femur was segmented and reconstructed from the CT image data using Amira (v5.4, Visage Imaging, San Diego, CA) and validated threshold settings.²⁹ To improve resolution of the segmentation mask, CT images were up-sampled to 0.22 x 0.22 x 0.33 mm.²⁴ Reconstructed surfaces were triangulated and segmentation artifacts were removed by slightly smoothing surfaces

using tools available in Amira. Femur reconstructions were then cropped at the superior aspect of the lesser trochanter, which was considered to be the most inferior location where cam FAI deformities might extend. The cropped reconstructions were then aligned in Amira using a built-in iterative closest point algorithm to minimize the root mean square (RMS) distance between surfaces. Finally, surface reconstructions were converted to binary segmentations in a uniform bounding box of size 512 x 512 x 512, with an isotropic voxel resolution of 0.24 x 0.24 x 0.24 mm for each femur.

5.3.3 Statistical Shape Modeling

A basic principle of most SSMs is to place particles at corresponding locations on every shape in the population of interest. Optimization routines, designed to minimize descriptive length or entropy, seek to establish particle configurations that conform qualitatively to the anatomy of individuals and capture underlying shape variability in the population as a whole. The current study used the correspondence methods of Cates et al. and Datar et al., which employ a variational formulation of ensemble entropy to optimize particle positioning, as briefly described below.^{14,30} Compared to other SSM methods that rely on relatively few manually placed landmarks or the necessity for training shapes, the SSM techniques of Cates et al. provide a geometrically accurate sampling of individual femurs, while computing a statistically simple model of the ensemble. Consequently, the number of correspondence particles and the ensemble size can be increased without large computational expense. Also with this method, particle initialization is performed automatically, which eliminates error that may be introduced by manually placing particles at anatomic landmarks. The methods of Cates et al. and Datar et al. have been

implemented in the ShapeWorks software and were used to conduct the statistical shape analysis for the current study (<http://www.sci.utah.edu/software/shapeworks.html>).

Binary segmentations of the femurs were output from Amira, preprocessed to remove aliasing artifacts, and 2048 particles were placed on each femur, using an iterative, hierarchical splitting strategy (Fig. 5.1). This strategy proceeded by randomly choosing a surface location and there placing a single particle that was then split to produce a second, nearby particle. Initial locations of the two particles were determined using a system of repulsive forces until a steady state between the particles was achieved. The splitting process and steady state initialization was repeated until 2048 particles were placed on each surface. Thus, the initialization proceeded simultaneously with a preliminary steady state optimization in a multiscale fashion, generating progressively more detailed correspondence models with each split.

The initial particle correspondences were further optimized using a gradient descent approach with a cost function that produced a compact distribution of samples in shape space, while providing uniformly-distributed particle positions on the femur surfaces to achieve a faithful shape representation. The generalized Procrustes algorithm was applied regularly during optimization to align shapes with respect to rotation and translation, and to normalize with respect to scale.³¹ Group labels were used to separate the particle configurations of controls and cam patients, and the mean shape for each group was constructed as the mean of the particle configurations from all shapes belonging to that group.

5.3.4 Analysis

Demographic and radiographic measurements were tested for significant differences between control and patient groups using the Mann-Whitney rank sum test. A Hotelling T^2 test was used to test for group differences between the mean control and patient shapes, with the null hypothesis that the two groups are drawn from the same distribution. Morphological differences were then calculated as the distance between mean shapes or between the control mean and individual cam patients. Principal component analysis (PCA) was used to reduce high-dimensional SSM correspondence data to a smaller set of linearly uncorrelated components (i.e., modes) that describe the variation existing within the ensemble of femur shapes. Principal component loading values (i.e., PC scores) were determined for all femurs and parallel analysis was used to determine the number of modes containing non-spurious, or significant, shape variation.³² Application of parallel analysis prevented the under-extraction (i.e., loss of meaningful information) or over-extraction (i.e., inclusion of random noise) in the analysis of shape variation. Principal component loading values were compared between control and patient groups for modes found to contain significant information using Student's t-test with a Finner's adjustment for multiple comparisons.³³ PCA was then applied to the control and patient groups separately to determine major intra-group variations.

Shape variation (i.e., PC loading values) was correlated with existing 2D and 3D measures of femoral anatomy using Pearson's correlation coefficient. First, PC loading values were correlated with 2D alpha angle and head-neck offset measurements. Next, native 3D reconstructions of each femoral head were isolated from the femur at the head-neck junction and fit to a sphere. Maximum deviations were then measured as the

distance between the native head and the corresponding best-fit sphere.³⁴ Maximum deviations were then correlated with PC loading values, alpha angles and head-neck-offsets.

5.4 Results

The average and standard deviation age, weight, height, and BMI of the patients and (controls) were 27 ± 8 (31 ± 10) years, 84 ± 15 (80 ± 18) kg, 181 ± 8 (177 ± 8) cm, and 25.6 ± 4.3 (25.4 ± 5.5) kg/m², respectively. Alpha angles and head-neck offsets of the patients and (controls) were $68.4 \pm 15.6^\circ$ ($43.0 \pm 5.2^\circ$) and 4.4 ± 1.7 (7.3 ± 1.6) mm, respectively. Age, weight, and BMI values were not significantly different between controls and patients ($p \geq 0.105$), whereas alpha angles and head-neck offsets were significantly different between the groups ($p < 0.001$).

The Hotelling T² test demonstrated significant differences between the patient and control mean shapes ($p < 0.001$). Morphologically, the patient mean shape was found to protrude above the control mean by a maximum of 3.3 mm in the anterolateral head-neck junction (Fig. 5.2). Sustained protrusions of ~2.5-3.0 mm were distributed from the anterior-posterior midline of the femoral neck along the anterolateral head-neck junction and distally along the anterior neck. Maximum deviations between individual patient femur shapes and the mean control shape were primarily in the anterosuperior to anterolateral head-neck junction, and ranged between 2.3 mm and 8.3 mm.

The first 12 modes captured 90% of the cumulative variation among the femurs (Fig. 5.3). However, parallel analysis determined that the first 6 modes captured statistically significant (nonspurious) variation and were used for further analysis. The 6

modes captured 83.8% of the cumulative variation among all femurs. Specifically, mode 1 captured 35.2% of the variation, followed by mode 2 at 21.8%, mode 3 at 15.2%, mode 4 at 6.9%, mode 5 at 2.5%, and mode 6 at 2.2% of the variation, respectively. PC loading values between controls and patients were significant ($p < 0.001$) for the first two modes.

PCA, run on the control and patient groups independently, showed similar areas of intragroup variation. Qualitative and quantitative descriptions of variation captured by the first three modes are shown in Figure 5.4. For both groups, variation in mode 1 was most substantial at the femoral offset (i.e., medial-lateral distance from tip of greater trochanter to center of the femoral head) and the distance between the proximal tip of the greater trochanter and the proximal lesser trochanter. For the patient group, mode 1 also captured variation in concavity at the head-neck junction. For both groups, mode 2 primarily described variation in the diameter of the femoral neck. Finally, mode 3 captured variation in the curvature of the greater trochanter in both groups.

Correlations of alpha angles and head-neck offsets with PC loading values from the first four modes were moderate to weak. Specifically, Pearson's correlation coefficients for alpha angles and (head-neck offsets) with PC loadings were $r = 0.407$ (-0.288), 0.357 (-0.345), and 0.137 (0.119) for modes 1, 2, and 3, respectively.

Maximum deviations from best-fit spheres were 1.95 ± 0.61 mm for the control subjects and 4.79 ± 1.54 mm for patient femurs. Maximum deviations were significantly different between patients and controls ($p < 0.001$). Correlations between maximum deviation and PC loading values were moderate to weak, with Pearson's correlation coefficients of $r = 0.433$, 0.360, and 0.168 for modes 1, 2, and 3, respectively.

Correlations between radiographic measurements and maximum deviations were $r = 0.863$ (alpha angle) and $r = -0.696$ (head-neck offset).

5.5 Discussion

This study used SSM to quantify and compare femoral head morphology between control and cam FAI femurs. A primary result of this study was the computation of mean femoral shapes for controls and cam FAI patients. The greatest differences between the mean shapes were located along the anterolateral head-neck junction, which corresponds very well with the locations of cam lesions and corresponding joint damage reported in the literature.^{2,35}

Considerable variation was found in the shape and height of the greater trochanter, among all femurs and between groups. There were also large variations among femurs in the distance between the greater trochanter and the center of the femoral head (i.e., femoral offset) as well as the diameter of the femoral neck. This finding alone demonstrates the potential utility of SSM for objectively describing variations in femoral shape and the spectrum of possible deformities, which would otherwise be difficult to identify using traditional radiographs.

Mean shapes calculated using SSM, as well as color plots of individual cam femurs compared to the mean shapes, could be used to improve the diagnosis and treatment of FAI. For example, a 3D reconstruction of a single patient with cam FAI could be objectively compared to the mean pathological shape to assess disease severity (relative to other cam patients), or could be compared to the mean control femur to produce a map elucidating the magnitude and location of bone debridement required to

make the femoral head normal in appearance (Fig. 5.5). Under-correction of a cam lesion may cause lingering pain and could require revision surgery, while over correction could endanger the mechanical integrity or blood supply of the femur.^{36,37} Three-dimensional debridement maps from objective SSM could facilitate more exact surgical planning and may reduce instances of under- or over-correction of cam deformities.

A persistent clinical problem with diagnosing cam FAI is the establishment of rubrics that can reliably distinguish pathologic from normal femurs. Along with quantifying the spectrum of deformities and variations previously unknown to exist between groups, the current study also demonstrates how SSM could be used to develop new, and perhaps more reliable measurements of anatomy to diagnose FAI. For instance, SSM suggested that the distance between the greater and lesser trochanters was highly variable and different between groups. While these results are preliminary, the disparity in greater trochanter morphologies may be indicative of a developmental deformity at the trochanteric physis during early adolescence, concomitant with suggested capital femoral physeal deformities.^{38,39}

Our results also suggest that femoral offset is largely variable in both control and cam FAI subjects. This variability may contribute to susceptibility for FAI by reducing available clearance between the lateral acetabular rim and proximal femoral neck during extreme ranges of motion. Considerable variability in the concavity of the head-neck junction in cam FAI patients and femoral neck diameter in all subjects, as captured by modes 1 and 2, respectively, is likely to further contribute to the susceptibility for FAI.

Comparison of PC loading values between controls and patients suggested that variation captured within the first two modes may be the most useful for identifying

shape alterations that are a contribution of the FAI disease rather than inherent femur population variance. Such localized information about variation among control and cam femurs could help physicians classify unusual FAI cases and comprehensively characterize complex morphological variations that distinguish healthy and pathologic hips.

There was a strong correlation between alpha angles from the frog-leg lateral view and maximum deviations from a sphere, likely because these measures assume circular/spherical geometry. However, only moderate to weak correlative relationships were found between shape variations captured by SSM and existing 2D and 3D measures of femoral morphology. The relatively weak correlations between SSM-derived data and radiographic measurements observed in our study suggest that current radiographic criteria may not adequately describe the underlying variation in anatomy observed in FAI patients. In the future, it may be possible to relegate 3D SSM-derived data to 2D radiographs of an average normal/FAI subject, which could serve as a template in which to compare individual patient radiographs.

A few limitations of this study warrant discussion. First, there is some risk that subjects included in the control cohort could have had subtle forms of FAI. In our study, we used the most widely recognized radiographic measures of cam FAI (alpha angle from a lateral view, and head-neck offset) to establish inclusion criteria. We also used three levels of exclusion criteria in the consideration of our control group (evidence of osteoarthritis, gross bony deformities, alpha angle and head-neck offset values outside previously reported ranges for asymptomatic subjects^{9,26}). Alpha angles, head-neck offsets and 3D maximum deviations from a sphere were all significantly, and

substantially, different between the control and cam FAI femurs. Thus, we believe the two groups were sufficiently distinct. Another limitation was that SSM was not applied to the acetabulum. In our study, a few patients were treated for chondrolabral damage on the acetabulum, which may have been caused by acetabular deformities (i.e., mixed FAI). However, the primary diagnosis of the patients was cam-type FAI. Future research will include methods to simultaneously consider both the femoral and acetabular sides of the hip joint. Finally, it is possible that alignment errors between femoral reconstructions could affect SSM results. To reduce errors of this type, femoral reconstruction alignment was controlled using a strict relative RMS error stipulation and the generalized Procrustes algorithm was applied during optimization, which assisted in removing any residual, non-shape information from the model.

In conclusion, we have shown that SSM can be used to differentiate anatomical differences in the shape of proximal femur between cam FAI patients and control subjects. The methodologies described in the current study lay the groundwork for additional research studies as well as the deployment of SSM as a clinical tool. For example, because of its objectivity, SSM could be used to stage disease severity (e.g., assign z-scores), which would be particularly useful for patients who are symptomatic, but do not have obvious deformities. As a pre- or intraoperative surgical tool, SSM could be used to characterize the amount of bone that should be resected during surgery to restore normal appearance in shape. Finally, SSM data could be used to identify novel anatomical variations between groups, which could in turn be used to develop more sensitive and specific measurements. It may be possible to modify our SSM approach to

output an average ‘normal’ and FAI radiograph that could be used as a template to efficiently diagnose patients.

5.6 Acknowledgements

This project was supported by the National Institutes of Health (R01AR05344, P41RR012553-14, P41 GM103545-14), NIH/NCBC National Alliance for Medical Image Computing (U54-EB005149), and the National Science Foundation (CCF-073222). The authors also thank Dr. Hugh West Jr., of Intermountain Healthcare.

5.7 References

1. Ganz R, Parvizi J, Beck M, et al. 2003. Femoroacetabular impingement: A cause for osteoarthritis of the hip. *Clin Orthop Relat Res*:112-120.
2. Beck M, Kalhor M, Leunig M, Ganz R. 2005. Hip morphology influences the pattern of damage to the acetabular cartilage: Femoroacetabular impingement as a cause of early osteoarthritis of the hip. *J Bone Joint Surg Br* 87:1012-1018.
3. Beaulé PE, Zaragoza E, Motamedi K, et al. 2005. Three-dimensional computed tomography of the hip in the assessment of femoroacetabular impingement. *J Orthop Res* 23:1286-1292.
4. Clohisy JC, Carlisle JC, Beaulé PE, et al. 2008. A systematic approach to the plain radiographic evaluation of the young adult hip. *J Bone Joint Surg Am* 90 Suppl 4:47-66.
5. Rakhra KS, Sheikh AM, Allen D, Beaulé PE. 2009. Comparison of mri alpha angle measurement planes in femoroacetabular impingement. *Clin Orthop Relat Res* 467:660-665.
6. Barton C, Salineros MJ, Rakhra KS, Beaulé PE. 2011. Validity of the alpha angle measurement on plain radiographs in the evaluation of cam-type femoroacetabular impingement. *Clin Orthop Relat Res* 469:464-469.
7. Clohisy JC, Carlisle JC, Trousdale R, et al. 2009. Radiographic evaluation of the hip has limited reliability. *Clin Orthop Relat Res* 467:666-675.

8. Allen D, Beaulé PE, Ramadan O, Doucette S. 2009. Prevalence of associated deformities and hip pain in patients with cam-type femoroacetabular impingement. *J Bone Joint Surg Br* 91:589-594.
9. Pollard TC, Villar RN, Norton MR, et al. 2010. Femoroacetabular impingement and classification of the cam deformity: The reference interval in normal hips. *Acta Orthop* 81:134-141.
10. Sutter R, Dietrich TJ, Zingg PO, Pfirrmann CW. 2012. How useful is the alpha angle for discriminating between symptomatic patients with cam-type femoroacetabular impingement and asymptomatic volunteers? *Radiology* 264:514-521.
11. Peters CL, Erickson JA. 2006. Treatment of femoro-acetabular impingement with surgical dislocation and debridement in young adults. *J Bone Joint Surg Am* 88:1735-1741.
12. Almoussa S, Barton C, Speirs AD, et al. 2011. Computer-assisted correction of cam-type femoroacetabular impingement: A sawbones study. *J Bone Joint Surg Am* 93 Suppl 2:70-75.
13. Audenaert EA, Baelde N, Huysse W, et al. 2011. Development of a three-dimensional detection method of cam deformities in femoroacetabular impingement. *Skeletal Radiol* 40:921-927.
14. Cates J, Fletcher PT, Styner M, et al. 2007. Shape modeling and analysis with entropy-based particle systems. *Inf Process Med Imaging* 20:333-345.
15. Cootes TF, Taylor CJ, Cooper DH, Graham J. 1995. Active shape models-their training and application. *Comput Vis Image Underst* 61:38-59.
16. Bredbenner TL, Eliason TD, Potter RS, et al. 2010. Statistical shape modeling describes variation in tibia and femur surface geometry between control and incidence groups from the osteoarthritis initiative database. *J Biomech* 43:1780-1786.
17. Bryan R, Mohan PS, Hopkins A, et al. 2010. Statistical modelling of the whole human femur incorporating geometric and material properties. *Med Eng Phys* 32:57-65.
18. Fitzpatrick CK, Baldwin MA, Laz PJ, et al. 2011. Development of a statistical shape model of the patellofemoral joint for investigating relationships between shape and function. *J Biomech* 44:2446-2452.

19. Blanc R, Seiler C, Szekely G, et al. 2012. Statistical model based shape prediction from a combination of direct observations and various surrogates: Application to orthopaedic research. *Med Image Anal* 16:1156-1166.
20. Zheng G, Dong X, Rajamani KT, et al. 2007. Accurate and robust reconstruction of a surface model of the proximal femur from sparse-point data and a dense-point distribution model for surgical navigation. *IEEE Trans Biomed Eng* 54:2109-2122.
21. Barratt DC, Ariff BB, Humphries KN, et al. 2004. Reconstruction and quantification of the carotid artery bifurcation from 3-d ultrasound images. *IEEE Trans Med Imaging* 23:567-583.
22. Meller S, Kalendar WA. 2004. Building a statistical shape model of the pelvis. *ICS* 1268:561-566.
23. Davies RH, Twining CJ, Cootes TF, et al. 2002. A minimum description length approach to statistical shape modeling. *IEEE Trans Med Imaging* 21:525-537.
24. Harris MD, Anderson AE, Henak CR, et al. 2012. Finite element prediction of cartilage contact stresses in normal human hips. *J Orthop Res* 30:1133-1139.
25. Ruff CB, Hayes WC. 1988. Sex differences in age-related remodeling of the femur and tibia. *J Orthop Res* 6:886-896.
26. Clohisy JC, Nunley RM, Otto RJ, Schoenecker PL. 2007. The frog-leg lateral radiograph accurately visualized hip cam impingement abnormalities. *Clin Orthop Relat Res* 462:115-121.
27. Eijer H, Leunig M, Mahomed N, Ganz R. 2001. Cross table lateral radiographs for screening of anterior femoral head-neck offset in patients with femoro-acetabular impingement. *Hip Int* 11:37-41.
28. Notzli HP, Wyss TF, Stoecklin CH, et al. 2002. The contour of the femoral head-neck junction as a predictor for the risk of anterior impingement. *J Bone Joint Surg Br* 84:556-560.
29. Anderson AE, Ellis BJ, Peters CL, Weiss JA. 2008. Cartilage thickness: Factors influencing multidetector ct measurements in a phantom study. *Radiology* 246:133-141.
30. Datar M, Cates J, Fletcher PT, et al. 2009. Particle based shape regression of open surfaces with applications to developmental neuroimaging. *Med Image Comput Comput Assist Interv* 12:167-174.
31. Gower J. 1975. Generalized procrustes analysis. *Psychometrika* 40:33-51.

32. Franklin SB, Gibson DJ, Robertson PA, et al. 1995. Parallel analysis: A method for determining significant principal components. *J Veg Sci* 6:99-106.
33. Finner H. 1993. On a monotonicity problem in step-down multiple test procedures. *J Am Stat Assoc* 88:920-923.
34. Harris MD, Reese PR, Peters CL, et al. 2011. 3d morphological assessment of cam femoroacetabular impingement. In, 2011 Utah Biomedical Engineering Conference. Salt Lake City, UT, USA.
35. Peters CL, Erickson JA, Anderson L, et al. 2009. Hip-preserving surgery: Understanding complex pathomorphology. *J Bone Joint Surg Am* 91 Suppl 6:42-58.
36. Mardones RM, Gonzalez C, Chen Q, et al. 2006. Surgical treatment of femoroacetabular impingement: Evaluation of the effect of the size of the resection. Surgical technique. *J Bone Joint Surg Am* 88 Suppl 1 Pt 1:84-91.
37. Philippon MJ, Schenker ML, Briggs KK, et al. 2007. Revision hip arthroscopy. *Am J Sports Med* 35:1918-1921.
38. Ogden JA. 1990. Skeletal injury in the child. W.B. Saunders Company, Philadelphia, PA.
39. Siebenrock KA, Wahab KH, Werlen S, et al. 2004. Abnormal extension of the femoral head epiphysis as a cause of cam impingement. *Clin Orthop Relat Res*:54-60.

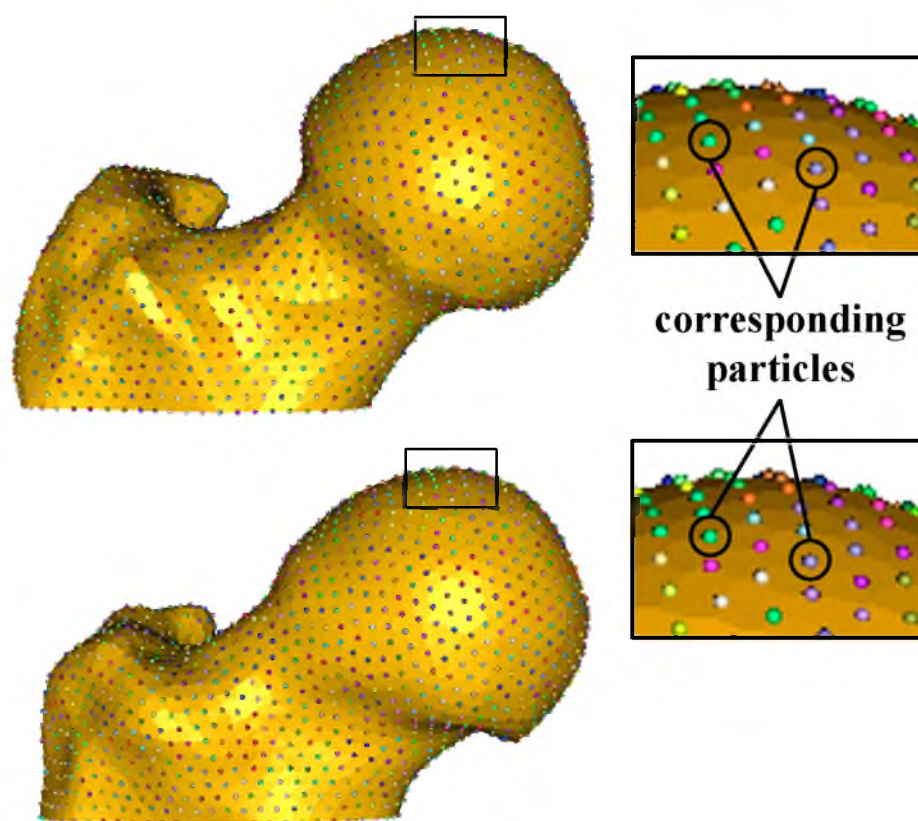


Figure 5.1. Correspondence particle distribution on a control (top) and cam FAI (bottom) femur. Particles ($n=2048$) were placed on each femur and optimally positioned to balance model compactness and accurate shape representation.

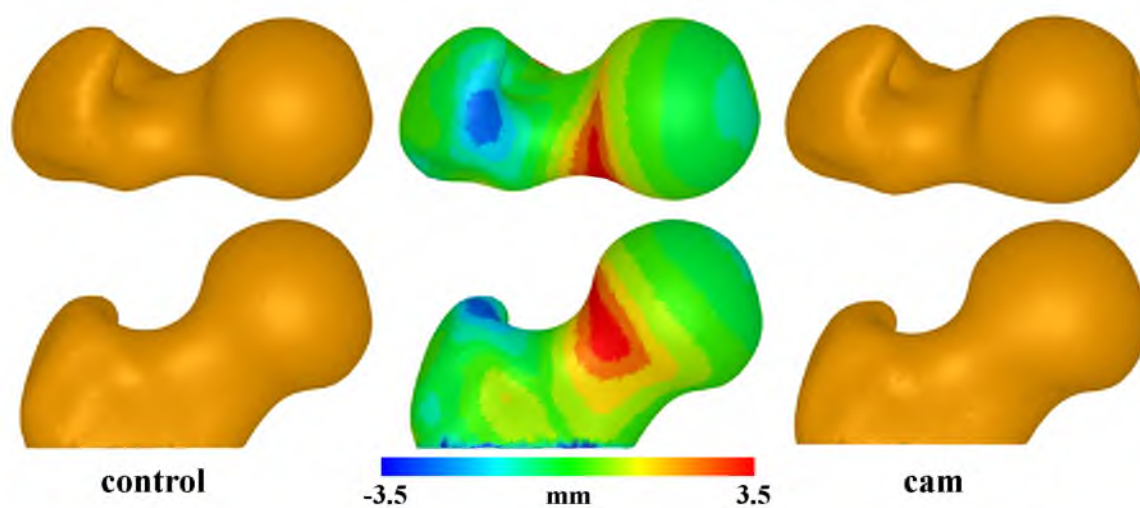


Figure 5.2. Mean control (left) and cam (right) shapes. Middle images demonstrate how the mean cam shape differed relative to the mean control shape (shown). Top and bottom rows show different rotations of the femoral head.

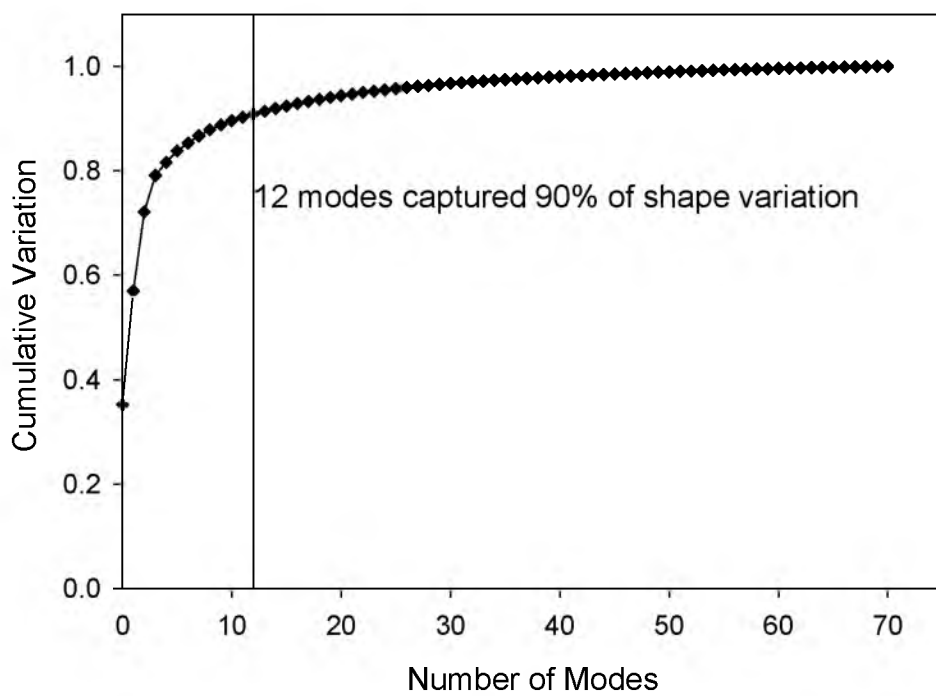


Figure 5.3. Cumulative shape variation captured in the 70 PCA modes when PCA was run for all femurs. Ninety percent of the variation was captured in the first 12 modes.

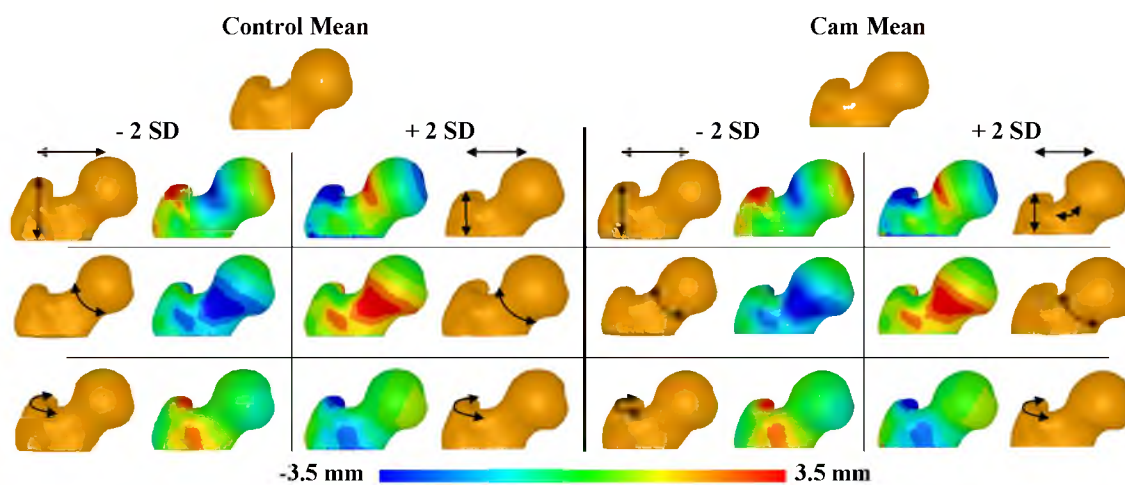


Figure 5.4. Shape variation captured in the first 3 modes. PCA was run independently on the control and patient femur groups. From the mean, shapes are shown at ± 2 SD shown for each group in each mode. Color plots indicate differences between various shapes and the means (shown). Arrows qualitatively show areas of greatest variation captured by each mode.

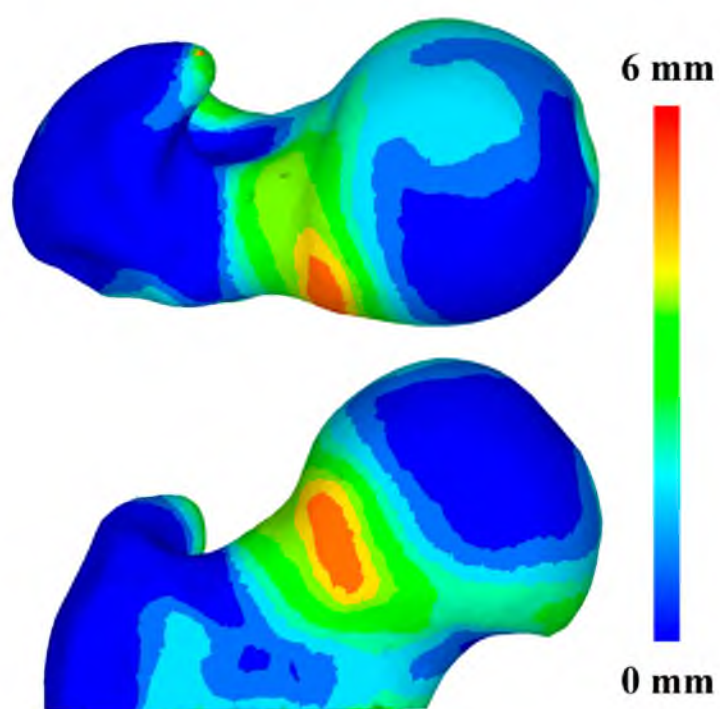


Figure 5.5. Color plot of a single cam FAI femur (shown) and the amount it deviates from the average control femur. These plots could be used as guide for planning surgical debridement to relieve FAI.

CHAPTER 6

FINITE ELEMENT PREDICTION OF CARTILAGE CONTACT STRESSES IN NORMAL HUMAN HIPS¹

6.1 Abstract

The objectives of this research were to determine cartilage contact stress during walking, stair climbing and descending stairs in a well-defined group of normal volunteers, and to assess variations in contact stress and area between subjects and across loading scenarios. Ten volunteers without history of hip pain or disease, with normal lateral center-edge angle and acetabular index were selected. Computed tomography imaging with contrast was performed on one hip. Bone and cartilage surfaces were segmented from volumetric image data, and subject-specific finite element models were constructed and analyzed using a validated protocol. Acetabular contact stress and area were determined for 7 activities. Peak stress ranged from 7.52 ± 2.11 MPa for heel-strike during walking (233% BW) to 8.66 ± 3.01 MPa for heel-strike during descending stairs (261% BW). Average contact area across all activities was 34% of the surface area of the acetabular cartilage. The distribution of contact stress was highly nonuniform, and there was more variability between subjects for a given activity than between activities for a

¹Reprint of article: "Finite element prediction of cartilage contact stresses in normal human hips," *J Orthop Res*. Harris MD, Anderson AE, Henak CR, Ellis BJ, Peters CL, Weiss JA. 2012;30(7):1133-1139. Reprinted with permission from John Wiley and Sons. License Number: 3012690834922.

single subject. The magnitude and area of contact stress were consistent between activities, although there were interactivity shifts in contact pattern as the direction of loading changed. Relatively small incongruencies between the femoral and acetabular cartilage had a large effect on the contact stresses. These effects tended to persist across all simulated activities. These results demonstrate the diversity and trends in cartilage contact stress in healthy hips during activities of daily living and provide a basis for future comparisons between normal and pathologic hips.

6.2 Introduction

Contact stresses in the human hip play an important role in maintaining joint health and pain-free ambulation. Abnormal contact stresses are thought to be a primary cause of hip osteoarthritis (OA).^{1,2} While a number of factors contribute to the progression of OA, studies have suggested that bony abnormalities such as dysplasia and femoroacetabular impingement (FAI) accelerate the onset of the disease.³⁻⁷

Despite the importance of cartilage contact stresses to joint health, there is still disagreement in the literature regarding the normal magnitudes and distributions of contact stress in the healthy hip. In vitro measurements of contact stress have used pressure-sensitive film or piezo-resistive sensors.⁸⁻¹⁰ It is difficult to quantify contact stress on the entire articulating surface with these techniques, and there is a limited range of stresses that can be measured. In vivo experimental studies have used instrumented prostheses to measure equivalent joint reaction forces.¹¹⁻¹⁴ These measurements only approximate the true cartilage stresses since one joint surface has been replaced with a

spherical implant. To date, there are no experimental methods available to assess hip contact stresses on a subject-specific basis.

Computational methods provide the means to predict hip joint cartilage mechanics for individual subjects. Contact stresses in the hip have been predicted using both the discrete element analysis (DEA) technique^{15,16} and the finite element (FE) method.¹⁷⁻¹⁹ These studies reported proof-of-concept and results of parametric studies, but simplifying assumptions and a lack of validation limited their ability to provide definitive measurements of the magnitude and distribution of contact stresses in normal hips.

Experimental and computational reports on contact stresses in the hip have not incorporated clear exclusion criteria to define the “normal” hip. In the clinic, radiographic measurements are used to define geometric abnormalities or cartilage degradation, while a detailed patient history can help to rule out preexisting pathologies. The objectives of this research were to determine cartilage contact stresses during walking, stair climbing and descending stairs in a well-defined group of normal volunteers, and to assess variations in contact stresses and areas between subjects and across loading scenarios. This was accomplished by constructing and analyzing subject-specific finite element models of the volunteers using a validated protocol.²⁰

6.3 Methods

6.3.1 Subject Selection and CT Imaging

Human volunteers were recruited to approximately match the age, weight, and body mass index (BMI) of patients with acetabular dysplasia commonly treated at our clinic. An institutional review board approved this study, and informed consent was

received from sixteen volunteers (7 female, 9 male) with no history of hip pain or disease.

One hip from each subject was selected randomly to receive a CT arthrogram. The hip capsule was injected with ~20 ml of a diluted contrast agent (2:1 lidocaine to OMNIPAQUE® 350, GE Healthcare Inc, Princeton, NJ) under fluoroscopic guidance. Multidetector CT scans of the entire pelvis and both femurs were obtained within 10 minutes of injection (120 kVp, 100-400 mAs, 512×512 matrix, 1.0 pitch, 300-400 mm FOV, 1.0 mm slice thickness) using a Siemens SOMATOM Definition CT Scanner. Joint traction was applied during the scan using a hare traction device to ensure that the contrast agent filled the joint space (Fig. 6.1a).

The CT images were read by a senior radiologist and an orthopaedic surgeon. The inclusion criteria for the study required the hips to have a lateral center-edge angle between 25-40 degrees,^{21,22} acetabular index angle (acetabular inclination or Tonnis angle) between 0-10 degrees,^{23,24} qualitatively normal joint congruity, bone sphericity and cartilage morphology, and no signs of OA. CT images needed to show distribution of contrast sufficient to distinguish acetabular and femoral cartilage (Fig. 6.1a). Based on these criteria, 6 subjects were excluded from the study. For the remaining 10 subjects (5 female, 5 male), the lateral center-edge angle was 33.5 ± 5.4 degrees and acetabular index was 4.6 ± 3.7 degrees. Age, weight and BMI of the subjects were 26 ± 4 years, 70.0 ± 13.9 kg and 23 ± 3.8 , respectively.

6.3.2 Surface Reconstruction, Mesh Generation and Constitutive Models

Bone and cartilage surfaces were segmented from the CT image data using the Amira software (5.3, Visage Imaging, San Diego, CA) and previously validated threshold settings.²⁵⁻²⁷ CT images were up-sampled using a Lanczos filter kernel (1536×1536; 0.3 mm thickness) to improve the resolution of the segmentation mask (Fig. 6.1a). Additional up-sampling did not change FE predictions appreciably. Reconstructed surfaces were decimated to reduce the number of polygons and smoothed with a low pass filter to remove segmentation artifacts.

Surfaces were discretized using hexahedral and triangular shell elements (Fig. 6.1b, c). Hexahedral meshes were constructed for the cartilage layers using TrueGrid (XYZ Scientific, Livermore, CA). Cortical bone surfaces were discretized using shell elements. Mesh densities were determined from mesh convergence studies.²⁰ Trabecular bone was not included in the models, as it has little effect on predictions of contact stress.²⁰ Tied and sliding contact algorithms based on the mortar method were used to define the cartilage-to-bone and cartilage-to-cartilage interfaces, respectively.²⁸ Frictionless contact was assumed for the cartilage-to-cartilage interface. The friction coefficient between articulating cartilage surfaces is very low, on the order of 0.01-0.02 in the presence of synovial fluid.²⁹ Therefore, it is reasonable to neglect frictional shear stresses between contacting articular surfaces.

Cartilage was modeled as a homogeneous, isotropic, nearly incompressible, neo-Hookean hyperelastic material with shear modulus $G = 13.6$ MPa and bulk modulus $K = 1,359$ MPa ($\nu = 0.495$).²⁰ Cortical bone was modeled as a homogeneous, isotropic material with elastic modulus $E = 17$ GPa and Poisson's ratio $\nu = 0.29$.²⁰

6.3.3 Model Positioning, Boundary Conditions and Loading

Rigid node sets were created at the sacroiliac and pubis symphysis joints. Motion was applied superiorly to the distal femur to load the femur/acetabulum contact interface. The femur was allowed to translate in the medial-lateral and anterior-posterior directions as it was displaced superiorly to facilitate seating of the femoral head in the acetabulum. To eliminate rigid body modes, motion along the medial-lateral and anterior-posterior directions was resisted by four orthogonal linear springs ($k = 1 \text{ N/m}$) placed at the distal femur.

Seven loading scenarios were used to simulate activities of daily living (Fig. 6.1d-j). First, neutral pelvic and femoral positions were established using anatomical landmarks.¹² Next, the femur and pelvis were reoriented based on in vivo kinematic and kinetic hip joint data.¹¹ Five of the loading scenarios corresponded to time points during the gait cycle: the peak of hip contact force following heel strike (WHS), the midpoint between heel strike and midstance (WHM), midstance (WMD), the midpoint between midstance and the late stance hip contact force peak (WML), and the late stance peak (WLS). Peaks in force following heel strike were simulated for the activities of ascending stairs (AHS) and descending stairs (DHS). A target hip contact force (HCF) for each activity was scaled to bodyweight (BW) according to Bergmann's average subject – WHS (233% BW), WHM (215% BW), WMD (203% BW), WML (204% BW), WLS (205% BW), AHS (252% BW) and DHS (261% BW). PreView was used for pre-processing,³⁰ NIKE3D (Lawrence Livermore National Laboratory; Livermore, CA) was used for all FE analyses, and PostView³¹ was used to determine contact area and contact stresses for each subject and loading scenario.

6.3.4 Contact Areas and Stresses

Contact area was calculated on the articulating surface of the acetabular cartilage as an absolute value and as a percentage of the total surface area. Peak and average contact stresses within the contact area on the acetabular cartilage were calculated for all subjects and loading scenarios. Average values of contact stress were mapped to a template mesh representing the acetabular cartilage. The radius and surface area of the template mesh were chosen to match the mean values for the group of subjects.

6.3.5 Statistical Analysis

The acetabular cartilage was divided into anterior, superior and posterior regions.³² The nonparametric Kruskal-Wallis analysis of variance was used to test for significant differences in mean pressure between regions for each activity, and for differences between activities for each region. Posthoc comparisons were performed using the Dunn test. Significance was set at $p \leq 0.05$. Data are presented as mean \pm SD unless noted.

6.4 Results

6.4.1 Contact Stress Distribution and Contact Area

Contact stresses were highly nonuniform, and there was more variability in contact stress between subjects for a given activity than between activities for a single subject (Fig. 6.2). Quantitatively, the standard deviation of peak contact stresses for a single subject (across all activities) was usually less than half of the standard deviation for any activity (across all subjects). For example, the standard deviation of peak contact

stresses for subject #2 (across all activities) was 0.55 MPa, whereas the standard deviation of peak contact stress for the walking heel-strike activity (across all subjects) was 2.11 MPa. Differences in bone and cartilage geometry strongly affected the variation in contact patterns and location of peak contact stresses between the subjects. As an example, the acetabulum of one subject exhibited a small cavity in the anterior-superior roof of the acetabulum, causing a discontinuity in the contact stresses on the articular surface (Fig. 6.3). Despite the variability between subjects, the differences in contact between activities roughly followed the change in the direction of the resultant joint reaction force. Specifically, as the direction of loading changed from predominantly superior-posterior during ascending stairs to more superior during walking and superior-anterior during descending stairs, the locations of contact moved similarly. Similar shifting was seen within the stages of walking, although to a lesser extent.

Although the location of contact was different between activities, the magnitudes of the average contact areas on the acetabular cartilage were similar during each activity. The total acetabular cartilage surface area averaged $1,936 \pm 295 \text{ mm}^2$, while the average area in contact across all activities was $657 \pm 43 \text{ mm}^2$ (Fig. 6.4). There was no significant difference in absolute contact area ($p=0.593$) or percent contact area ($p=0.486$) between activities.

6.4.2 Peak and Average Contact Stresses

The location of the peak stress tended to be similar for a particular subject across all activities (Fig. 6.2). The magnitude of the peak stresses slightly increased as the joint reaction force increased between activities. For instance, the peak stress was 7.52 ± 2.11

MPa for WHS (233% BW) and increased to 8.53 ± 2.61 and 8.66 ± 3.01 MPa for AHS (252% BW) and DHS (261% BW). Peak stresses for the other activities were 7.22 ± 2.32 , 7.16 ± 2.62 , 7.15 ± 2.54 and 7.11 ± 2.50 MPa for WHM, WMD, WML, and WLS, respectively.

Average contact stresses were on the order of 1 MPa for all activities. Specifically, average contact stresses for WHS, WHM, WMD, WML, WLS, AHS, and DHS were 1.08 ± 0.32 , 0.99 ± 0.27 , 0.94 ± 0.24 , 0.94 ± 0.23 , 0.93 ± 0.21 , 1.18 ± 0.27 and 1.23 ± 0.32 MPa, respectively.

6.4.3 Regional Differences in Average Contact Stresses

There were significant differences in the average contact stress between regions for most activities (Fig. 6.5). For instance, differences were detected between the superior and posterior regions during WHS ($p=0.04$). When the joint force was oriented more anteriorly during WHM, there were significant regional differences in contact stress between the anterior and posterior regions ($p=0.04$) and between the superior and posterior regions ($p=0.01$). This trend continued through the remaining walking stages, including WLS ($p=0.004$ and $p=0.006$ for anterior versus posterior and superior versus posterior, respectively). There were no significant differences in contact stress between the different regions during AHS. However, contact stress in both the anterior and superior regions was significantly greater than those of the posterior region during DHS ($p=0.004$ and $p=0.02$, respectively).

For a given region, there were no significant differences in average stresses between any of the walking scenarios, with the exception of the posterior region, which

saw a significant increase in stresses between WHS and WLS ($p=0.04$).

6.5 Discussion

The objective of this study was to quantify the magnitude and distribution of cartilage contact stress in a well-defined group of healthy hips using a validated modeling protocol. The major findings were that cartilage contact stress distribution varies considerably even among healthy subjects, but there were consistent trends in the magnitude and area of contact stresses. Further, contact patterns changed significantly between loading activities. Despite the fact that subjects were selected using clinically-based criteria for normal, healthy hips, contact stress distribution was nonuniform in all cases, with greater variation between subjects than between loading scenarios (Fig. 6.2). This suggests that even in the healthy population, cartilage contact mechanics are unique to the individual. It is postulated that the variability in contact mechanics is due to small differences in bone and cartilage morphology, an example of which is illustrated in Figure 6.3. This conclusion is based upon the fact that identical boundary and loading conditions were applied to each model, leaving geometry as the primary variable between subjects.

The nonuniform distribution of contact stress predicted in this study is supported by prior studies examining the effect of geometric assumptions on a computational model, as well as prior in vitro studies. A previous computational study investigated how contact stresses were altered when femoral and acetabular geometry were changed from subject-specific to an ideal sphere.³³ Models with ideal geometry had substantially reduced cartilage contact stresses and more uniform distributions of contact.

Furthermore, for spherical models, the magnitude and distribution of contact stresses did not appreciably change between loading scenarios, in contrast to the results of the current study. Most computational studies that have used subject-specific geometry presented only proof-of-concept results, wherein only a single model was developed.^{17,34} One exception is a study that modeled contact pressures using the asymptomatic hips of 5 patients with acetabular dysplasia and CT images from 1 cadaver.³⁵ Only contact distributions for the cadaver-based model were described in detail, and the distributions were more uniform than those of the current study. The differences may be due to the fact that the CT images in the previous study were collected from hip joints that were already in contact. The added congruency due to initial contact, along with considerable smoothing during segmentation, may have resulted in more uniform contact during modeling. Still, the range of peak contact pressures (4.53 to 7.05 MPa) in asymptomatic hips of the previous study reached the lower end of those observed in the current study. Multiple in vitro experiments have reported that cartilage contact stresses are irregular in the normal hip joint.^{8,10,14,20,36-38} In a study of hip joint congruity, considerable variation was found in the magnitude and joint space width.³⁹ Likewise, another study found that incongruity strongly affected the distribution of contact and pressure, although there was no correlation between distribution of contact and subchondral bone density.³⁸ This suggests that, in agreement with current results, surface geometry is the major determinant of cartilage contact stress distribution and magnitude.

While there was substantial variation in the spatial distribution of contact stress between subjects, peak and average contact stresses as well as contact areas were similar for each loading scenario. The magnitude of peak contact stress averaged between 7 and

8 MPa for all activities. This was despite a 58% bodyweight difference in applied joint contact forces between the highest and lowest loading activities. These data suggest that although different hips distribute load differently, healthy joints distribute load in a way that maintains a fairly homeostatic maximum contact stress. Average contact stresses (~ 1 MPa) were considerably less than peak values, in agreement with other studies.^{14,36} Direct comparison of values for contact stress with prior experimental studies is difficult because of differences in loading modalities and measurement techniques. At midstance (203% BW load, 1.1° flexion, 8.4° abduction, 6.7° internal rotation), we predicted a peak stress of 7.16 ± 2.62 MPa. This is in good agreement with values ranging from 6.72 to 8.80 MPa found in vitro with joints in similar orientations.^{10,14,36} In fact, the range of peak contact stresses predicted in the present study corroborates many published values.^{8,38}

Even though the orientation of the femur and pelvis were changed to represent different loading scenarios, contact areas were consistent at 32% to 37% of the articulating surface area. This suggests that despite variations in the distribution of stresses, healthy hips maintain a similar percentage of the cartilage surface in contact during different activities. These interactivity similarities may be explained by specific morphologies of the acetabulum consistently being in contact with the articulating femoral head. Two previous studies varied the orientation of the femur with respect to the acetabulum and found little effect on the pattern of contact stress.^{10,36} However, one of these studies did report a general shift in loading as orientation changed, in agreement with the current study.³⁶

While there was considerable variation in the distribution of contact stress between subjects, some patterns were evident. There was a shift in the spatial distribution of contact stress in correspondence with changing loading directions. The acetabular regions that experienced the highest load support depended on the particular loading scenario (Fig. 6.4). For example, the cartilage on the anterior acetabulum supported more load than the superior region during DHS, whereas the superior region supported more load than the anterior region during AHS. These patterns indicate significant shifts in load bearing throughout the joint during different activities.

There are several limitations of this study that warrant discussion. First, cartilage was assumed to be isotropic, nearly incompressible, and hyperelastic. While cartilage is known to exhibit biphasic behavior, computational predictions of stress have been shown to be equivalent for biphasic and incompressible hyperelastic material models during instantaneous loading.⁴⁰ Also, the constitutive assumptions in this study are consistent with an experimentally validated protocol.²⁰ Furthermore, despite the material homogeneity used in this study, there are substantial differences in the predicted stress distributions between subjects. This implies that the differences are due to the geometric variation in joint geometry between subjects. Second, the FE models did not include the acetabular labrum. The role of the labrum during load distribution has been debated.^{41,42} A recent study found that the labrum supported less than 3% of the total load across the joint in healthy control subjects.⁴³ Since CT image data were segmented semi-automatically, there may be some observer-dependence in the resulting segmentations. The accuracy of the segmentation protocols has been evaluated for both bone and cartilage and found to produce errors less than 0.5 mm.^{25,26} With respect to this amount

of error and its effect on contact stresses, it is important to note that local changes in geometry are not likely to occur in a 0.5 mm distance along the articulating surface. In other words, errors in segmentation are consistent and vary smoothly on a given surface. Thus, the subtle geometric differences suspected to cause individual contact stress magnitudes and distributions generally occur along the curvature of that surface over distances greater than 0.5 mm. Finally, joint angles and contact forces used to drive the models were taken from the literature.¹¹ Using generic values for specific models may have one of two effects: application of generic joint angles and forces could cause more uniformity in contact stress between subjects, or it could exacerbate the effects of individual geometry as the joints are loaded at what may not be the optimal orientations to effectively redistribute contact forces. Nevertheless, boundary conditions were applied in the model to circumvent this effect (i.e., femur was allowed to translate in axial plane to find path of least resistance).

The use of subject-specific geometry in a population of healthy individuals revealed considerable variation in distributions of contact stress and some similarities that can be expected in normal human hips. The results presented herein can be used as a basis for comparing pathologic and healthy hips in the future.

6.6 Acknowledgments

Financial support from NIH R01AR053344 and R01GM083925 is gratefully acknowledged. The authors thank R. Kent Sanders, MD for interpreting the CT arthrograms.

6.7 References

1. Mavcic B, Pompe B, Antolic V, et al. 2002. Mathematical estimation of stress distribution in normal and dysplastic human hips. *J Orthop Res* 20:1025-1030.
2. Bombelli R. 1983. Osteoarthritis of the hip: Classification and pathogenesis. Springer-Verlag, Berlin and New York.
3. Jessel RH, Zurakowski D, Zilkens C, et al. 2009. Radiographic and patient factors associated with pre-radiographic osteoarthritis in hip dysplasia. *The Journal of bone and joint surgery* 91:1120-1129.
4. Harris WH. 1986. Etiology of osteoarthritis of the hip. *Clinical orthopaedics and related research*:20-33.
5. Bardakos NV, Villar RN. 2009. Predictors of progression of osteoarthritis in femoroacetabular impingement: A radiological study with a minimum of ten years follow-up. *J Bone Joint Surg Br* 91:162-169.
6. Beck M, Kalhor M, Leunig M, Ganz R. 2005. Hip morphology influences the pattern of damage to the acetabular cartilage: Femoroacetabular impingement as a cause of early osteoarthritis of the hip. *J Bone Joint Surg Br* 87:1012-1018.
7. Ganz R, Parvizi J, Beck M, et al. 2003. Femoroacetabular impingement: A cause for osteoarthritis of the hip. *Clinical orthopaedics and related research*:112-120.
8. Afoke NY, Byers PD, Hutton WC. 1987. Contact pressures in the human hip joint. *J Bone Joint Surg Br* 69:536-541.
9. Sparks DR, Beason DP, Etheridge BS, et al. 2005. Contact pressures in the flexed hip joint during lateral trochanteric loading. *J Orthop Res* 23:359-366.
10. von Eisenhart-Rothe R AC, Steinlechner M, Muller-Gerbl M and Eckstein F. 1999. Quantitative determination of joint incongruity and pressure distribution during simulated gait and cartilage thickness in the human hip joint. *J Orthop Res* 7:532-539.
11. Bergmann G. 1998. Hip98: Data collection of hip joint loading on cd-rom. Free University and Humboldt University, Berlin.
12. Bergmann G, Deuretzbacher G, Heller M, et al. 2001. Hip contact forces and gait patterns from routine activities. *J Biomech* 34:859-871.

13. Carlson CE, Mann RW, Harris WH. 1974. A radio telemetry device for monitoring cartilage surface pressures in the human hip. *IEEE Trans Biomed Eng* 21:257-264.
14. Hodge WA, Fijan RS, Carlson KL, et al. 1986. Contact pressures in the human hip joint measured in vivo. *Proc Natl Acad Sci U S A* 83:2879-2883.
15. Genda E, Iwasaki N, Li G, et al. 2001. Normal hip joint contact pressure distribution in single-leg standing--effect of gender and anatomic parameters. *J Biomech* 34:895-905.
16. Yoshida H, Faust A, Wilckens J, et al. 2006. Three-dimensional dynamic hip contact area and pressure distribution during activities of daily living. *J Biomech* 39:1996-2004.
17. Bachtar F, Chen X, Hisada T. 2006. Finite element contact analysis of the hip joint. *Med Biol Eng Comput* 44:643-651.
18. Brown TD, DiGioia AM, 3rd. 1984. A contact-coupled finite element analysis of the natural adult hip. *J Biomech* 17:437-448.
19. Rappoport DJ, Carter DR, Schurman DJ. 1985. Contact finite element stress analysis of the hip joint. *J Orthop Res* 3:435-446.
20. Anderson AE, Ellis BJ, Maas SA, et al. 2008. Validation of finite element predictions of cartilage contact pressure in the human hip joint. *J Biomech Eng* 130:051008.
21. Anderson LA, Peters CL, Park BB, et al. 2009. Acetabular cartilage delamination in femoroacetabular impingement. Risk factors and magnetic resonance imaging diagnosis. *The Journal of bone and joint surgery* 91:305-313.
22. Wiberg G. 1939. Studies on dysplastic acetabula and congenital subluxation of the hip joint. *Acta Chir Scand.* 83 28-38.
23. Clohisy JC, Carlisle JC, Beaulé PE, et al. 2008. A systematic approach to the plain radiographic evaluation of the young adult hip. *The Journal of bone and joint surgery* 90 Suppl 4:47-66.
24. Tonnies D. 1987. *Congenital dysplasia and dislocation of the hip* Springer Verlag, Berlin.
25. Anderson AE, Ellis BJ, Peters CL, Weiss JA. 2008. Cartilage thickness: Factors influencing multidetector ct measurements in a phantom study. *Radiology* 246:133-141.

26. Allen BC, Peters CL, Brown NA, Anderson AE. 2010. Acetabular cartilage thickness: Accuracy of three-dimensional reconstructions from multidetector ct arthrograms in a cadaver study. *Radiology* 255:544-552.
27. Anderson AE, Peters CL, Tuttle BD, Weiss JA. 2005. Subject-specific finite element model of the pelvis: Development, validation and sensitivity studies. *J Biomech Eng* 127:364-373.
28. Puso MA, Maker, Bradley N., Ferencz, Robert M., Hallquist, John O. 2007. Nike3d: A nonlinear, implicit, three-dimensional finite element code for solid and structural mechanics. User's Manual.
29. Caligaris M, Ateshian GA. 2008. Effects of sustained interstitial fluid pressurization under migrating contact area, and boundary lubrication by synovial fluid, on cartilage friction. *Osteoarthritis Cartilage* 16:1220-1227.
30. Maas S, Rawlins D, Weiss J. 2010. "Preview" finite element pre-processing. In. Salt Lake City: Musculoskeletal Research Laboratories.
31. Maas S, Rawlins D, Weiss J. 2010. "Postview" finite element post processing. In. Salt Lake City: Musculoskeletal Research Laboratories.
32. Athanasiou KA, Agarwal A, Dzida FJ. 1994. Comparative study of the intrinsic mechanical properties of the human acetabular and femoral head cartilage. *J Orthop Res* 12:340-349.
33. Anderson AE, Ellis BJ, Maas SA, Weiss JA. 2010. Effects of idealized joint geometry on finite element predictions of cartilage contact stresses in the hip. *J Biomech* 43:1351-1357.
34. Lutz A, Fietz K, Nackenhorst U. 2009. Simulation of the physiological contact pressure distribution in the human hip joint. *Proc App Math and Mech* 9:149-150.
35. Russell ME, Shivanna KH, Grosland NM, Pedersen DR. 2006. Cartilage contact pressure elevations in dysplastic hips: A chronic overload model. *J Orthop Surg Res* 1:6.
36. Brown TD, Shaw DT. 1983. In vitro contact stress distributions in the natural human hip. *J Biomech* 16:373-384.
37. Rushfeldt PD, Mann RW, Harris WH. 1981. Improved techniques for measuring in vitro the geometry and pressure distribution in the human acetabulum. In instrumented endoprosthesis measurement of articular surface pressure distribution. *J Biomech* 14:315-323.

38. von Eisenhart-Rothe R, Eckstein F, Muller-Gerbl M, et al. 1997. Direct comparison of contact areas, contact stress and subchondral mineralization in human hip joint specimens. *Anat Embryol (Berl)* 195:279-288.
39. Eckstein F, von Eisenhart-Rothe R, Landgraf J, et al. 1997. Quantitative analysis of incongruity, contact areas and cartilage thickness in the human hip joint. *Acta Anat (Basel)* 158:192-204.
40. Ateshian GA, Ellis BJ, Weiss JA. 2007. Equivalence between short-time biphasic and incompressible elastic material responses. *J Biomech Eng* 129:405-412.
41. Ferguson SJ, Bryant JT, Ganz R, Ito K. 2003. An in vitro investigation of the acetabular labral seal in hip joint mechanics. *J Biomech* 36:171-178.
42. Konrath GA, Hamel AJ, Olson SA, et al. 1998. The role of the acetabular labrum and the transverse acetabular ligament in load transmission in the hip. *The Journal of bone and joint surgery* 80:1781-1788.
43. Henak CR, Ellis BJ, Harris MD, et al. 2011. Role of the acetabular labrum in load support across the hip joint. *J Biomech* 44:2201-2206.

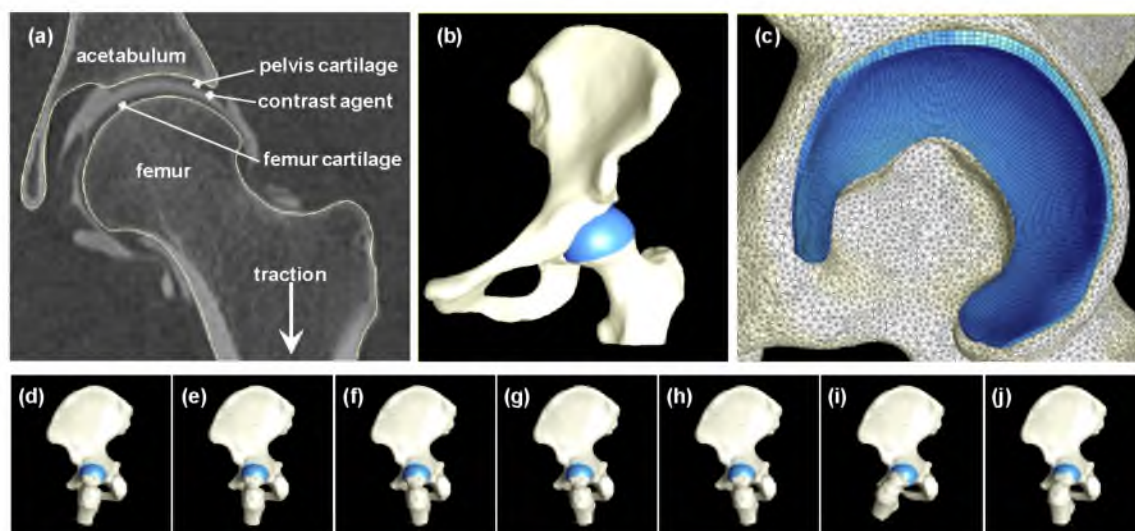


Figure 6.1. FE model creation and simulated loading scenarios. (a) CT section through center of proximal femur with contrast agent between opposing acetabular and femoral cartilage. Segmentation lines follow the contour of the pelvis and femur bone morphology. (b) Three-dimensional reconstruction of cortical bone (off-white) and articular cartilage (blue). (c) Lateral view of the FE model at the acetabulum shows triangular shell and hexahedral elements representing cortical bone and cartilage, respectively (d-j). Orientation of femur and pelvis during simulated activities captured from an identical view of the yz-plane; with respect to these images, displacements were centered in the joint and directed vertically. From left to right: WHS, WHM, WMD, WML, WLS, AHS, and DHS.

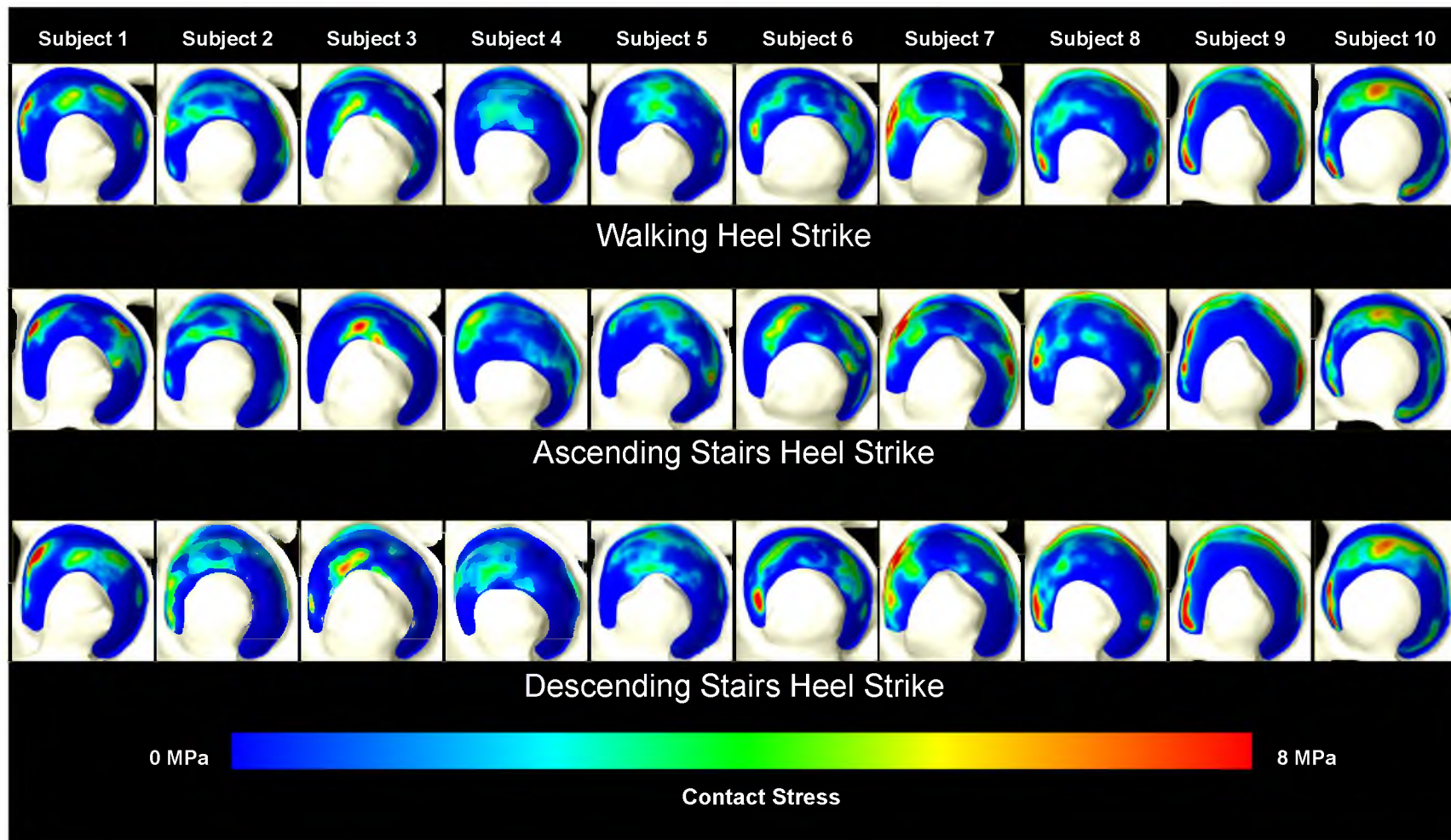


Figure 6.2. Contact stresses on the acetabular cartilage for each subject during walking, ascending stairs and descending stairs. Left is anterior. Variations in the stresses were greater between subjects (columns) than between loading scenarios (rows).

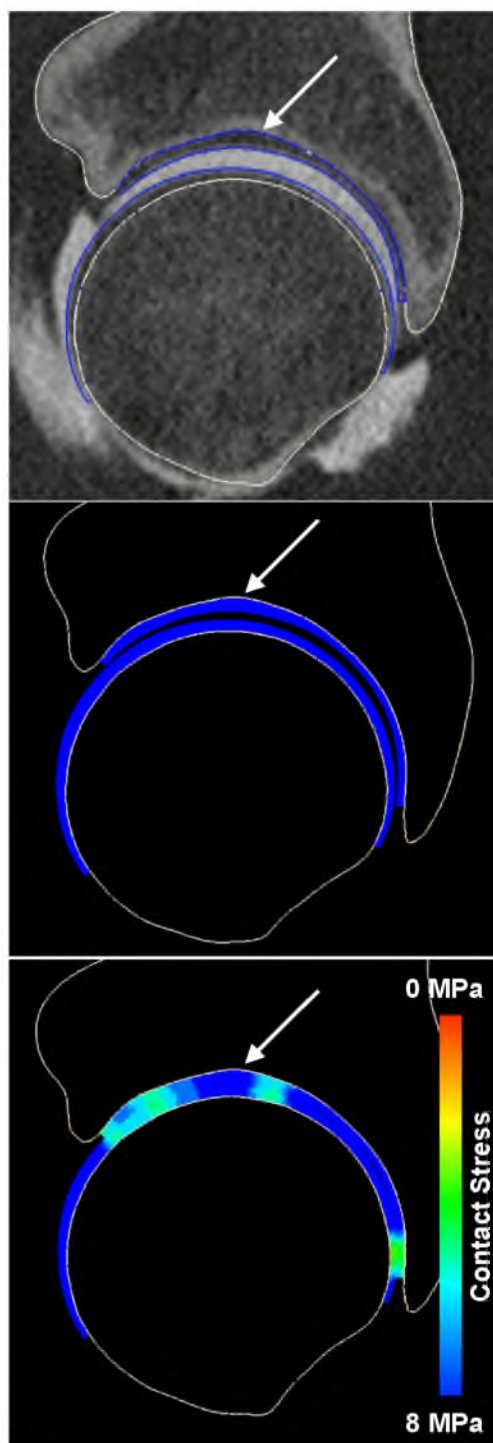


Figure 6.3. CT image and model predictions of cartilage contact stress for 1 subject, illustrating the effects of bony geometry. The small cavity located in the superior roof of the acetabulum (arrow, top panel) created a depression that is identifiable in the model before loading (arrow, middle panel) and when loaded (arrow, bottom panel). This resulted in an area of relatively low contact stress at the corresponding location of contact.

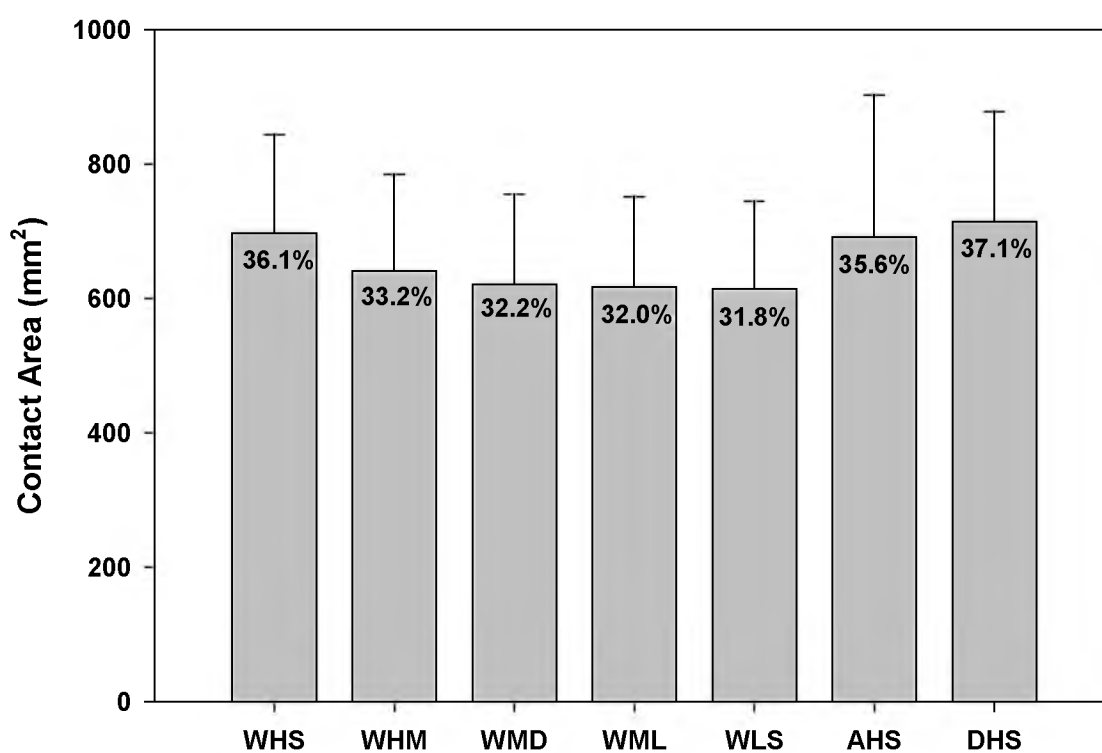


Figure 6.4. Contact area on the articulating surface of the acetabular cartilage as a function of activity. Percentages represent the portion of the total articulating surface in contact.

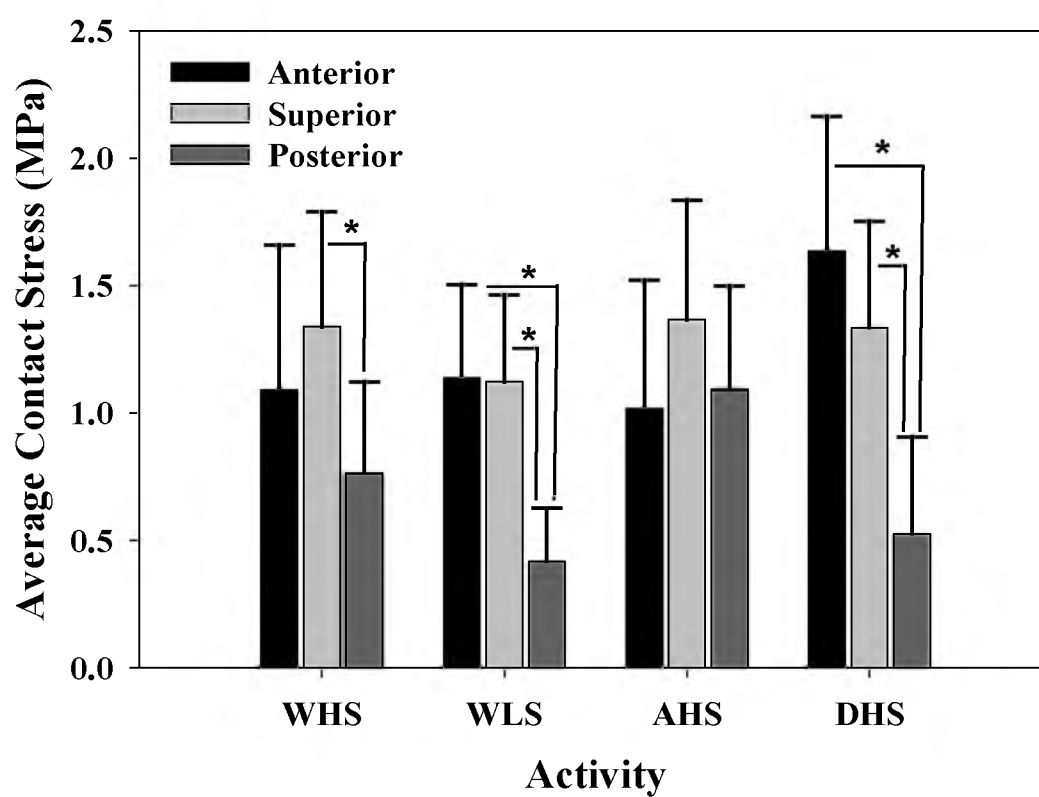


Figure 6.5. Average contact stress as a function of region and activity. There were significant differences (shown with asterisk) between at least two regions for every activity, except AHS.

CHAPTER 7

JOINT ANGLES, MOMENTS, MUSCLE FORCES, AND REACTION FORCES IN NORMAL AND DYSPLASTIC HIPS

7.1 Abstract

Orthopaedists focus on bony abnormalities and cartilage damage when evaluating the severity of acetabular dysplasia. Alterations to lower limb gait and hip muscle mechanics are rarely quantified, but may be of clinical importance by providing insight into the origins of pain and predisposition to osteoarthritis. The objectives of this study were to assess the feasibility of using an available musculoskeletal model to estimate muscle and joint forces at the hip and to compare hip joint kinematics and muscle forces between healthy control subjects and patients with acetabular dysplasia. The modeling process was validated by comparing model-based muscle activations to in vivo electromyographical (EMG) signals for a healthy subject. Validation was also accomplished by comparing hip and knee joint angles and moments for the single subject to data reported in the literature for healthy subjects. Next, force generation from muscles spanning the hip, as well as joint reaction forces at the hip were compared between 7 control subjects and 7 patients with acetabular dysplasia. Model-based estimations of activations compared well with EMG for most muscles. Joint kinematics

and moments were also consistent with data from the literature. Few statistical significant differences existed between controls and dysplastic patients, but these data could still have clinical implications. With refinement, the modeling strategies of the current study demonstrate potential to improve the diagnosis and treatment of acetabular dysplasia.

7.2 Introduction

Anatomical pathologies of the hip, such as acetabular dysplasia are a common cause of hip pain in the young adult.^{1,2} The shallow acetabulum of dysplastic hips fails to adequately cover and stabilize the femoral head, which can alter loading within the joint.³⁻⁵ Altered loading is thought to then cause tears and fraying of the acetabulum and focal cartilage lesions, which may predispose dysplasia patients to osteoarthritis.⁶⁻⁸ Some patients experience acute pain that results from traumatic labral tears.¹ However, for most dysplasia patients pain is insidious, beginning as a minor irritation and becoming progressively more painful with time. Pain tends to originate in the buttock, groin, or lateral aspect of the hip and can be accompanied with mechanical symptoms such as catching, clicking, popping, and locking of the hip.^{1,9}

Diagnosis of acetabular dysplasia often focuses on radiographic and magnetic resonance (MR) evidence of abnormal geometry and/or labral tears.^{2,10,11} Radiographic angles such as the lateral center edge angle (LCEA) are used to determine the shallowness of the acetabulum.^{12,13} Radiographs can also be used to detect sclerotic changes to the acetabular rim or femoral head that may be indicative of abnormal loading

and early OA.^{14,15} MR images can be used to observe biological changes to the labrum and articular cartilage as damage occurs within the joint.¹⁶

Current clinical evaluation of acetabular dysplasia is not focused on understanding the mechanics of hip musculature in dysplasia patients. Understandably, focus is upon correction of abnormal bony anatomy, which cannot be corrected with therapy or other nonsurgical methods.^{17,18} However, acetabular dysplasia is likely a complex pathomechanical disease that involves not only bony and soft-tissue damage within the joint, but also alterations to the musculature and ligaments surrounding the joint.¹⁹ For example, altered muscle forces may explain pain patients experience in the groin or buttocks. Likewise, in response to altered joint anatomy, patients may adapt their motion during activities of daily living to reduce pain or improve feelings of stability.

Only a few studies have reported the kinematics and kinetics of patients with acetabular dysplasia during different activities. These studies have focused on joint angles and moments in dysplastic hips compared to the presumed healthy contralateral limb²⁰, a control group^{20,21}, or before and after corrective surgery.²²⁻²⁵ Results from these studies suggest that patients with acetabular dysplasia indeed have altered hip joint angles and moments. However, there is no indication from these studies what, if any, muscular differences may be associated with these alterations.

The lack of data about possible muscular differences between control subjects and dysplastic patients may be due to the inability to measure muscle forces in vivo. To this end, musculoskeletal models may be applied to estimate muscle activations, muscle forces, and cumulative joint reaction forces.²⁶ To do so, muscle models based on experimentally derived mechanical and geometric muscle features (e.g., maximum

isometric force, pennation angles, tendon slack lengths, etc.) are coupled with gait or other motion data collected in vivo.^{27,28} Assuming, a musculoskeletal model can be shown to feasibly predict muscle activation and force, observed differences in joint kinematics and kinetics may be interpreted in light of any differences noted in the muscle forces.

The purpose of this study was to assess the feasibility of using a musculoskeletal model to estimate muscle and joint forces at the hip and to couple traditional gait analysis with musculoskeletal modeling to determine if differences in hip joint kinematics and muscle forces existed between healthy control subjects and patients with acetabular dysplasia.

7.3 Methods

7.3.1 Data Collection and Processing (Feasibility Study)

Gait data were collected for a single female control volunteer. First, retro-reflective spherical markers were placed at bony landmarks of the pelvis, lower limbs, C7 vertebrae, and the clavicles.²⁹ Additional markers were placed so at least 3 markers were on the pelvis, femurs, shanks, and feet, making a total of 21 markers. The subject then walked barefoot at a self-selected speed across a 10 meter runway. Three-dimensional marker trajectories were recorded using 10 near-infrared Vicon cameras (Vicon Motion Systems; Oxford, UK) at a capture rate of 100 Hz. Ground reaction forces were simultaneously recorded at a rate of 1000 Hz using 4 AMTI forceplates concealed within the runway (Advanced Mechanical Technology Inc., Watertown, MA).

Electromyography (EMG) data of muscle activations were collected using a 10-channel Motion Lab Systems system (Motion Lab Systems, Inc. Baton Rouge, LA). The electrode-skin interface was cleared of hair and prepped with alcohol pads to reduce impedance and 5 surface electrode pairs were placed on each leg. Specifically, electrodes were placed over the gluteus maximus, rectus femoris, hamstrings, proximal anterior tibialis, and gastrocnemius muscles. EMG signals were recorded simultaneously with gait data at a sampling rate of 1000 Hz.

Video and analog data were all captured using Vicon Nexus software (v1.7) then imported into Visual 3D software (v 4.96; C-Motion Inc., Germantown, MD) for processing. Residual analysis was performed on marker and ground reaction force data to determine filtering cutoff frequencies that sufficiently eliminated noise without undue elimination of true signal.³⁰ Low-pass Butterworth filters were then applied to the marker and ground reaction force data using cutoff frequencies of 6 Hz and 20 Hz, respectively. Foot strike and foot off events were identified, from which speed and stride length were calculated for each subject.

A high-pass filter with cutoff frequency of 20 Hz³¹ and a root mean square window was passed over the data with a window size of 51 frames, which corresponded to a ~10 Hz low-pass-filter.^{32,33} EMG signals were then rectified and normalized to their respective maxima. Finally, filtered marker, ground reaction force, and EMG data were exported from Visual 3D and converted using Matlab (r2010; MathWorks Inc., Natick, MA) to a format conducive to importation into the musculoskeletal modeling program, OpenSim.²⁸

7.3.2 Musculoskeletal Modeling (Feasibility Study)

In OpenSim, a virtual marker set matching the experimental markers was placed on a 23 degree-of-freedom (DOF), 96 actuator (80 muscles) model of the lower limbs, pelvis, torso, and head (Fig. 7.1). The model was derived from a 23-DOF, 92 actuator model that has been used previously.^{32,34-36} For the current study, rectus abdominus and obturator externus muscles were added based a model by Shelburne et al.³⁷⁻³⁹

The generic model was scaled to fit the live subject using anthropometrics recorded during gait collection and spatial relationships between virtual and experimental markers. Next, joint angles were calculated using an inverse kinematics (IK) tool which minimized the error between experimental marker trajectories and virtual markers on the model. Specifically, at each frame the model was placed in a pose in which virtual markers best matched experimental marker coordinates based on a weighted least squares problem that minimized the distance between experimental marker coordinates and corresponding virtual markers, subject to joint constraints.⁴⁰ Greater weights were assigned to markers on prominent bony landmarks that were the least susceptible to skin and soft-tissue motion and subject-to-subject positional variation. Flexion, adduction, and rotation angles were calculated at the hip joint; flexion angles were also calculated at the knees and ankles. An inverse dynamics tool was used to calculate net joint moments from the joint kinematics and ground reaction forces.³⁰

To minimize dynamic inconsistencies between ground reaction forces, joint moments and model kinematics that result from experimental factors (e.g., skin motion, noise), joint angle data (e.g., accelerations derived by differentiating angles), and modeling assumptions (e.g., inaccuracies in model geometry and mass distribution), a

residual reduction algorithm (RRA) was used.²⁸ Briefly, RRA allowed for minor adjustments to the location of the torso center of mass, the mass of each individual segment, and the joint angles and translations calculated with inverse kinematics, to reduce residuals that result from inequalities between the external force applied to the subject (i.e., ground reaction force) and the cumulative force exerted by the body (calculated as the summed mass of each segment times their translational accelerations).

Static optimization was used to calculate the muscle forces needed to reproduce joint moments during a full gait cycle. Briefly, static optimization extended the inverse dynamics solution to resolve net joint moments into individual muscle contributions by minimizing the sum of squared muscle activations. Although dynamic optimization tools are available that may incorporate more of the time-dependent behavior of muscles, static optimization has been found to be appropriate for studies of normal gait, as in the current study.^{41,42}

Finally, joint reaction forces (JRF) were calculated at the hip using an analysis tool in OpenSim.³² The joint reaction analysis tool reported the vector components of the summed contributions of all motion and forces in the model, including muscle and ground forces.

7.3.3 Modeling Control Subjects and Dysplastic Patients

Gait data were collected from 7 patients (5 female, 2 male) diagnosed with acetabular dysplasia with IRB approval (IRB #10983) and informed consent. All patients had LCEA angles less than 20°, which is clinically indicative of a dysplastic

acetabulum.^{10,13} Patients also presented at the clinic with pain and, after collection of gait data, were treated with or scheduled for a corrective peri-acetabular osteotomy.

Seven control subjects (5 female, 2 male) were also recruited as part of a larger study (IRB #10983). The control subjects had no history of hip pain or dysfunction and were radiographically confirmed to not have signs of dysplasia.

Gait data were collected for each subject. A representative trial was identified during which the subjects stepped on the forceplates in a sequence that provided ground reaction force and marker data that met the necessary requirements stipulated for OpenSim models of the lower limb. Joint angles, moments, and muscle forces were estimated for a complete gait cycle as describe above. Analyses were performed on the affected side of the patients and a randomly chosen side of the controls.

7.3.4 Analysis

Normalized EMG signals were qualitatively compared to muscle activation estimations from the OpenSim models. From the first female volunteer, a total of 7 gait cycles (foot strike to ipsilateral foot strike) from 7 different trials were compared. Muscle activations from OpenSim are reported on a scale from 0 to 1, with 1 representing maximum activation. Therefore, the EMG signals were normalized on a 0 to 1 scale. Residual forces during static optimization were reported as a percent of body weight during the modeled gait cycles.

Average and standard deviation pelvis angles (tilt/list/rotation), hip joint angles (flexion/adduction/rotation), hip joint moments (flexion/adduction/rotation), knee joint angles (flexion), and knee moments (flexion) were calculated for the control and

dysplastic subjects across a full gait cycle. Angles were calculated in degrees; moments were divided by body mass for each individual. Time points during gait of average angle and moment maxima and minima were identified. Then, maxima and minima for each subject near those time points were isolated, averaged, and compared between groups using a Students t-test. An exception was made with respect to pelvic tilt, which had little variance during the entire gait cycle and no obvious maximum or minimum. Instead, pelvic tilt angles were average across the gait cycle for each subject; these averaged values were tested for significance between groups.

Resultant JRFs were calculated at the hip for each subject and normalized to bodyweight (xBW). Maximum JRFs during early and late stance were tested for statistical significance between control and patient groups. Forces from the 21 muscles spanning the hip (represented by 33 actuators) were tested for significant differences between groups with a t-test at the times during early and late stance (~15% and ~50% of the gait cycle, respectively), when JRF maxima occurred for each individual. Significance for all tests was set at $p \leq 0.05$.

7.4 Results

7.4.1 Feasibility and Validation

Average and standard deviation residual forces and moments for the 7 trials of the feasibility model are shown in Figure 7.2. Using RRA, residual forces were reduced to less than 0.05 xBW. Similarly, residual moments were reduced to 0.4 Nm/kg. Kinematic differences between IK and RRA were unappreciable (not shown), indicating that RRA did not substantially change joint angles or segment translations.

Qualitative agreement between EMG signals and model-based muscle activations appeared excellent for the hamstrings and gastrocnemius, good for the gluteus maximus, fair for the rectus femoris, and poor for the anterior tibialis (Fig. 7.3).

7.4.2 Demographics, Joint Angles, and Moments

The average age, weight, and height of the controls and (patients) were 25 ± 4 (26 ± 8) years, 71.4 ± 21.8 (66.7 ± 14.8) kg, and 1.73 ± 0.09 (1.70 ± 0.08) meters, respectively. Average and standard deviation speeds were 1.19 ± 0.11 m/s for controls and 1.13 ± 0.13 m/s for patients, and were not significantly different between groups ($p = 0.5$). Stride lengths, normalized to subject height, were 0.75 ± 0.69 and 0.72 ± 0.04 for controls and patients, respectively, and were not significantly different ($p = 0.4$).

Patients had more posterior pelvic tilt than controls, but the difference was not statistically significant ($p = 0.12$) (Fig. 7.4). Patients had a reduced pelvic list toward the contralateral side during early stance and less external rotation throughout gait, compared to controls. However, maximum and minimum pelvic list and rotation angles were not statistically significant between groups ($p \geq 0.06$).

Hip flexion range of motion was decreased for patients, but again, differences at local maxima and minima were not significantly different than those of controls ($p \geq 0.09$). Likewise, average adduction and rotation angles indicated reduced range of motion in the patients, but not to the point of statistical significance (Fig 7.5). Significance was found at minimum adduction moment points, during which patients produced less of a negative adduction (i.e., abduction) moment ($p = 0.03$ for min1, 0.002

for min2). Minimum external rotation moments were also significantly less for patients ($p = 0.01$) in mid- to late stance (~40% gait) (Fig. 7.5).

Knee flexion angles were not significantly different between groups, but the knee flexion moment for the patients was significantly reduced during late stance ($p = 0.009$) (Fig. 7.6).

7.4.3 Joint Reaction and Muscle Forces

Resultant hip JRFs manifested a peak in early stance (~15% gait) during the initial loading response, and a second peak during late stance (~50% gait) (Fig. 7.7). Average JRFs for controls at the first peak were 3.56 ± 0.54 xBW, and were significantly greater than the 2.92 ± 0.34 xBW experienced by the dysplastic hips ($p = 0.02$). At the second JRF peak, controls' JRFs were 3.91 ± 0.41 xBW compared to 3.71 ± 0.63 xBW for patients, and were not significantly different ($p = 0.5$).

Average and standard deviation hip muscle forces at the two JRF peaks are shown in Table 7.1. Gluteus medius was the major contributor to the first peak JRF, with support also from gluteus maximus, gluteus minimus, semimembranosus, the long head of biceps femoris, and gemellus. Rectus femoris generated 0.09 to 0.12 xBW of force at the first JRF peak, although contributions were likely more toward knee extension. All other muscles made only minor contributions (0.06 xBW or less) to the first JRF peak. Major contributions to the second JRF peak came from gluteus medius, psoas, iliacus, rectus femoris, and gluteus minimus. Iliacus and psoas generated more force in control subjects than in patients, whereas rectus femoris generated more force in the patients. Rectus femoris force differences were not statistically significant, although $p = 0.06$ at

the second peak. Statistically significant differences were found only for gluteus minimus and tensor fasciae latae ($p = 0.03$ and 0.01 , respectively). Forces from contributing muscles during an entire gait cycle are shown for a representative control and dysplastic patient in Figure 7.8.

7.5 Discussion

The objectives of this study were to assess the feasibility of using an available musculoskeletal model to estimate muscle and joint forces at the hip and to compare hip joint kinematics and muscle forces between healthy control subjects and those with acetabular dysplasia. Dynamic consistency between joint angles and translation with ground reaction forces and moments was established with only very minor residual forces, using the residual reduction algorithm. Estimations of activations, forces, joint angles and moments compared well with EMG for most muscles and with literature reports of hip kinematics. There were few statistical differences between controls and dysplastic patients, but differences that did exist may have important clinical implications, as discussed below.

It is not possible to eliminate experimental or modeling errors that occur during data collection or construction of a musculoskeletal model. As a result, when performing simulations of gait, residual forces and moments exist to establish dynamic consistency between the model coordinates (joint angles and translations), ground reaction forces and moments. If these residuals are left unbounded, their contribution to the model can be very high, leaving estimations of forces for other actuators (i.e., muscles) lower than may be realistic. Use of RRA in the current study reduced contributions of peak residual

forces and moments to ~ 0.04 xBW and 0.4 Nm/kg, respectively. Averaged across the entire gait cycle, residuals were nearly zero and had only minor contributions to overall model forces. Consequently, estimations of muscle and joint reaction forces at the hip were largely unaffected by residual forces. Also, use of RRA was not at the expense of large changes to model kinematics, as joint angles from IK were not appreciably different from joint angles post-RRA.

OpenSim-based estimations of muscle activations showed qualitative agreement with EMG signals for most of the muscles measured. Specifically, agreement was good with respect to timing and magnitude for the hamstrings, gastrocnemius, and gluteus maximus muscles. Activation of the rectus femoris seemed to be underestimated in early stance (through $\sim 30\%$ gait) and again during swing (after $\sim 60\%$ gait). The lack of rectus femoris activation in the model may be due to simplification of the degrees of freedom for the knee joint (i.e., flexion only). The major functions of the rectus femoris are hip flexion and knee extension, but it also likely serves to stabilize knee rotation in more than the sagittal plane, which would lead to more *in vivo* firing than was predicted by the simplified model. Alternatively, there may have been cross-talk in the EMG signal from other quadriceps muscles, which would have exaggerated the duration and amplitude of EMG-based rectus femoris activation.

Model-based and EMG activation differences were greatest for the anterior tibialis. The cause of this may have been simplification of the ankle and foot as well as geometric representation of the anterior tibialis and the tibia. Common marker schemes for the foot, including that of this study, place markers at the heel and toe.²⁹ Thus, the entire foot is considered to be a rigid body and flexion at the forefoot is not captured.

While forefoot flexion is likely minor in healthy adults, it may contribute to activation of the anterior tibialis, which could explain differences between activations in the model and those recorded with EMG. Redefinition of the muscle path of the anterior tibialis and the bony geometry of the tibia may also improve agreement between EMG and model activation.⁴³ Regardless, the major role of the anterior tibialis is flexion of the foot during swing, so underestimation of its activation was unlikely to have a strong impact on predicted forces at the hip.

Kinematics and kinetics, as calculated with OpenSim, were in agreement with literature reports for control subjects. Specifically, speed and stride length, as well as pelvis, knee and hip angles fell within ranges previously reported for healthy individuals.^{35,44-46} These results provide confidence for the marker weights and inverse kinematics optimization used, as well as the selection of this cohort as representative healthy adult subjects. Muscle force magnitudes can be found primarily from other modeling studies, as muscle forces cannot be measured *in vivo*. For muscles spanning the hip, forces in the current study were comparable to estimates from other models, for the gluteus maximus, gluteus medius, gluteus minimus^{26,47} and rectus femoris.⁴⁶ Iliacus and psoas were major contributors to hip joint reaction forces in late stance when the subjects were moving to push off the foot and flex the hip. Few studies have reported iliacus and psoas forces, which may be due to the difficulty in obtaining EMG signals for these deep muscles. However, the large forces from iliacus and psoas, in the range of 1 xBW agree with data presented by Pandy and Andriacchi.²⁶

Finally, hip joint reaction forces for control subjects peaked during the loading response after heel strike at approximately 3.5 xBW and during late stance at 3.9 xBW.

These estimations fall within the upper range of JRFs determined in vivo with telemeterized implants, which generally have peaks from 2.5 to 4.0 xBW during gait.^{48,49} Although higher than in vivo reports, JRFs from the current study compare well with previous modeling studies.⁵⁰⁻⁵² One explanation for differences in forces between telemeterized implants and model-derived estimates may be with regards to the type of subjects for which data was collected and processed. For instance, subjects studied by Bergmann et al. ranged in age from 50 to 71 years and received a total hip arthroplasty for treatment of end-stage OA with a telemeterized implant.⁵³ It is likely that the musculature of older subjects with end-stage OA had weakened and may not generate forces to the same level of younger subjects. Likewise, implantation inherently disrupts and may weaken the musculature. As a whole, it is understandable that JRFs for the older population with end-stage OA would be less than younger subjects who are still active.

When control subjects were compared to the dysplastic patients, few statistically significant differences were found. A number of factors may explain the lack of differences between groups, including the setup of the forceplates in this study, the activity examined (normal walking), and limitations to the model.

The modeling procedure in OpenSim currently requires ground reaction forces of approximately 0.5 to 0.75 xBW from the contralateral limb, prior to modeling a gait cycle for the limb of interest. These forces stabilize the model during initialization of RRA and static optimization. However, meeting these requirements can be a challenge with a limited number of force plates and restrictions to the size of the capture volume. Forceplate layout in the current study allowed subject trials to be modeled only if they hit

a specific forceplate sequence, which may have resulted in similar step lengths for controls and patients during the trials that could be modeled. In turn, this could have led to joint angles for each group that were more similar than if trials could be captured without forceplate restriction.

Very recently, an instrumented treadmill was purchased using NIH grant funding and installed in the University of Utah Motion Capture Core Facility. The instrumented treadmill has separate forceplates and treads for each foot. The setup allows continuous capture of ground reaction forces. With continuous and controlled gait speed, the subject can find a natural stride length. The instrumented treadmill would alleviate issues related to the setup of the forceplates in the current study, and, in the future, could help to elucidate subtle differences in gait patterns between subject groups.

Patients with dysplasia may not demonstrate atypical gait when walking, which may also explain the lack of differences in kinematics and muscle forces between subject groups in this study. Normal walking is an energy efficient activity where the hip is not rotated into extreme ranges of motion. Patients in our study mentioned that they did not fatigue when walking short walking distances, such as those captured in the current study. Further, patients knew they were being observed during gait data collection and may have tried to conceal any discomfort and consciously maintain a normal appearing gait. Future studies should collect kinematic data during motions that may be more difficult to perform for patients with dysplasia, such as squatting, jogging, or climbing stairs; these activities are more likely to alter muscle activations and forces in patients with dysplasia.

Although there were few statistical differences between controls and patients during gait, those that were detected may be clinically meaningful. First, patients had more posterior pelvis tilt than controls throughout the gait cycle. The difference in pelvic tilt was enough evident during data collection that markers on the pelvis of patients were routinely double checked for correct placement. The posterior rotation of the pelvis by dysplastic patients may be a subconscious compensatory mechanism to shift their center of mass and stabilize the joint during walking. If so, this would be a difficult adjustment to consciously correct during observation and is likely a true artifact of the dysplastic hip.

More posterior tilt may have also contributed to the higher rectus femoris forces and knee moments in patients. Although not statistically different between groups, average muscle forces of the rectus femoris were 0.25 xBW greater in patients compared to controls. Rectus femoris originates just above the acetabulum at the anterior inferior iliac spine and the ilium and spans not only the hip but also the knee, and plays a major role in bending at each joint.⁵⁴ The effect of increased posterior pelvic tilt across the long trajectory of rectus femoris could reasonably cause an increase in required muscle force contribution to hip flexion and knee extension. Increased rectus femoris forces may then have lessened the required contributions from iliacus and psoas, which tended to be lower in patients than in controls during late stance. It is possible that increased rectus femoris forces contribute to clinically noted avulsions of that muscle concomitant with labral tears, and is worthy to pursue in future studies.⁵⁵

Statistical differences did exist at the first JRF peak, where controls experienced JRFs that were significantly higher than those of the patients. The greater JRFs in controls did not correspond to higher forces from any single muscle. Instead, there was a

general, distributed decrease in hip muscle forces in the patient group. Because dysplasia patients may have become accustomed to feelings of joint instability and discomfort, and despite efforts to maintain a normal gait, they may adapt their gait to yield a slightly lower ground reaction force than normal. The reduced hip flexion just before and at foot strike in the patient group supports a possible reduction in ground reaction force to reduce instability.

Finally, results suggested possible hip abductor weakness or avoidance in the patients compared to the control subjects. This was evidenced by reduced adduction and external rotation moments at the hip and statistically significant reductions in tensor fasciae latae and gluteus minimus forces at the second JRF peak. One study has reported tensor fasciae latae weakness in a group of subjects with pathologic hip anatomy (i.e., patients with femoroacetabular impingement) and the same may hold true for the anatomical alterations seen in acetabular dysplasia patients.⁵⁶ Regardless, if dysplastic patients do have weak abductors, this may be an important consideration when planning periacetabular osteotomy surgery to correct global deficiency in coverage, as some techniques have been associated with prolonged abductor weakness.⁵⁷ Further weakening of already weak muscle groups following surgery could make recovery challenging for patients and may endanger their ability to recoup muscle function.

Some of the limitations of this study have already been discussed, but a general limitation of this type of musculoskeletal modeling deserves further attention. The modeling techniques used in this study can only identify muscle force differences secondary to differences in movement patterns between controls and patients. Also, because the joint is represented as an ideal ball and socket joint, it does not represent the

true geometry of dysplastic patients and cannot estimate more subtle mechanical differences that result from geometric abnormalities. For example the shallow acetabulum of the dysplastic joint may lateralize the center of rotation and change moment arms of the surrounding muscles.⁵⁸ Also, the center of rotation may not be stationary within the hip, especially in the aspherical joints of dysplastic patients. Prior theoretical work has shown that changes to hip geometry affect predictions of joint forces.⁵⁹ Thus, muscle force estimations using this musculoskeletal model are likely good estimates of general force distribution and summed joint reaction forces, but there may be subtle differences in joint loading due to abnormal geometry that cannot be detected. Work is underway to incorporate subject-specific geometry into OpenSim models and determine the sensitivity of models to changes bony geometry, muscle paths, and definition of the hip joint center (see NIH R21AR063844).⁶⁰

A final limitation of note is the inherent difficulty in capturing precise hip joint motion with skin markers. Although skin markers are the most common tool used during gait analysis, they do have recognized errors due to skin motion over underlying bone, and the presence of soft-tissue that prohibits markers from being placed directly on bony landmarks.⁶¹ Capturing subtle hip motion differences can be especially challenging at the hip because the joint is deep within the thigh, where marker errors can cause errors in definition of the hip joint to be as high as 30 mm.⁶² Therefore, skin marker errors may have obscured differences between the control and dysplastic groups in the current study. In the aforementioned NIH R21, 3D dual fluoroscopy will be used to measure in vivo hip joint kinematics with submillimeter accuracy. These kinematics may yield differences in muscle forces between groups.^{62,63}

Results from this preliminary study of kinematics and muscle forces in control subjects and patients with acetabular dysplasia are promising. The applied model is feasible for the study of gait and similar activities and has demonstrated the ability to detect differences between healthy and pathomorphologic conditions. Future use of subject-specific kinematics and inclusion of subject-specific geometry may improve model predictions, which may better delineate subtle differences between groups. Activities that are difficult for dysplasia patients should be examined. Further tests of model feasibility may be completed by applying muscle activations using the current techniques to drive forward dynamic simulations and verify that resulting kinematics match those originally collected in the laboratory.⁶⁴ In conclusion, with refinement, the modeling strategies of the current study could improve our biomechanical understanding of this multifaceted pathology.

7.6 Acknowledgments

This project was supported by the National Institutes of Health R01AR05344, R24HD06569 and the National Center for Simulation in Rehabilitation Research.

7.7 References

1. Nunley RM, Prather H, Hunt D, et al. 2011. Clinical presentation of symptomatic acetabular dysplasia in skeletally mature patients. *J Bone Joint Surg Am* 93 Suppl 2:17-21.
2. Peters CL, Erickson J. 2006. The etiology and treatment of hip pain in the young adult. *J Bone Joint Surg Am* 88 Suppl 4:20-26.
3. Cooperman DR, Wallensten R, Stulberg SD. 1983. Acetabular dysplasia in the adult. *Clin Orthop Relat Res*:79-85.

4. Dezateux C, Rosendahl K. 2007. Developmental dysplasia of the hip. *Lancet* 369:1541-1552.
5. Russell ME, Shivanna KH, Grosland NM, Pedersen DR. 2006. Cartilage contact pressure elevations in dysplastic hips: A chronic overload model. *J Orthop Surg Res* 1:6.
6. Guevara CJ, Pietrobon R, Carothers JT, et al. 2006. Comprehensive morphologic evaluation of the hip in patients with symptomatic labral tear. *Clin Orthop Relat Res* 453:277-285.
7. Leunig M, Podeszwa D, Beck M, et al. 2004. Magnetic resonance arthrography of labral disorders in hips with dysplasia and impingement. *Clin Orthop Relat Res*:74-80.
8. Reijman M, Hazes JM, Pols HA, et al. 2005. Acetabular dysplasia predicts incident osteoarthritis of the hip: The rotterdam study. *Arthritis Rheum* 52:787-793.
9. Birrell F, Silman A, Croft P, et al. 2003. Syndrome of symptomatic adult acetabular dysplasia (saad syndrome). *Ann Rheum Dis* 62:356-358.
10. Clohisy JC, Carlisle JC, Beaule PE, et al. 2008. A systematic approach to the plain radiographic evaluation of the young adult hip. *J Bone Joint Surg Am* 90 Suppl 4:47-66.
11. Jessel RH, Zurakowski D, Zilkens C, et al. 2009. Radiographic and patient factors associated with pre-radiographic osteoarthritis in hip dysplasia. *J Bone Joint Surg Am* 91:1120-1129.
12. Wiberg G. 1939. Studies on dysplastic acetabula and congenital subluxation of the hip joint. *Acta Chir Scand*. 83 28-38.
13. Delaunay S, Dussault RG, Kaplan PA, Alford BA. 1997. Radiographic measurements of dysplastic adult hips. *Skeletal Radiol* 26:75-81.
14. Su P, Li R, Liu S, et al. 2008. Age at onset-dependent presentations of premature hip osteoarthritis, avascular necrosis of the femoral head, or legg-calve-perthes disease in a single family, consequent upon a p.Gly1170ser mutation of col2a1. *Arthritis Rheum* 58:1701-1706.
15. Hasegawa Y, Iwata H, Mizuno M, et al. 1992. The natural course of osteoarthritis of the hip due to subluxation or acetabular dysplasia. *Arch Orthop Trauma Surg* 111:187-191.

16. Stelzeneder D, Mamisch TC, Kress I, et al. 2012. Patterns of joint damage seen on mri in early hip osteoarthritis due to structural hip deformities. *Osteoarthritis Cartilage* 20:661-669.
17. Sanchez-Sotelo J, Trousdale RT, Berry DJ, Cabanela ME. 2002. Surgical treatment of developmental dysplasia of the hip in adults: I. Nonarthroplasty options. *J Am Acad Orthop Surg* 10:321-333.
18. Clohisy JC, Barrett SE, Gordon JE, et al. 2006. Periacetabular osteotomy in the treatment of severe acetabular dysplasia. Surgical technique. *J Bone Joint Surg Am* 88 Suppl 1 Pt 1:65-83.
19. Babst D, Steppacher SD, Ganz R, et al. 2011. The iliocapsularis muscle: An important stabilizer in the dysplastic hip. *Clin Orthop Relat Res* 469:1728-1734.
20. Romano CL, Frigo C, Randelli G, Pedotti A. 1996. Analysis of the gait of adults who had residua of congenital dysplasia of the hip. *J Bone Joint Surg Am* 78:1468-1479.
21. Pedersen EN, Simonsen EB, Alkjaer T, Soballe K. 2004. Walking pattern in adults with congenital hip dysplasia: 14 women examined by inverse dynamics. *Acta Orthop Scand* 75:2-9.
22. Pedersen EN, Alkjaer T, Soballe K, Simonsen EB. 2006. Walking pattern in 9 women with hip dysplasia 18 months after periacetabular osteotomy. *Acta Orthop* 77:203-208.
23. Karam MD, Gao Y, McKinley T. 2011. Assessment of walking pattern pre and post peri-acetabular osteotomy. *Iowa Orthop J* 31:83-89.
24. Endo H, Mitani S, Senda M, et al. 2003. Three-dimensional gait analysis of adults with hip dysplasia after rotational acetabular osteotomy. *J Orthop Sci* 8:762-771.
25. Sucato DJ, Tulchin K, Shrader MW, et al. 2010. Gait, hip strength and functional outcomes after a ganz periacetabular osteotomy for adolescent hip dysplasia. *J Pediatr Orthop* 30:344-350.
26. Pandy MG, Andriacchi TP. 2010. Muscle and joint function in human locomotion. *Annu Rev Biomed Eng* 12:401-433.
27. Pandy MG. 2001. Computer modeling and simulation of human movement. *Annu Rev Biomed Eng* 3:245-273.
28. Delp SL, Anderson FC, Arnold AS, et al. 2007. Opensim: Open-source software to create and analyze dynamic simulations of movement. *IEEE Trans Biomed Eng* 54:1940-1950.

29. Davis RB. 1991. A gait analysis data collection and reduction technique. *Human Movement Science* 10:575-587.
30. Winter D. 2004. *Biomechanics and motor control of human movement*. Wiley.
31. De Luca CJ, Gilmore LD, Kuznetsov M, Roy SH. 2010. Filtering the surface emg signal: Movement artifact and baseline noise contamination. *J Biomech* 43:1573-1579.
32. Steele KM, Demers MS, Schwartz MH, Delp SL. 2012. Compressive tibiofemoral force during crouch gait. *Gait Posture* 35:556-560.
33. Heintz S, Gutierrez-Farewik EM. 2007. Static optimization of muscle forces during gait in comparison to emg-to-force processing approach. *Gait Posture* 26:279-288.
34. Delp SL, Loan JP, Hoy MG, et al. 1990. An interactive graphics-based model of the lower extremity to study orthopaedic surgical procedures. *IEEE Trans Biomed Eng* 37:757-767.
35. Liu MQ, Anderson FC, Schwartz MH, Delp SL. 2008. Muscle contributions to support and progression over a range of walking speeds. *J Biomech* 41:3243-3252.
36. Au C. 2013. Gait 2392 and 2354 models. In: Hicks, J. editor.
37. Shelburne KB, Decker MJ, Krong J, et al. 2010. Muscle forces at the hip during squatting exercise. In, 56th Annual Meeting of the Orthopaedic Research Society. New Orleans, LA, p. poster 1927.
38. Jorgensen MJ, Marras WS, Granata KP, Waiand JW. 2001. MRI-derived moment-arms of the female and male spine loading muscles. *Clin Biomech (Bristol, Avon)* 16:182-193.
39. Marras WS, Jorgensen MJ, Granata KP, Waiand B. 2001. Female and male trunk geometry: Size and prediction of the spine loading trunk muscles derived from MRI. *Clin Biomech (Bristol, Avon)* 16:38-46.
40. Lu TW, O'Connor JJ. 1999. Bone position estimation from skin marker coordinates using global optimisation with joint constraints. *J Biomech* 32:129-134.
41. Anderson FC, Pandy MG. 2001. Dynamic optimization of human walking. *J Biomech Eng* 123:381-390.

42. Anderson FC, Pandy MG. 2001. Static and dynamic optimization solutions for gait are practically equivalent. *J Biomech* 34:153-161.
43. Arnold EM, Ward SR, Lieber RL, Delp SL. 2010. A model of the lower limb for analysis of human movement. *Ann Biomed Eng* 38:269-279.
44. Ostrosky KM, VanSwearingen JM, Burdett RG, Gee Z. 1994. A comparison of gait characteristics in young and old subjects. *Phys Ther* 74:637-644; discussion 644-636.
45. Oberg T, Karsznia A, Oberg K. 1994. Joint angle parameters in gait: Reference data for normal subjects, 10-79 years of age. *J Rehabil Res Dev* 31:199-213.
46. Xiao M, Higginson J. 2010. Sensitivity of estimated muscle force in forward simulation of normal walking. *J Appl Biomech* 26:142-149.
47. Crossley KM, Dorn TW, Ozturk H, et al. 2012. Altered hip muscle forces during gait in people with patellofemoral osteoarthritis. *Osteoarthritis Cartilage* 20:1243-1249.
48. Bergmann G, Deuretzbacher G, Heller M, et al. 2001. Hip contact forces and gait patterns from routine activities. *J Biomech* 34:859-871.
49. Graichen F. 2013. Orthoload: Loading of orthopaedic implants. In: Bergmann, G. editor. Berlin: Julius Wolff Institute.
50. Correa TA, Crossley KM, Kim HJ, Pandy MG. 2010. Contributions of individual muscles to hip joint contact force in normal walking. *J Biomech* 43:1618-1622.
51. Lewis CL, Sahrman SA, Moran DW. 2010. Effect of hip angle on anterior hip joint force during gait. *Gait Posture* 32:603-607.
52. Fraysse F, Dumas R, Cheze L, Wang X. 2009. Comparison of global and joint-to-joint methods for estimating the hip joint load and the muscle forces during walking. *J Biomech* 42:2357-2362.
53. Bergmann G, Graichen F, Rohlmann A. 1993. Hip joint loading during walking and running, measured in two patients. *J Biomech* 26:969-990.
54. Morton D, Albertine K, Foreman B. 2011. The big picture: Gross anatomy. McGraw Hill, New York.
55. Hosalkar HS, Pennock AT, Zaps D, et al. 2012. The hip antero-superior labral tear with avulsion of rectus femoris (halter) lesion: Does the slap equivalent in the hip exist? *Hip Int* 22:391-396.

56. Casartelli NC, Maffiuletti NA, Item-Glatthorn JF, et al. 2011. Hip muscle weakness in patients with symptomatic femoroacetabular impingement. *Osteoarthritis Cartilage* 19:816-821.
57. Pogliacomi F, Stark A, Vailanti E, Wallensten R. 2003. Periacetabular osteotomy of the hip: The ilioinguinal approach. *Acta Biomed* 74:38-46.
58. Delp SL, Maloney W. 1993. Effects of hip center location on the moment-generating capacity of the muscles. *J Biomech* 26:485-499.
59. Lenaerts G, De Groote F, Demeulenaere B, et al. 2008. Subject-specific hip geometry affects predicted hip joint contact forces during gait. *J Biomech* 41:1243-1252.
60. Valente G, Martelli S, Taddei F, et al. 2012. Muscle discretization affects the loading transferred to bones in lower-limb musculoskeletal models. *Proc Inst Mech Eng H* 226:161-169.
61. Fuller J, Liu LJ, Murphy MC, Mann RW. 1997. A comparison of lower-extremity skeletal kinematics measured using skin- and pin-mounted markers. *Hum Mov Sci* 16:219-242.
62. Stagni R, Fantozzi S, Cappello A, Leardini A. 2005. Quantification of soft tissue artefact in motion analysis by combining 3d fluoroscopy and stereophotogrammetry: A study on two subjects. *Clin Biomech (Bristol, Avon)* 20:320-329.
63. Li K, Zheng L, Tashman S, Zhang X. 2012. The inaccuracy of surface-measured model-derived tibiofemoral kinematics. *J Biomech* 45:2719-2723.
64. Buchanan TS, Lloyd DG, Manal K, Besier TF. 2004. Neuromusculoskeletal modeling: Estimation of muscle forces and joint moments and movements from measurements of neural command. *J Appl Biomech* 20:367-395.

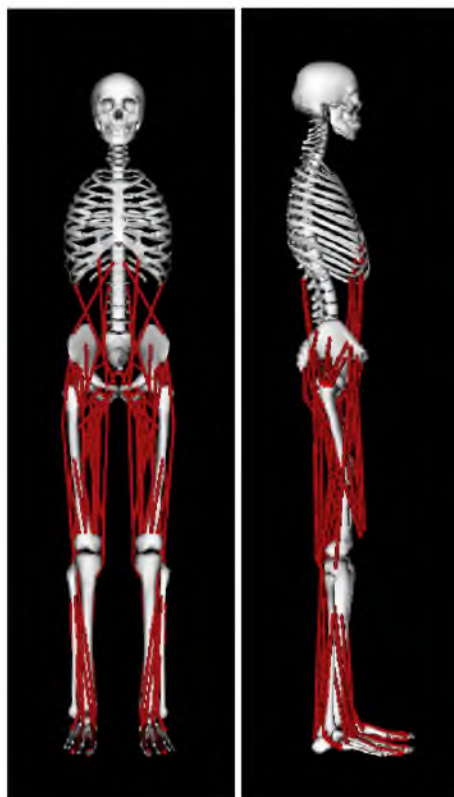


Figure 7.1 Frontal and sagittal view of unscaled OpenSim musculoskeletal model. Model used in the current study had 23 degrees of freedom and 96 muscle actuators.

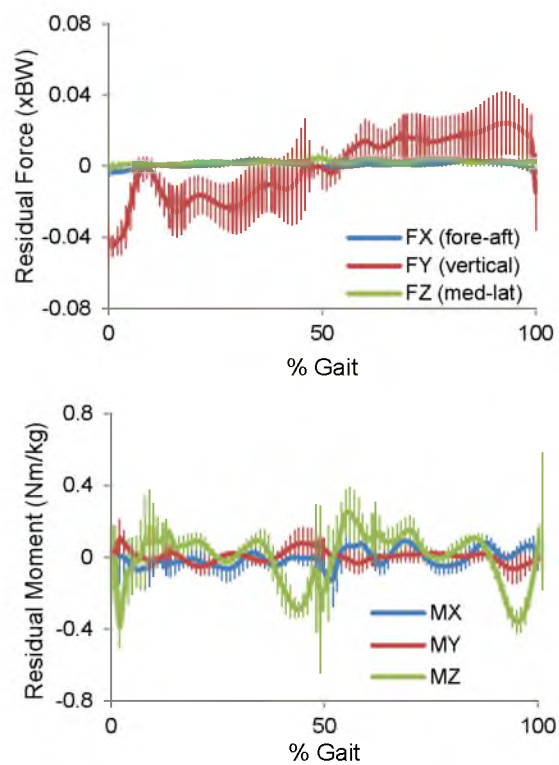


Figure 7.2. Residual forces and moments, after RRA, averaged across 7 trials for 1 subject. Vertical bars are standard deviations.

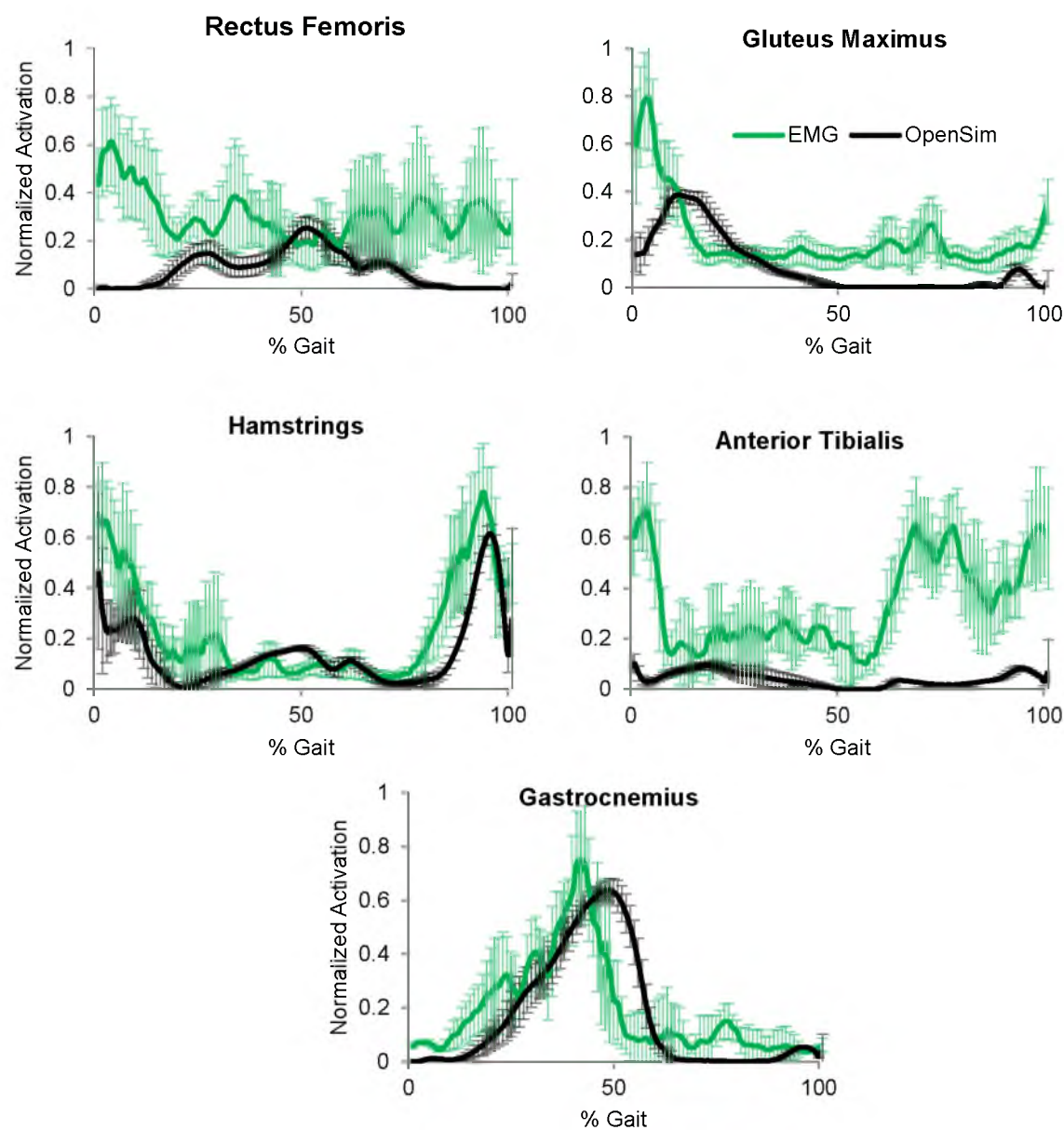


Figure 7.3. Rectified and normalized EMG signals (green) compared to OpenSim predictions of muscle activations (black). EMG and OpenSim signals were averaged across 7 trials; vertical bars show standard deviations.

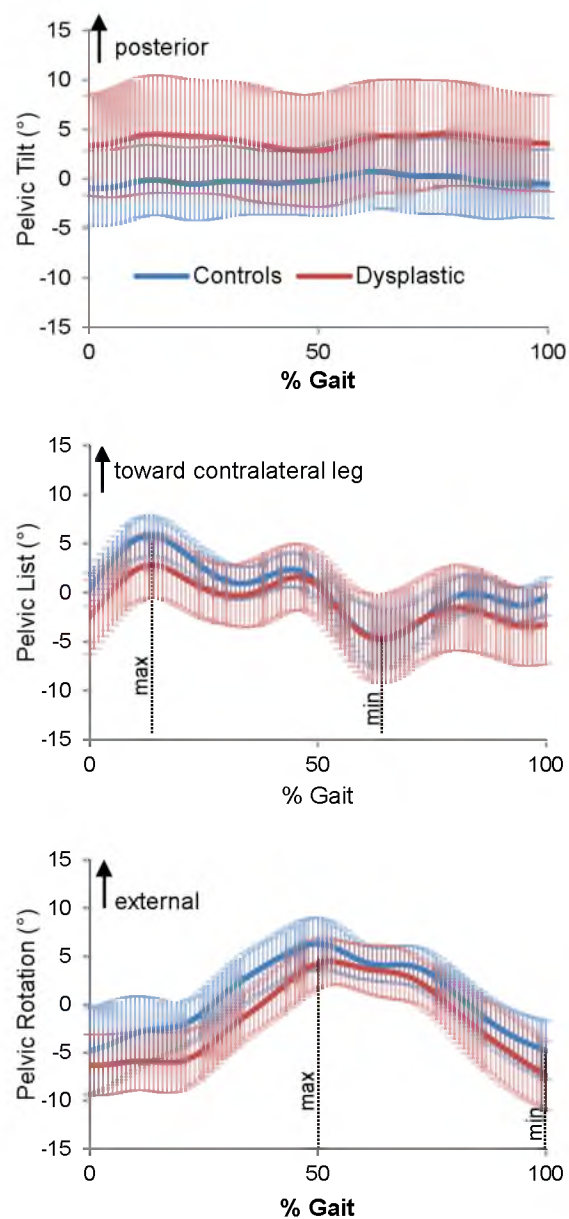


Figure 7.4. Average pelvis angles for control and dysplastic subjects. Dotted vertical lines show approximate maxima and minima used for statistical comparisons.

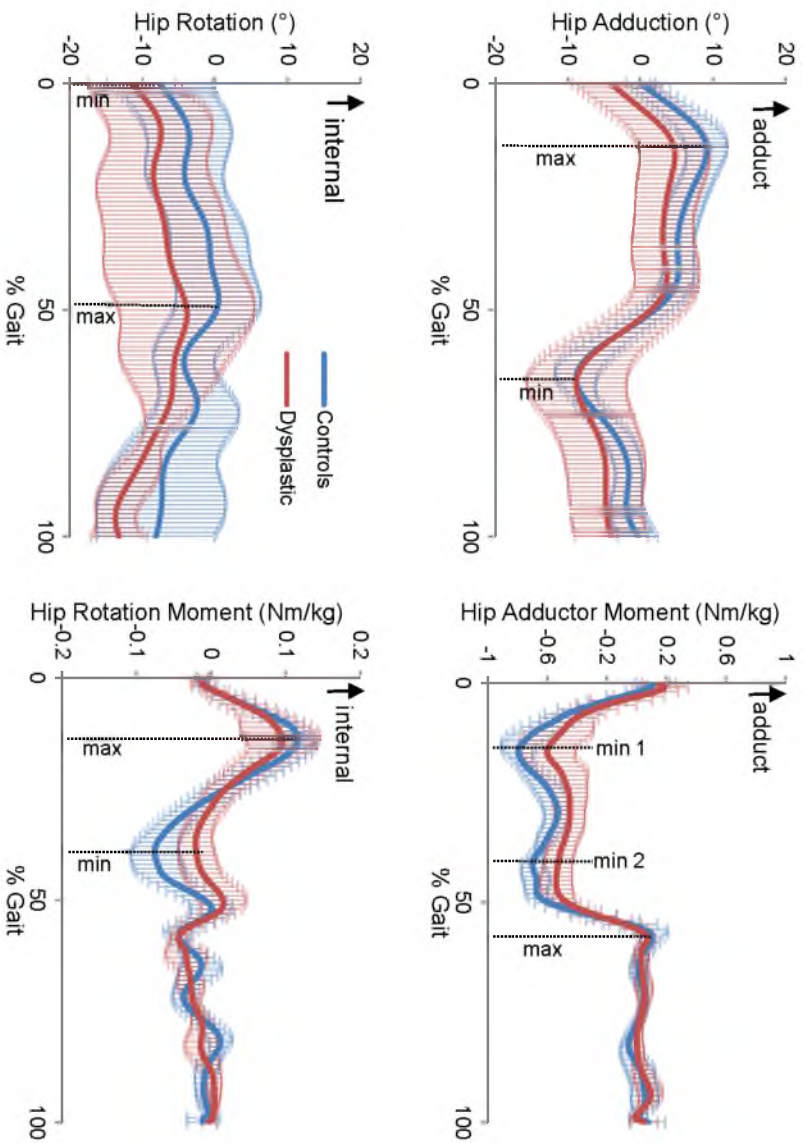
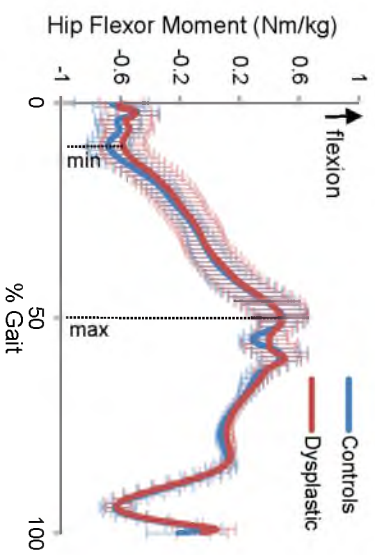
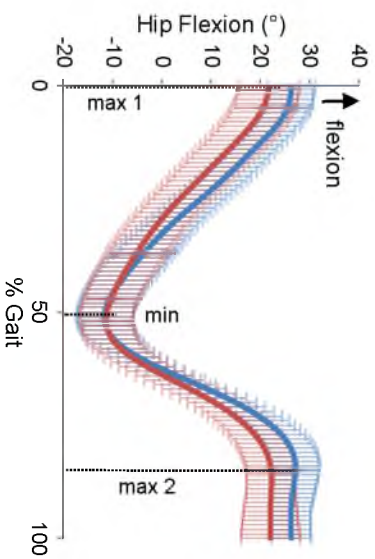


Figure 7.5. Average hip angles and moments for controls and dysplastic patients.



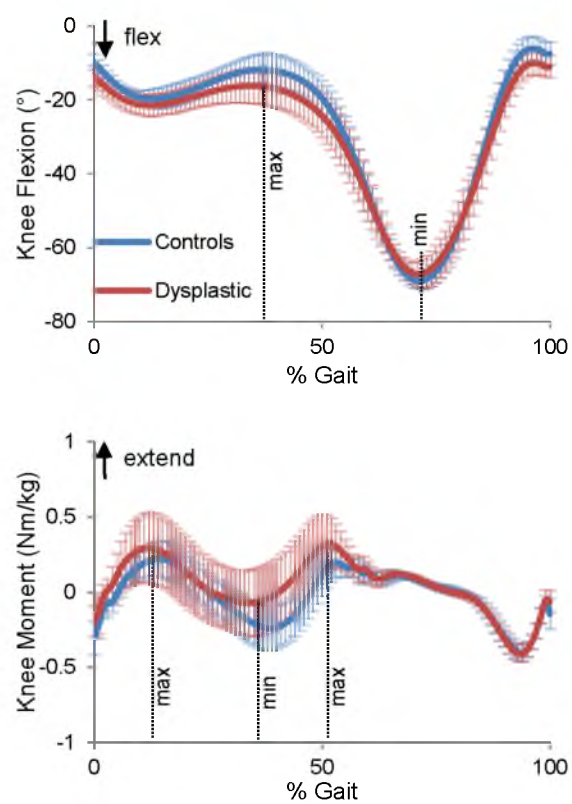


Figure 7.6. Knee flexion angles and moments for control and dysplastic subjects.

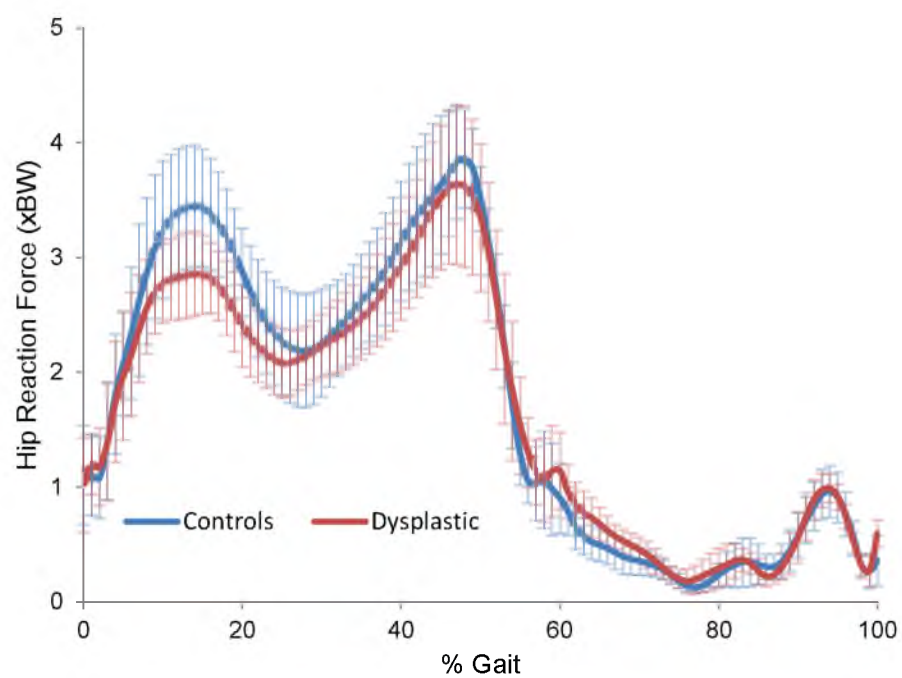


Figure 7.7. Average joint reaction forces at the hip for control and dysplastic subjects. Vertical bars indicate standard deviations.

Table 7.1 Average \pm standard deviation forces generated by muscles spanning the hip during peaks JRF times. Function abbreviations: abd = abduct thigh, add = adduct thigh, ext = extend thigh, flex = flex thigh, inrot = internally rotate thigh, exrot = externally rotate thigh. Functions shown in order of strength of contribution to a given movement. Forces are xBW. Significance differences ($p \leq 0.05$) are shaded.

Muscle	Function	JRF Peak 1		JRF Peak 2	
		Controls	Patients	Controls	Patients
Tensor fasciae latae	abd/flex	0.06 \pm 0.04	0.05 \pm 0.05	0.11 \pm 0.02	0.08 \pm 0.02
Gluteus medius	abd/inrot/ flex/ exrot/ext	1.46 \pm 0.32	1.20 \pm 0.33	1.04 \pm 0.20	0.86 \pm 0.18
Gluteus minimus	abd/inrot /exrot	0.26 \pm 0.04	0.22 \pm 0.07	0.27 \pm 0.04	0.21 \pm 0.05
Gluteus maximus	ext/exrot	0.52 \pm 0.24	0.36 \pm 0.14	0.02 \pm 0.02	0.01 \pm 0.01
Semimembranosus	ext/add	0.19 \pm 0.11	0.14 \pm 0.12	0.005 \pm 0.01	<0.001
Semitendinosus	ext/add	0.03 \pm 0.02	0.02 \pm 0.02	<0.001	<0.001
Biceps Femoris (long head)	ext/add	0.13 \pm 0.09	0.11 \pm 0.10	<0.001	<0.001
Biceps Femoris (short head)	knee flex/ext	0.001 \pm 0.001	0.001 \pm 0.001	0.17 \pm 0.05	0.12 \pm 0.05
Sartorius	flex/abd	0.005 \pm 0.01	0.004 \pm 0.006	0.04 \pm 0.01	0.03 \pm 0.01
Iliacus	flex/inrot	0.01 \pm 0.03	<0.001	0.72 \pm 0.28	0.59 \pm 0.25
Psoas	flex/inrot	0.03 \pm 0.08	<0.001	0.78 \pm 0.30	0.64 \pm 0.26
Rectus Femoris	flex/knee ext	0.12 \pm 0.20	0.09 \pm 0.12	0.50 \pm 0.16	0.74 \pm 0.32
Pectineus	flex/add	<0.001	<0.001	<0.001	<0.001
Piriformis	exrot/abd	0.002 \pm 0.004	0.002 \pm 0.002	<0.001	0.001 \pm 0.001
Obturator externus	exrot	0.001 \pm 0.001	0.001 \pm 0.002	<0.001	<0.001
Gracilis	add/flex	<0.001	<0.001	<0.001	<0.001
Adductor longus	add/flex	<0.001	<0.001	<0.001	<0.001
Adductor brevis	add/flex	<0.001	<0.001	<0.001	<0.001
Adductor magnus	add/ext	0.007 \pm 0.01	0.01 \pm 0.01	<0.001	<0.001
Quadratus femoris	exrot	0.002 \pm 0.006	0.002 \pm 0.004	<0.001	<0.001
Gemellus	exrot	0.12 \pm 0.06	0.07 \pm 0.04	0.02 \pm 0.02	0.02 \pm 0.02

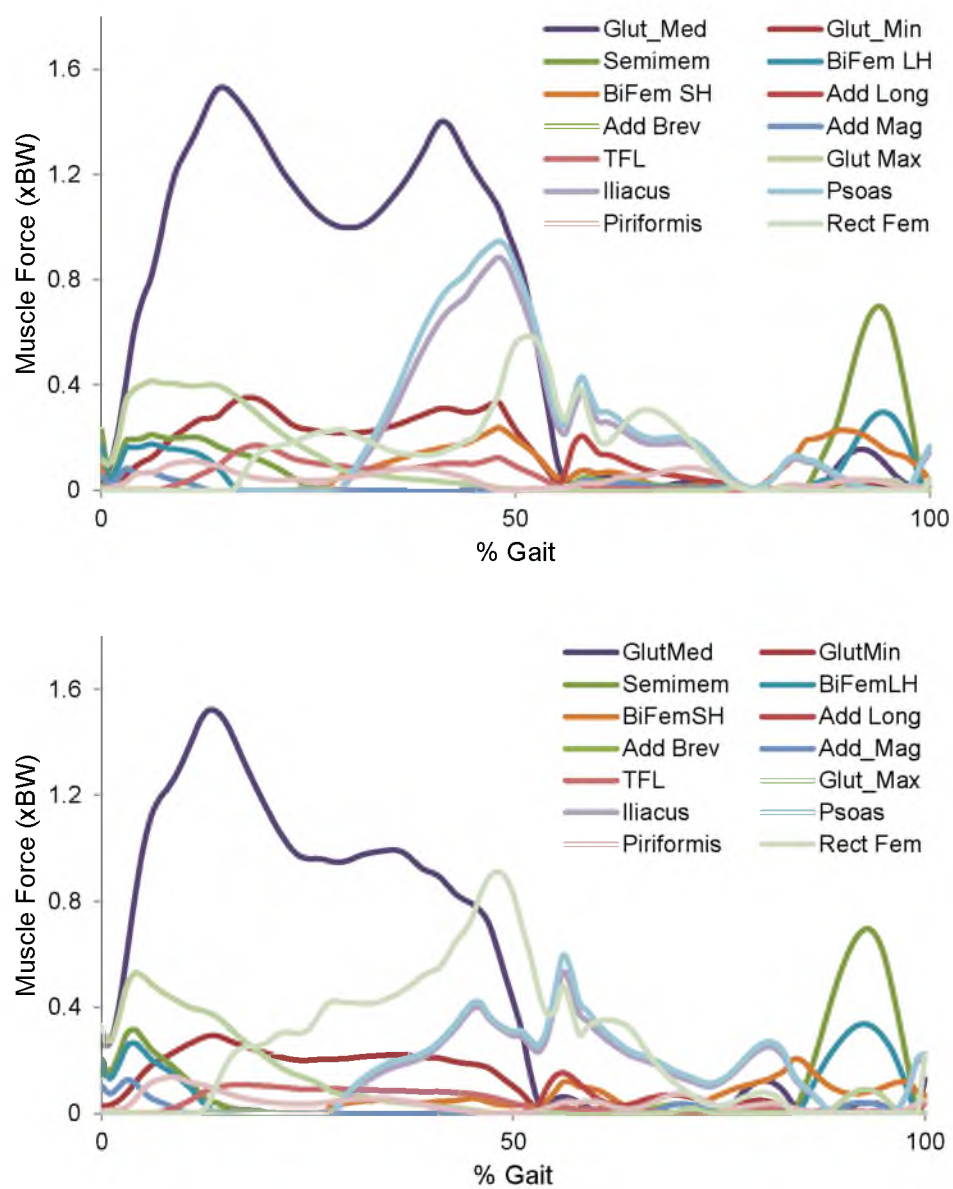


Figure 7.8. Muscle forces from a representative control subject (top) and a dysplastic patient (bottom).

CHAPTER 8

CONCLUSION

8.1 Summary and Impact

The objectives of this dissertation were (1) to quantify anatomical deformities in hips with FAI and (2) improve our understanding of intra-articular and whole joint mechanics in healthy and dysplastic hips.

8.1.1 Objective 1

Assumptions persist that a healthy femoral head is spherical. However, data presented in Chapter 3 demonstrated that femurs without any apparent geometric abnormalities protrude above a best-fit sphere by approximately 2.5 mm. Femurs in patients with cam FAI have protrusions roughly twice that size. While this latter result is to be expected, until now a quantified description of 3D deviations from ideal shapes in cam-type femurs relative to their normal counterparts has not been presented.

The sphere (for 3D surfaces) and circle (for 2D radiographs) will likely continue to serve as a simple comparator when diagnosing cam FAI. However, it is important to account for those deviations that can be expected in healthy populations when diagnosing cam type FAI. This is especially important when using spherical or circular templates to make surgical decisions.

Chapter 3 also provided information about the characteristic features of bony protrusions in control and cam FAI femurs. Control subjects were found to have larger (in area) but flatter (as determined by maximum deviation) protrusions. In contrast, FAI patients had smaller, but more prominent, bumps. It may contribute to damage within the joint. As 3D reconstructions become more available to clinics, the tools and results from Chapter 3 can be used to supplement conventional diagnostic tools and provide complete information about the size, shape, and location of cam deformities.

Choosing the correct radiographic projection and screening protocol is important for properly identifying bony deformities associated with cam FAI in a timely manner, and without undue cost to patients. In Chapter 4, a systematic and objective method was employed to determine which common radiographic projection or radial CT view of the hip may be best suited for detecting cam lesions. Alpha angles measured from the 45° Dunn view with external rotation were found to be strongly correlated to maximum deviation from a sphere. It was interesting to note that the anteroposterior view had the weakest correlation; this view is the most common to initially screen the hip for deformities such as cam FAI.

During the completion of Chapter 4, and as suggested in the study conclusions, two other important considerations came to light that may be important for improving the diagnosis of cam FAI. First, there should be clear communication between surgeons and radiologists or radiology technicians, with respect to patient positioning during x-ray. For example, literature descriptions of the 45° Dunn view stipulate a specific orientation of the femur. However, we found that with the femur held strictly in the prescribed position, correlations to 3D asphericity were relatively weak. Also, images in many

studies, claiming to use the 45° Dunn view, did not match images held strictly to the prescribed 45° Dunn definition.^{1,2} Instead, the images were more similar to ours when we applied external rotation to the femur. Furthermore, from conversations with physicians and technicians from two institutions, we found differences in how individuals were trained to position patients for the different radiographic views. We also found that protocols were often modified ad hoc to accommodate patients or facilitate faster acquisition of radiographs. General adjustments of screening protocols are not discouraged, but we recommend that practitioners standardize radiographic exams to avoid positioning errors. Finally, for clinics equipped to use radial CT or MRI, there may be the temptation to limit analysis to only one or two slices in anterior or anterosuperior region of the head.^{3,4} While Chapter 3 confirms that this region does contain the majority of bony abnormalities, Chapter 4 demonstrated that not all radial slices in this region strongly correlate to maximum asphericity and, therefore, run the risk of misidentifying a cam lesion. Ultimately, the goal of screening is to improve diagnoses and patient care; Chapters 3 and 4 furthered that goal for cam FAI patients.

Chapters 3 and 4 furthered our understanding of hip pathomorphology in cam FAI patients. However, the spectrum of pathomorphologies related to cam FAI is still not fully understood. Chapter 5 demonstrated that statistical shape modeling (SSM) can describe variations in femoral morphology in both controls and cam FAI patients and may be useful for developing new measurements of pathological anatomy. SSM allows the entire proximal femur to be analyzed, and objectively identifies anatomical differences between control subjects and patients, as well as differences among femurs within a group. Some differences, such as variation in the height of the greater trochanter

have not received attention from current clinical screening analyses, but may prove to be an important concomitant factor in FAI patients. As discussed later, application of SSM to the entire hip joint may elucidate additional important morphological features that are characteristic of pathologies but are undetectable with radiographs. Also, the SSM protocol developed for Chapter 5, is easily adaptable to morphological analyses of other joints. For instance, methods from Chapter 5 are currently being employed to characterize shape variation in the shaft of the humerus to improve endoprosthesis design, and to the shoulder to study scapular and humeral head shape with respect to scapular notching and implant design.

8.1.2 Objective 2

To meet the second goal of this dissertation, finite element (FE) models were used to study articular cartilage contact stresses. The FE models followed validation protocols, which remain the most solidly established techniques for accurate contact stress predictions. Quantification of cartilage contact mechanics in ten normally shaped hips from live subjects was a necessary step to further our knowledge of abnormal mechanics in FAI and dysplasia patients. Small variations in the surface anatomy of bone and cartilage within healthy hips were shown to produce, non-uniform and individualized stress distributions. Thus, the need for subject-specific geometry when constructing contact models of the hip was reemphasized.⁵ Also, despite subject-specific distributions of cartilage stresses, data still demonstrated trends in contact area and stress magnitude that are characteristic of healthy hips. For example, peak contact stresses were within a narrow range of approximately 7 to 9 MPa during the simulated activities,

and contact areas were consistently near 34%. Likewise, shifts in contact stress pattern were common between activities. Therefore, the results of Chapter 6 serve as a valuable resource for ongoing and future studies devoted to predicting cartilage contact mechanics in dysplastic hips and FAI patients. Also, CT images collected for Chapter 6 have been made available to the public via download at no charge. It can be difficult for institutions to acquire IRB approval to image healthy individuals using CT. Therefore, it is hoped that these images will be downloaded frequently to serve other investigators who may be interested in quantifying hip anatomy and cartilage contact mechanics.

Finally, Chapter 7 offered preliminary data with regards to kinematic and kinetic differences in whole joint mechanics between healthy and pathologic hips. Few studies have utilized musculoskeletal modeling to quantify hip muscle and joint reaction forces. Validation of musculoskeletal models is difficult.⁶ Nevertheless, the models in Chapter 7 showed good agreement with EMG activation signals for most muscles; joint angles and moments were also within ranges expected for healthy subjects. As discussed later, models of hip joint muscle mechanics require additional refinement. Still the preliminary results of Chapter 7 demonstrate the feasibility of using musculoskeletal modeling to study dysplasia and FAI, and suggest differences may exist in muscle recruitment and force generation between pathologic and healthy hips.

8.2 Limitations and Future Work

Limitations of each study are described within their respective chapters, but some limitations of this dissertation are uniform to the work and motivate future work.

First, CT images were used for most studies in this dissertation. Consequently, subjects were exposed to ionizing radiation. The one time radiation dose for the hip CT was 0.969 rem, which is ~20% of the allowable exposure for employees who utilize radiation as part of their employment (FDA Title 21 CFR Part 361). This exposure is the same as that imparted during standard of care CT exams. However, during the course of diagnosis and treatment, patients likely received additional exposure from radiographs. MR imaging may be an attractive alternative, as it does not require radiation exposure. MRI is becoming increasingly common for the screening of dysplasia and FAI, but most protocols utilize 2D MRI sequences that are insufficient for generating the type of reconstructions used in this dissertation.⁷ Our group is currently investigating 3D MRI sequences with Brigham Young University.⁸ It is hoped that the MRI protocol will result in similar image resolutions and differentiation of bone/cartilage as that obtained with CT arthrography.

As stated in the individual chapters, the techniques and procedures developed to quantify 3D anatomy were applied only to the femur. The femur is a major focus in cases of cam FAI. However, FAI and dysplasia are complicated diseases involving multiple structures, including the pelvis. Chapter 5 served as preliminary data to obtain federal funding which will be used, in part, to apply SSM techniques to study both the acetabulum and the femur in large cohorts of FAI and dysplasia patients. The proposed work may offer valuable information with respect to positioning of geometric abnormalities on the acetabulum versus the femur. SSM may also be used to study cam-like femurs in patients with acetabular dysplasia, which represent a subset of cases that are poorly understood and for which no clear treatment strategy is known.⁹ As

mentioned, the SSM methods developed in this dissertation are being applied to the shoulder and humerus. These examples represent a small sample of orthopaedic pathologies related to shape deformity for which SSM may be beneficially applied.

A third limitation of this dissertation can be found in the use of literature-based joint angles and loading conditions in the FE study of cartilage contact stresses.¹⁰ In the future, loading conditions could be refined by applying the joint angles and joint reaction forces predicted with musculoskeletal models, as discussed in Chapter 7. However, a more precise method for capturing intra-articular joint motion may be necessary. Our group is currently developing methods to use high-speed dual fluoroscopy. Dual fluoroscopy systems are increasingly popular and allow in vivo recording of 3D joint motion without interference from skin and other soft tissue.^{11,12} Joint angles from fluoroscopy, captured for the hip joint, may be coupled with marker based motions and ground reaction forces for the remaining lower limb. These data could then be used to drive the musculoskeletal models and provide refined JRF estimations. In fact, our group will investigate the use of dual-fluoroscopy and marker-based motion tracking to drive musculoskeletal models as an NIH R21 grant. The work highlighted in this dissertation served as important preliminary data to garner NIH funding.

Even with accurate joint kinematics, current musculoskeletal models are limited in their representation of joint geometry. For example, in OpenSim the hip is idealized as a perfect ball and socket. Such simplifying assumptions have an unknown effect on the accuracy of estimations of muscle forces and joint reaction forces, especially in pathologic hips. To address this problem there is increasing attention to the manner in which joints are represented at different scales, or levels, of the continuum.¹³ In addition

to incorporating accurate joint kinematics from dual-fluoroscopy, the NIH R21 discussed above will systematically quantify the sensitivity of musculoskeletal models to changes in joint geometry (i.e., generic versus subject-specific) and muscle attachments and paths (as derived from MR images).^{14,15} Results from the musculoskeletal models will then be used to drive FE models and determine their inherent sensitivity to parameter input. Another feasible approach to addressing the problem of inconsistent representations of the hip joint is, to integrate muscle representations into the FE model, and run all simulations from a single framework – a current pursuit of this and other institutions.^{16,17}

Integrating different modeling technologies may provide more subject-specific descriptions of joint mechanics. However, to be clinically useful, results need to be delivered quickly and in a form that is easy to interpret. Indeed, this is a continuing challenge with FE models, which can take 100+ man-hours per subject from development to final analysis. Integrated musculoskeletal and FE packages are also likely to be time consuming. The methods described in this dissertation make considerable contributions to making morphological analyses systematic, straight forward, and provide information that can be easily used clinically for diagnostics and surgical planning. However, even morphology studies require time to reconstruct joint geometry, compare to ideal shapes, or run statistical shape models. To this end, one aim of the federally funded SSM project is to develop a shape modeling protocol that can quickly and easily incorporate femur or acetabular reconstructions from individual patients and rapidly return a modified shape analysis that describes how the individual's geometry varies compared to a large database of control and pathologic femurs. A framework is also being developed to seamlessly integrate results from SSM with finite element meshing and analysis software. Coupling

these tools will enable fast, robust, and flexible means to analyze the shape and mechanics of target hip pathologies.

8.3 References

1. Clohisy JC, Carlisle JC, Beaule PE, et al. 2008. A systematic approach to the plain radiographic evaluation of the young adult hip. *J Bone Joint Surg Am* 90 Suppl 4:47-66.
2. Domayer SE, Ziebarth K, Chan J, et al. 2011. Femoroacetabular cam-type impingement: Diagnostic sensitivity and specificity of radiographic views compared to radial mri. *Eur J Radiol* 80:805-810.
3. Rakhra KS, Sheikh AM, Allen D, Beaule PE. 2009. Comparison of mri alpha angle measurement planes in femoroacetabular impingement. *Clin Orthop Relat Res* 467:660-665.
4. Pfirrmann CW, Mengiardi B, Dora C, et al. 2006. Cam and pincer femoroacetabular impingement: Characteristic mr arthrographic findings in 50 patients. *Radiology* 240:778-785.
5. Anderson AE, Ellis BJ, Maas SA, Weiss JA. 2010. Effects of idealized joint geometry on finite element predictions of cartilage contact stresses in the hip. *J Biomech* 43:1351-1357.
6. Pandy MG, Andriacchi TP. 2010. Muscle and joint function in human locomotion. *Annu Rev Biomed Eng* 12:401-433.
7. Shapiro L, Harish M, Hargreaves B, et al. 2012. Advances in musculoskeletal mri: Technical considerations. *J Magn Reson Imaging* 36:775-787.
8. Staroswiecki E, Granlund KL, Alley MT, et al. 2012. Simultaneous estimation of $t(2)$ and apparent diffusion coefficient in human articular cartilage in vivo with a modified three-dimensional double echo steady state (dess) sequence at 3 t. *Magn Reson Med* 67:1086-1096.
9. Sugano N, Noble PC, Kamaric E, et al. 1998. The morphology of the femur in developmental dysplasia of the hip. *J Bone Joint Surg Br* 80:711-719.
10. Bergmann G, Deuretzbacher G, Heller M, et al. 2001. Hip contact forces and gait patterns from routine activities. *J Biomech* 34:859-871.

11. Bey MJ, Kline SK, Tashman S, Zauel R. 2008. Accuracy of biplane x-ray imaging combined with model-based tracking for measuring in-vivo patellofemoral joint motion. *J Orthop Surg Res* 3:38.
12. Massimini DF, Boyer PJ, Papannagari R, et al. 2012. In-vivo glenohumeral translation and ligament elongation during abduction and abduction with internal and external rotation. *J Orthop Surg Res* 7:29.
13. Halloran JP, Sibole S, van Donkelaar CC, et al. 2012. Multiscale mechanics of articular cartilage: Potentials and challenges of coupling musculoskeletal, joint, and microscale computational models. *Ann Biomed Eng* 40:2456-2474.
14. Correa TA, Baker R, Graham HK, Pandy MG. 2011. Accuracy of generic musculoskeletal models in predicting the functional roles of muscles in human gait. *J Biomech* 44:2096-2105.
15. Scheys L, Spaepen A, Suetens P, Jonkers I. 2008. Calculated moment-arm and muscle-tendon lengths during gait differ substantially using mr based versus rescaled generic lower-limb musculoskeletal models. *Gait Posture* 28:640-648.
16. Fitzpatrick CK, Shelburne KB, Dunbar B, Rullkoetter P. 2013. Computationally efficient forward-dynamic musculoskeletal modeling in a finite element framework. In, 2013 Orthopaedic Research Society Annual Meeting. San Antonio, TX: Orthopaedic Research Society.
17. Blemker SS, Delp SL. 2005. Three-dimensional representation of complex muscle architectures and geometries. *Ann Biomed Eng* 33:661-673.